Energy Storage Materials 69 (2024) 103440

Contents lists available at ScienceDirect

Energy Storage Materials

journal homepage: www.elsevier.com/locate/ensm

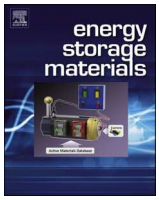

Ni-rich cathode evolution: exploring electrochemical dynamics and strategic modifications to combat degradation

Adil Saleem [a], Leon L. Shaw [a,*], Rashid Iqbal [b], Arshad Hussain [c], Abdul Rehman Akbar [d], Bushra Jabar [e], Sajid Rauf [f], Muhammad Kashif Majeed [g,h,*]

[a] Department of Mechanical, Materials and Aerospace Engineering, Illinois Institute of Technology, Chicago, IL, United States
[b] Key Laboratory of Colloid and Interface Chemistry of the Ministry of Education, School of Chemistry and Chemical Engineering, Shandong University, 250100 Jinan, China
[c] Interdisciplinary Research Center for Hydrogen and Energy Storage, King Fahd University of Petroleum & Minerals, Dhahran 31261, Saudi Arabia
[d] Institute for Advanced Study, Shenzhen University, Shenzhen 518060, China
[e] Institute for Metallic Materials, Leibniz Institute for Solid State and Materials Research Dresden (IFW Dresden), Dresden 01069, Germany
[f] College of Mechatronics and Control Engineering, Shenzhen University, Shenzhen 518060, China
[g] Department of Mechanical Engineering, The University of Texas at Dallas, Richardson, TX, United States
[h] Department of Chemistry, School of Natural Sciences, National University of Science and Technology, Islamabad, 44000, Pakistan

ARTICLE INFO

Keywords:
Lithium-ion batteries
Ni-rich cathode
Electrochemical dynamics
Interfacial stability
Cathode degradation

ABSTRACT

Nickel (Ni)-rich cathode materials hold immense promise for high-energy-density lithium-ion batteries (LIBs), yet their widespread deployment is hampered by significant challenges related to structural and interfacial degradation. These include rapid capacity fading, which diminishes their long-term performance, and the risk of thermal runaway caused by crystal disintegration, leading to safety concerns. Additionally, interfacial instability poses a hurdle to the widespread adoption of these cathodes in commercial applications. Addressing these issues is crucial for the successful commercialization of layered Ni-rich cathodes in energy storage systems. This paper provides a comprehensive analysis of the electrochemical dynamics underlying the degradation mechanisms in Ni-rich cathodes and explores innovative modification strategies to mitigate these issues. Through an in-depth investigation, we uncover the intricate processes leading to voltage fade, capacity decay, and structural instability. Utilizing advanced characterization techniques, including in situ and operando methodologies, we gain real-time insights into the degradation mechanisms. Furthermore, this study delves into cutting-edge modification strategies, such as surface coatings, doping techniques, and nano-structuring approaches, aimed at enhancing the stability of Ni-rich cathode materials. By synthesizing knowledge from electrochemical dynamics and innovative modification strategies, this research contributes valuable insights for the development of high-performance and long-lasting LIBs, essential for the future of energy storage and electric transportation technologies.

1. Introduction

1.1. Background and significance

The excessive consumption of fossil fuels results in the uncontrolled release of carbon dioxide and significant amounts of greenhouse gases into the atmosphere, leading to the dispersion of impurities and environmental damage. Considering this, the imperative for sustainable energy growth becomes evident, as even renewable energy cannot fully achieve its desired impact without a more efficient method of electricity storage. Hence, there is a critical need for high-performance energy storage devices exhibiting both high energy and power density to ensure the sustainability and safety of storing renewable energy. Electrochemical cells have long been recognized as promising candidates for reliable energy storage. In this context, LIBs have emerged as dominant players, showcasing outstanding characteristics such as high energy density, extended life cycles, cost-effective maintenance, absence of memory effect, sustainability, and relative eco-friendliness (Fig. 1) [1–3]. Recently, they have opened up new applications widely in portable electronic devices, electric vehicles, energy storage grids and

* Corresponding authors.
E-mail addresses: lshaw2@iit.edu (L.L. Shaw), drmkm@utdallad.edu (M.K. Majeed).

https://doi.org/10.1016/j.ensm.2024.103440
Received 5 March 2024; Received in revised form 8 April 2024; Accepted 29 April 2024
Available online 30 April 2024

other fields. Despite all this, automotive applications will have a huge impact on the rapid development of LIBs due to the huge element resource consumption as compared to portable devices [4]. However, the widespread adoption of electric vehicles still faces obstacles, such as range anxiety, price, capital preservation rate, capacity retention and safety [5–7].

In contrast to traditional Ni-metal hydride, Ni-cadmium, and lead-acid batteries, LIBs gained widespread attention following their commercialization by Sony in 1991 [9–11]. This was attributed to their impressive performance, high energy density, and extended cycle life. Over the past two decades, the demand for LIBs has consistently risen, prompting extensive research into high-performance electrode materials [12]. Typically, a LIB comprises three main components: the cathode, anode and electrolyte (Fig. 1). The initial prototype LIB utilized the $LiCoO_2$/Li system, with $LiCoO_2$ as the cathode material and Li metal as the anode material. The charge/discharge cycle involved Li insertion and extraction from the layered structure of $LiCoO_2$. However, for safety considerations, metallic Li was substituted with carbon-containing materials in the secondary LIB. Beyond carbonaceous materials, various other substances, including Si, Sn, $Li_4Ti_5O_{12}$, and other metal oxides, have been reported as potential anode materials (Fig. 1). However, with a diverse range of anode materials available, there is a notable scarcity in the selection of applicable cathode materials. Despite the extensive study of intercalation chemistry spanning hundreds of years, the variety of cathode materials remains limited [13]. The main groups of cathode materials comprise spinel $LiMn_2O_4$, layered $LiCoO_2$, layered $LiNi_xCo_yMn_{1-x-y}O_2$, polyanion $LiFePO_4$ and their byproducts (Fig. 1) [14–17]. Among these cathode material categories, $LiFePO_4$ has dominated the scene for the past three decades. However, there is a recent surge in interest in layered transition metal (TM) oxides for LIBs due to their ability to offer significantly higher energy density compared to $LiFePO_4$ cathode materials.

Generally, numerous approaches have been focused on progressing the electrochemical performance and energy density of layered TM oxides for LIBs [18]. Several strategies have been explored in the pursuit of enhancing Li^+ transmission rates and mitigating challenges in cathode materials. These strategies include element doping, which accelerates Li^+ transmission, and surface modification, which reduces charging resistance during the transfer process and hinders side reactions at the electrolyte interface [19]. Additionally, adjusting the component ratio is recognized as a beneficial approach. Ni-rich materials are anticipated to emerge as the next-generation cathode materials due to their cost-effectiveness and high energy density [20]. Nevertheless, these materials encounter notable issues, such as irreversible capacity decay in the initial cycle, voltage lag in charging/discharging, rate capability challenges, and voltage attenuation [21]. Recent findings highlight the pivotal role of Ni in mitigating voltage decay among these materials. During the charging/discharging process, a protective Ni-rich and Li-poor rock salt crust forms, acting as a barrier to oxygen loss [6]. Increasing the proportion of Ni suppresses phase changes and effectively addresses the voltage attenuation issue by establishing a Ni^{3+} redox buffer that inhibits the Mn^{3+}/Mn^{4+} redox reaction [22]. Therefore, among various layered cathode materials, Ni-rich cathode materials like $LiNi_xMn_yCo_zO_2$ (NMC) and $LiNi_xCo_yAl_zO_2$ (NCA) emerge as practical contenders for widespread LIB applications, considering reversible capacity, rate capability, and capital cost [23]. Notably, Ni-rich cathodes with Ni content exceeding 80 % offer advantages of higher gravimetric energy density compared to that with Ni content below 80 % [24]. Presently, Ni-rich cathodes with less than 60 % concentration have been successfully commercialized. However, challenges persist in the

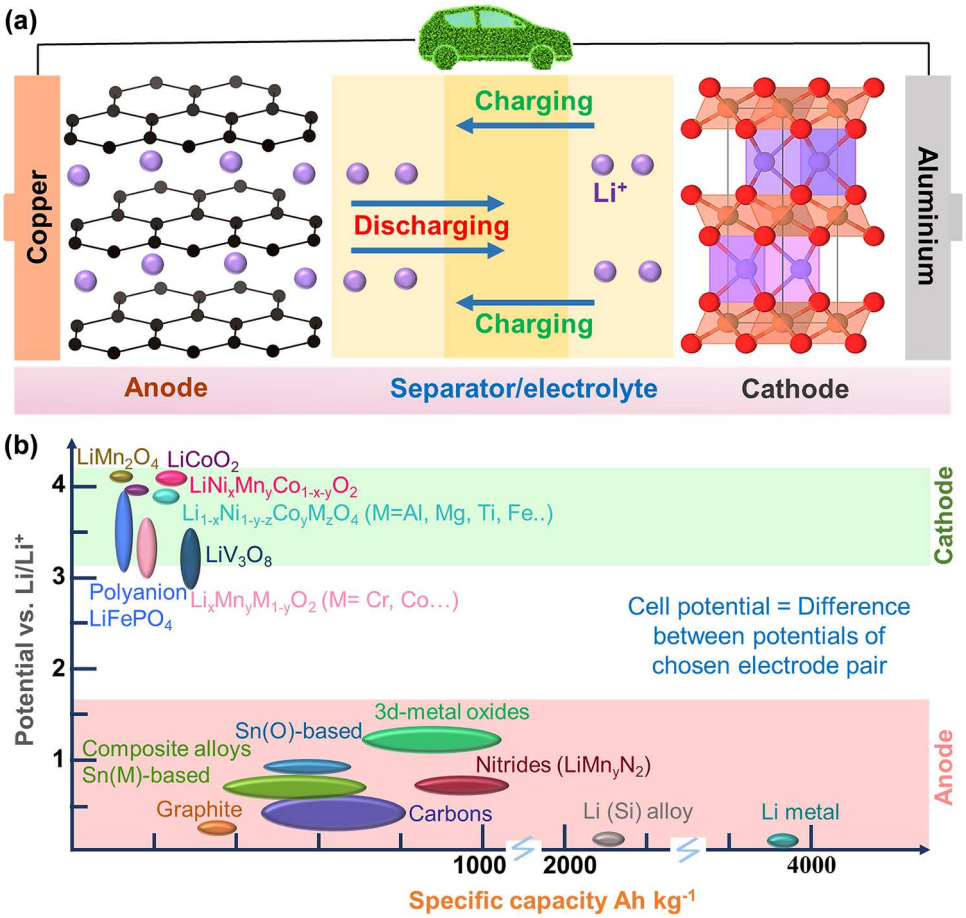

Fig. 1. **(a)** The hierarchical structure of LIBs, and **(b)** voltage vs. specific capacity for cathode and anode materials [8].

commercialization of Ni-rich cathodes with ≥80 % Ni content, particularly concerning powder properties and electrode manufacturing processes [25]. Indeed, the structural degradation of Ni-rich cathode materials is a critical challenge that affects the performance and longevity of LIBs, as shown in several recent review articles [26–28]. This degradation can begin even before battery assembly when the materials are exposed to air. Surface impurity species formed on $LiNi_{0.8}Mn_{0.1}Co_{0.1}O_2$ (NMC811) upon exposure to ambient air not only lead to a significant delithiation voltage peak in the first charge, but also markedly reduce the cycling stability of NMC811-graphite cells due to significant polarization of the NMC811 electrode [29]. Understanding and mitigating these degradation mechanisms are crucial for improving the overall stability and efficiency of Ni-rich LIBs.

This review delves into innovative strategies aimed at overcoming structural and interfacial degradation challenges in Ni-rich cathode materials used in LIBs (Fig. 2). The focus is on dynamic solutions, offering insights into electrochemical dynamics and state-of-the-art modification techniques. The continued exploration of Ni-rich cathode materials is yielding new perspectives and insights that have the potential to drive significant advancements in battery technology, enabling the development of safer, more efficient, and long-lasting energy storage devices. By going beyond traditional approaches, the article aims to shed light on promising avenues for enhancing the durability and performance of Ni-rich cathodes, ultimately contributing to the advancement of safer and long-lasting LIB technology.

1.2. Challenges in the synthesis and stability of Ni-rich cathode materials

Despite the enhanced storage capacity offered by Ni-rich cathodes, there comes a tradeoff in terms of electrochemical stability [35]. Research has confirmed that the crystal structure of Ni-rich cathode materials tends to undergo irreversible transformations during the delithiation process, leading to rapid performance deterioration. The extent of degradation is influenced by the specific elemental composition within the cathode material. Nevertheless, all Ni-rich cathodes experience comparable electronic and structural changes. It is crucial to note that, in addition to considering cathode materials, the degradations occurring in the battery anode and electrolyte should also be taken into account when assessing the overall performance from a full-cell perspective [36].

Graphite stands out as the most commercially viable anode material currently available in the market and is frequently paired with Ni-rich cathodes in modern batteries. In contrast, Li-metal is deemed as an ideal anode material due to its lowest negative electrochemical potential and possesses the highest specific capacity among any cathode material. both anode materials encounter significant challenges, including the formation of solid-electrolyte interphase (SEI) and the dendrite growth [37]. These issues present significant obstacles to the widespread commercialization of Ni-rich-based LIBs as the next generation of batteries. Various techniques have been employed to address these challenges and improve the electrochemical performance of Ni-rich layered oxides. These include elemental doping, surface modification, Li^+ extraction by increasing the cut-off voltage, increasing the fraction of redox elements such as Ni or other transition metals, and preserving structural stability [38–42]. Adjusting the proportions of components is also considered a viable strategy. Due to its high discharge capacity and cost-effectiveness, $LiNiO_2$ layered oxide has emerged as a potential cathode material for further development [43]. Unfortunately, the preparation of $LiNiO_2$ with complete stoichiometry faces difficulties due to unavoidable cation disorder. Consequently, $LiNiO_2$ with Ni>0.6 has

Fig. 2. Schematic illustration of the major challenges and strategies of Ni-rich cathode materials in different stages from crystal structure to practical applications [30–34].

been developed as a Ni-rich layered cathode material, similar to the rhombic phase of $LiNiO_2$ [44]. While Ni-rich materials demonstrate high energy density, their cycle performance decreases with increasing capacity. This is attributed to the weaker Ni-O bond, which compromises the stability of the layered structure and induces anisotropic volume changes during the lithiation/delithiation process. Additionally, Ni-rich materials, despite their potential as next-generation cathode materials due to low cost and high capacity, encounter issues such as irretrievable capacity degradation, voltage degradation, rate capability challenges, and voltage hysteresis during charge/discharge [45]. Notably, Ni plays a crucial role in inhibiting voltage degradation among these materials. During charging and discharging, Ni-rich and Li-poor rock salt crusts are formed, acting as a protective layer to suppress oxygen loss. Increasing the proportion of Ni inhibits phase changes and efficiently resolves the issue of voltage attenuation by forming a Ni^{3+} redox buffer to prevent the redox reaction of Mn^{3+}/Mn^{4+} [46]. The electrochemical performance of the cathode material is intricately linked to the physical properties of the precursor. As the synthetic route significantly influences precursor properties and electronic conductivity, exploring the synthesis method is crucial for producing an optimal product [47]. Various synthesis techniques, such as sol-gel, solid-state reaction, spray drying, and co-precipitation, have been developed [48–51]. A comparative overview of all the synthetic techniques is presented in Table 1. The effectiveness of this complex cathode material is intricately linked to the nature of the precursor particles in terms of the chemical composition and various physical characteristics, such as particle size, shape, crystal structure, crystallinity, structural integrity, and cation arrangement. Presently, the synthesis technique that offers the highest degree of control for mass production in an industrial setting involves a hydroxide coprecipitation process followed by solid-state reaction. While certain NMC compounds have made their way into commercial products, the optimized synthesis conditions for precursors like temperature, duration, pH level, stirring rate and compositions attributes on the material's physical features and ultimate electrochemical performance remains poorly understood, particularly at the scale of industrial manufacturing. A significant amount of research has focused on the development of synthetic methods for various Ni-rich cathode materials for LIBs, resulting in substantial enhancements. The summary improvements in their electrochemical performance with different synthesize techniques are detailed in Table 2.

In Ni-based layered oxides, the migration of Ni^{2+} to vacancies in the Li layer through tetrahedral interstices occurs after Li^+ extraction, accompanied by a loss of lattice oxygen (Fig. 3**a**). These parasitic reactions, occurring during charging, contribute to unfavorable phase transformations and a reduction in thermal stability. The oxidation of Ni^{2+} at the Li layer leads to a significant contraction of the octahedral cell due to the corresponding loss of electrons in the e_g orbit (Fig. 3**b**). The shrinkage of the unit cell is intricately connected to the contraction along the c-axis, leading to anisotropic volume deformation of the primary particles and internal mechanical stress. The crystal fields generated by the coordination of octahedral oxygen anions for Ni, Mn, and Co divide the 5d orbitals of TMs into two energy level groups known as e_g and t_{2g} [71]. In addition, due to the increase in electrostatic repulsion of coordination anion, the energy of e_g is higher than the other [72]. The ionic states of Ni ions, where oxygen redox reactions start the main role of material capacity. The overlapping between the $Ni^{3+/4+}$ position in the e_g band and the top of the O^{2-} 2p band is smaller than the $Co^{3+/4+}$ position in the t_{2g} band, indicating that $Ni^{3+/4+}$ has less electron delocalization [73]. Therefore, the Ni^{4+} state can be achieved in the layered material with a higher lithium utilization rate in the main structure, reaching a capacity of 220 mAh g^{-1} [74]. The interfacial reactions between the Ni-rich cathode and electrolyte stem from the spontaneous reductions of transition metal ions. This reduction process facilitates the catalytic decomposition of the electrolyte solvent, resulting in the formation of the organic SEI layer. This SEI layer consists of carboxylate (O—C═O) and semi-carbonates ($ROCO_2Li$), as depicted in Fig. 3**c** [75]. The decomposition of the electrolyte solvent is accompanied by the generation of gases such as C_xH_y, CO_2, and CO [76]. Notably, the decomposition of the solvent is reported to be enhanced at higher temperatures. Shikano et al. [77] conducted an analysis of the formation of the organic SEI layer in the $LiNi_{0.73}Co_{0.17}Al_{0.10}O_2$ cathode after electrochemical testing at different temperatures. As the temperature increased, the intensity of the organic SEI layer components, such as semi-carbonate and poly-carbonate, significantly increased (Fig. 3**d**) [77]. Particularly, the presence of carbonate-containing organic compounds substantially increased at temperatures exceeding 60 °C, indicating that the catalytic decomposition of the electrolyte solvent was

Table 1
Comparative overview of all the synthetic techniques.

Synthesis method	Advantages	Disadvantages
Co-precipitation	Cost effective, scalable, tunable composition and morphology	Agglomeration, reaction dependent
Solid-state	Simple, scalable	Low homogeneity, impurity risk, high energy consumption
Sol-gel	Small and uniform particle size, tunable morphology and composition, low agglomeration	Long reaction time, high cost
Spray pyrolysis	Continuous, scalable, uniform particle size, high reproducibility	Complicated, high cost, low density particle
Hydrothermal	Simple, low cost, controlled particle size, homogeneity	Long reaction time, non-scalable
Solvothermal	Uniform and controlled particle size, homogeneity, tunable composition	Non-scalable, equipment dependent
Spray drying	Simple, scalable, uniform particle size, homogeneity,	Equipment dependent

Table 2
Summary of various Ni-rich cathode materials with different synthesize techniques and electrochemical performance.

Material	Synthesis method	Capacity retention (%)/cycle	Cut-off voltage (V)	Ref.
$LiNi_{0.8}Co_{0.1}Mn_{0.1}O_2$	Co-precipitation	88/200	4.3	[52]
$LiNi_{0.85}Co_{0.05}Mn_{0.1}O_2$	Co-precipitation	82/100	4.3	[53]
$LiNi_{0.83}Co_{0.1}Mn_{0.07}O_2$	Co-precipitation	84/400	4.35	[54]
$LiNi_{0.85}Co_{0.1}Mn_{0.05}O_2$	Co-precipitation	82/150	4.3	[55]
$LiNi_{0.65}Co_{0.08}Mn_{0.27}O_2$	Co-precipitation	96/50	4.3	[56]
$LiNi_{0.48}Co_{0.26}Mn_{0.26}O_2$	Co-precipitation	93/100	4.5	[57]
$LiNi_{0.56}Co_{0.18}Mn_{0.26}O_2$	Co-precipitation	91/100	4.5	[57]
$LiNi_{0.7}Co_{0.15}Mn_{0.15}O_2$	Co-precipitation	84/50	4.3	[58]
$LiNi_{0.58}Co_{0.25}Mn_{0.17}O_2$	Co-precipitation	78/500	4.3	[59]
$LiNi_{0.72}Co_{0.10}Mn_{0.18}O_2$	Co-precipitation	70/100	4.5	[60]
$LiNi_{0.76}Co_{0.14}Mn_{0.10}O_2$	Co-precipitation	86/100	4.5	[61]
$LiNi_{0.80}Co_{0.15}Al_{0.05}O_2$	Co-precipitation	88/200	4.3	[62]
$LiNi_{0.7}Co_{0.15}Mn_{0.15}O_2$	Solvothermal	86/100	4.3	[63]
$LiNi_{0.9}Mn_{0.1}O_2$	Sol-gel	57/100	4.5	[64]
$LiNi_{0.5}Co_{0.2}Mn_{0.3}O_2$	Hydrothermal	79/50	4.6	[65]
$LiNi_{0.8}Co_{0.1}Mn_{0.1}O_2$	Hydrothermal	94/100	4.3	[66]
$LiNi_{0.8}Co_{0.1}Mn_{0.1}O_2$	Spray drying	81/200	4.3	[67]
$LiNi_{0.8}Co_{0.1}Mn_{0.1}O_2$	Solid-state	71/100	4.3	[68]
$LiNi_{0.6}Co_{0.2}Mn_{0.2}O_2$	Co-precipitation	83/100	4.3	[69]
$LiNi_{0.8}Co_{0.1}Mn_{0.1}O_2$	Spray pyrolysis	85/100	4.4	[70]

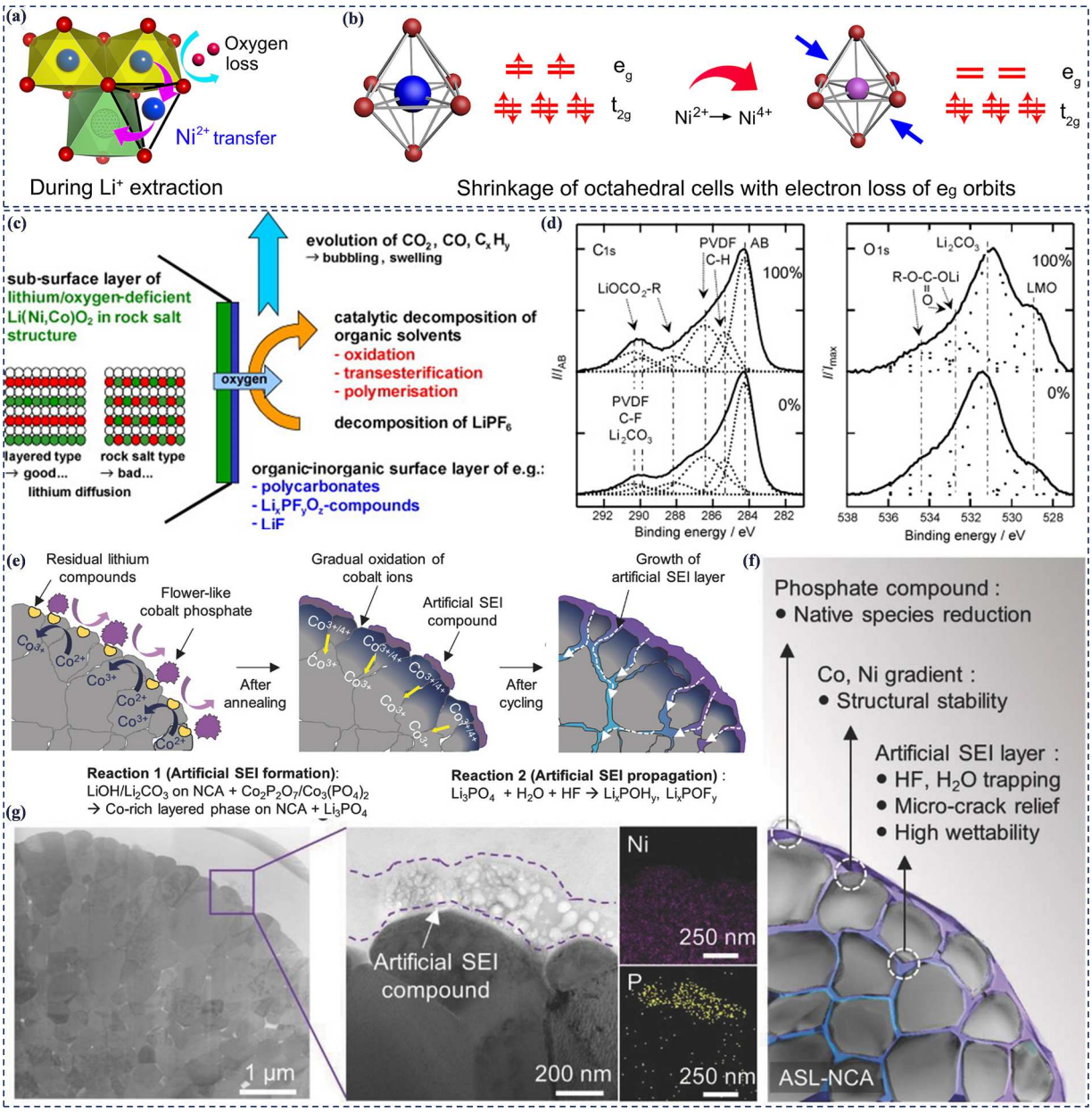

Fig. 3. (a, b) A schematic illustration of the failure mechanism of Ni-rich cathode. Reproduced with permission [34]. Copyright 2021, Nature. **(c)** Surface film formation during charged state in Ni-rich cathode. Reproduced with permission [75]. Copyright 2005, Elsevier. **(d)** C1s and O1s high-resolution hard X-ray photoemission spectroscopy (HX-PES) spectra of the $LiNi_{0.73}Co_{0.17}Al_{0.10}O_2$ cathode before and after the electrochemical test with increasing temperature. Reproduced with permission [77]. Copyright 2007, Elsevier. **(e-g)** Formation of artificial SEI layer and SEI compounds. Reproduced with permission [78]. Copyright 2018, Wiley-VCH.

more pronounced at temperatures ≥60 °C. The study also delves into the robustness and stability of the $LiNi_{0.84}Co_{0.14}Al_{0.02}O_2$ (NCA) cathode material during battery cycling, summarizing the impact of the artificial SEI layer (Fig. 3**e** and 3**f**) [78]. In the formation of the artificial SEI layer, native surface species like Li_2CO_3 and LiOH at the cathode surface undergo reactions with the Co-phosphate composite, specifically $Co_2P_2O_7$ and $Co_3(PO_4)_2$. This SEI compound appears blurred and is exclusively observed on the cathode surface. Notably, the artificial SEI layer, with a thickness of approximately ≈200 nm, is predominantly composed of phosphorus elements (Fig. 3**g**).

2. Electrochemical dynamics of Ni-rich cathode materials

The electrochemical characteristics and structural stability of NMC materials are mostly determined by the Ni concentration. Many investigations have now proven that increasing Ni concentration leads to increased storage capacity and lower electrode stability [79–81]. A rise in the Ni ratio, in particular, leads to an increase in high-valence Ni ions (Ni^{3+}, Ni^{4+}), which contributes to the increased capacity. These ions, on the other hand, react readily with the battery electrolyte, causing cycle instabilities. Presently, commercially successful NMCs with $x \leq 0.6$ and NCA with $x \approx 0.8$ have been established. However, the commercialization of those with even higher x values encounters numerous challenges due to performance degradation and safety hazards throughout the battery's lifespan [82]. Battery performance degrades with reduced capacity and voltage, increased volume, and impedance. This degradation poses safety risks, including thermal runaway during abuse conditions like overcharging and overheating [83]. The prevailing agreement is that the former problem stems from the aggressive chemical, structural, and mechanical deterioration of the

Ni-rich layered oxides. Meanwhile, the latter is ascribed to the thermodynamic instability of the Ni-rich layered oxides near the fully charged state or at elevated temperatures [34]. Although the mechanisms behind battery failure are intricate and may vary case by case, the following discussion highlights the key problems and their origins.

2.1. Surface reactions and gas evolution

In spite of the increased interest in Ni-rich cathode-based LIBs, their practical applicability is still limited due to performance deterioration and safety concerns. Different types of cathode materials ($LiFePO_4$, $LiCoO_2$, $LiMn_2O_4$, $LiNiO_2$, $LiNi_xCo_yMn_{1-x-y}O_2$, $LiNi_xCo_yAl_{1-x-y}O_2$, etc.) have been explored in LIBs, representing a research hotspot over the past few decades due to their high reversible capacity and cost-effectiveness [72,84,85]. A common strategy to achieve high reversible capacity is to increase the Ni-content [86]. Numerous researchers have successfully synthesized Ni-rich cathode materials with Ni-content exceeding 90 %, demonstrating high reversible capacity [87]. However, the elevated Ni-contents also pose risks such as the formation of residual Li-compounds (RLCs), and the associated side effects of these impurities, including low first efficiency and weak storage properties, cannot be overlooked [88–90]. A comprehensive understanding of the RLC formation mechanism on the surface of Ni-rich cathode materials is essential to minimize its negative impacts and enhance the electrochemical performance of LIBs.

This knowledge can provide insights into the origin of RLCs and the conditions necessary for designing high-performance Ni-rich cathode materials. Fig. 4**a** illustrates a schematic depiction of RLCs growth on a Ni-rich cathode surface [78]. The actual composition and quantity of surface impurities can vary based on synthesis parameters and storage conditions.

The primary components of RLCs on the surface of Ni-rich cathode materials include Li_2CO_3, $LiHCO_3$, Li_2O, Li_2O_2, and LiOH. During the storage process, the majority of these compounds decompose into LiOH and Li_2CO_3 (Fig. 4**b**) [91,92]. To compensate for Li loss during calcination due to volatilization at high temperatures, an additional quantity of Li salts is introduced as a transition metal precursor throughout the synthesis process. Moreover, a higher Li salt concentration helps prevent Li/TM ion mixing. However, the excess Li content remains at the particle surface and reacts with H_2O, O_2, and CO_2 in the air, forming a surface RLC composed of Li_2CO_3, $LiHCO_3$, and LiOH. Consequently, the formation of RLCs on Ni-rich cathode materials appears to be inevitable, and airborne H_2O and CO_2 are two variables that encourage their formation [93]. In a study by Sora et al. [93] the impact of residual Li compounds in LIBs with liquid electrolytes was investigated using non-washed pristine-NMC and washed-NCM (Fig. 4**c**). FE-SEM images of NMC particles reveal that the surface of the pristine-NMC is covered with film-like residual Li compounds, while the surface of the washed-NMC is clear and bare, aligning with previous literature (Fig. 4**d** and 4**e**). The X-ray photoelectron spectroscopy (XPS) analysis shows the O1s spectra identifying the removed species on the surface for both pristine and washed NMC cathodes (Fig. 4**f**). Although the voltage profiles of pristine and washed NMC cathodes were nearly identical, the initial charged capacities were different (Fig. 4**g**).

According to Sung et al. [92] H_2O is required to create surface RLCs at room temperature. Keeping $LiNi_{0.8}Co_{0.1}Mn_{0.1}O_2$ (NMC811) material powder in a reactor with airflow for 24 h to examine the involvement of H_2O and CO_2 in the formation of RLCs. They found that the RLCs increased considerably in the wet CO_2 gas, however, in the other two gases, dry CO_2 (99.99 %) and wet Ar gas, the RLCs increased much less. This indicates that at ambient temperature, both H_2O and CO_2 are required for the formation of RLCs. Furthermore, the heterogeneity of the electrochemical reaction, attributed to the insulating Li_2CO_3 coating on the surface, has been reported. This phenomenon is illustrated in Fig. 4**h** [99]. where the splitting of the (003) reflection is revealed through in-situ XRD analysis. Expanding on this observation, Qian et al. [95] suggested that the uneven accumulation of residual Li compounds leads to reaction heterogeneity, causing variations in energy barriers and activation energies for the delithiation of individual particles (Fig. 4**i**). Moreover, adverse interactions between the $LiPF_6$-based electrolyte and residual Li compounds at the electrode-electrolyte interface may result in the generation of LiF and CO_2 gas (Fig. 4**j**). Bi et al. [96] examined the electrochemical performance of Li_2CO_3-coated and LiF-coated NMC811 in order to support the effect of surface LiF and Li_2CO_3 on the performance of Ni-rich cathode materials. Fig. 4**k** illustrates how cycle stability was negatively impacted by the surface Li_2CO_3 coating layer, but not at all by the LiF coating. This discrepancy was explained by the electrolyte's reaction with Li_2CO_3's breakdown. Renfrew et al. [97] made the unexpected discovery that CO_2/CO emission resulted from the first charge's breakdown of leftover Li_2CO_3. Furthermore, after removing a portion of the surface Li_2CO_3, the oxygen evolution from the lattice of Ni-rich cathode materials reduced, indicating a connection between the oxidation of Li_2CO_3 and the lattice oxygen release (Fig. 4**l**) [97]. Hatsukade et al. [98] used isotope labeling to look into the source of CO_2 during $LiNi_{0.6}Co_{0.2}Mn_{0.2}O_2$ (NMC622) cycling. The surface Li_2CO_3 breakdown at high potential was identified as the cause of the CO_2 production during the initial charge step. Nevertheless, CO_2 resulting from chemical and electrochemical oxidation at high potential of the electrolyte solvent became predominant with extended cycling and the reduction of surface Li_2CO_3 (Fig. 4**m**) [98].

The most dangerous safety concern with LIBs is the gas leaking problem. The events that cause the gas release are often exothermic, causing a succession of chain reactions that finally result in the battery self-combusting catastrophically [100]. The most common gaseous breakdown products are CO_2 and O_2. The gas production in Ni-rich cathodes is mainly due to the electrolyte/surface mixed reactivity, Li_2CO_3 breakdown and direct electrolyte oxidation as illustrated in Fig. 5**a** [101]. A high state of charge will increase gas formation due to the existence of surface imperfections. Electrolyte decomposition processes are also stimulated by a high delithiation condition. Washing has long been used to relieve adverse effects such as gaseous emissions resulting from surface pollution. Varied solvents and processes utilized in the washing process result in variable surface contaminant compounds, leading to different gas evolution behavior, according to studies. Renfrew and McCloskey [101] investigated the effect of surface contamination on gas evolution in delithiated NMC622 using a variety of washing methods (Fig. 5**b**). They generated NMC622 samples with various treatments and monitored the gas evolution for a long period at 4.8 V. The sample with the H_2O soaking procedure had the least amount of gas evolution and capacity loss. Their findings revealed complicated gas production mechanisms that are influenced by surface pollutants and flaws. In order to reduce total gas creation, adequate surface preparation is required.

The development of O_2 and CO_2 gas in the battery system is considerably accelerated under high voltage operation. The gas generation at the NMC622 electrode was examined using differential electrochemical mass spectrometry under potentiostatic control at 4.8 V, as illustrated in Fig. 5**c** [101]. Surprisingly, the development of CO_2 and O_2 exhibits divergent patterns. The rate of O_2 evolution peaked at 4.8 V at the conclusion of galvanostatic charging and then reduced as the current dropped during the potentiostatic period. The CO_2 evolution rate continues to climb towards the start of the potentiostatic phase, only after 1 hour does it begin to fall. This pattern implies that the quantity of O_2 evolution is regulated by the delithiation depth and is directly connected to lattice defection at the outermost surface. The breakdown of Li_2CO_3 at the cathode surface is responsible for the majority of CO_2 evolution. Growing a surface carbonate layer and examining these materials as a function of various cut-off voltages further corroborated this finding. At 3.9 V, the surface carbonate layer was discovered, and the beginning voltage of O_2 lattice loss was identified at roughly 4.45 V. After discharge, the majority of the electrolyte breakdown products will come from the surface. On the other hand, the creation of the surface disorder

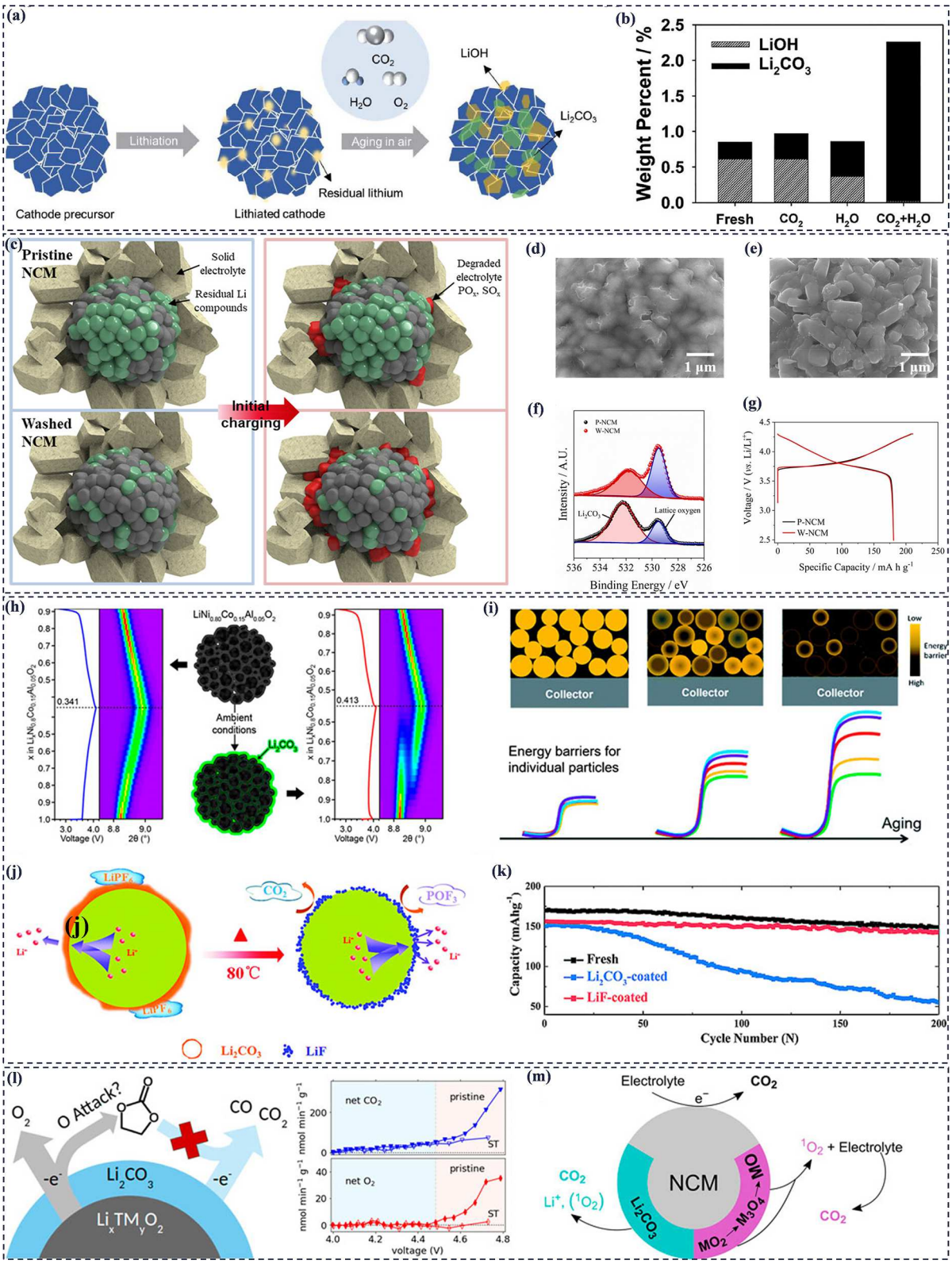

Fig. 4. **(a)** RLCs growth on Ni-rich cathode surface. Reproduced with permission [91]. Copyright 2018, Wiley-VCH. **(b)** The amount of residual compounds. Reproduced with permission [92]. Copyright 2019, ACS. **(c)** Effect of RLCs in suppressing side reactions with solid-state electrolyte, and FE-SEM images of **(d)** pristine NMC and **(e)** washed NMC, **(f)** top-most O 1 s XPS spectra, and **(g)** initial voltage profiles of the pristine NMC and washed NMC with liquid electrolyte at 0.1C. Reproduced with permission [93]. Copyright 2023, ACS. **(h)** The splitting of the (003) reflection of NCA after air exposure. Reproduced with permission [94]. Copyright 2017, ACS. **(i)** Schematic diagram of the energy barrier evolution with aging. Reproduced with permission [95]. Copyright 2019, RSC. **(j)** Schematic illustration of the surface reaction of Li_2CO_3-coated material in $LiPF_6$ electrolyte and **(k)** Cyclic stability of fresh, Li_2O coated, LiF coated NCM811 at 1 C. Reproduced with permission [96]. Copyright 2016, RSC. **(l)** Gas evolution for pristine and surface treated NMC, showing attenuation of both the CO_2 and O_2 evolution rates after removal of a portion of Li_2CO_3. Reproduced with permission [97]. Copyright 2017, ACS. **(m)** CO_2 emission during cycling of Ni-rich cathodes, including the decomposition of Li_2CO_3, chemical and electrochemical oxidation of electrolyte. Reproduced with permission [98]. Copyright 2018, ACS.

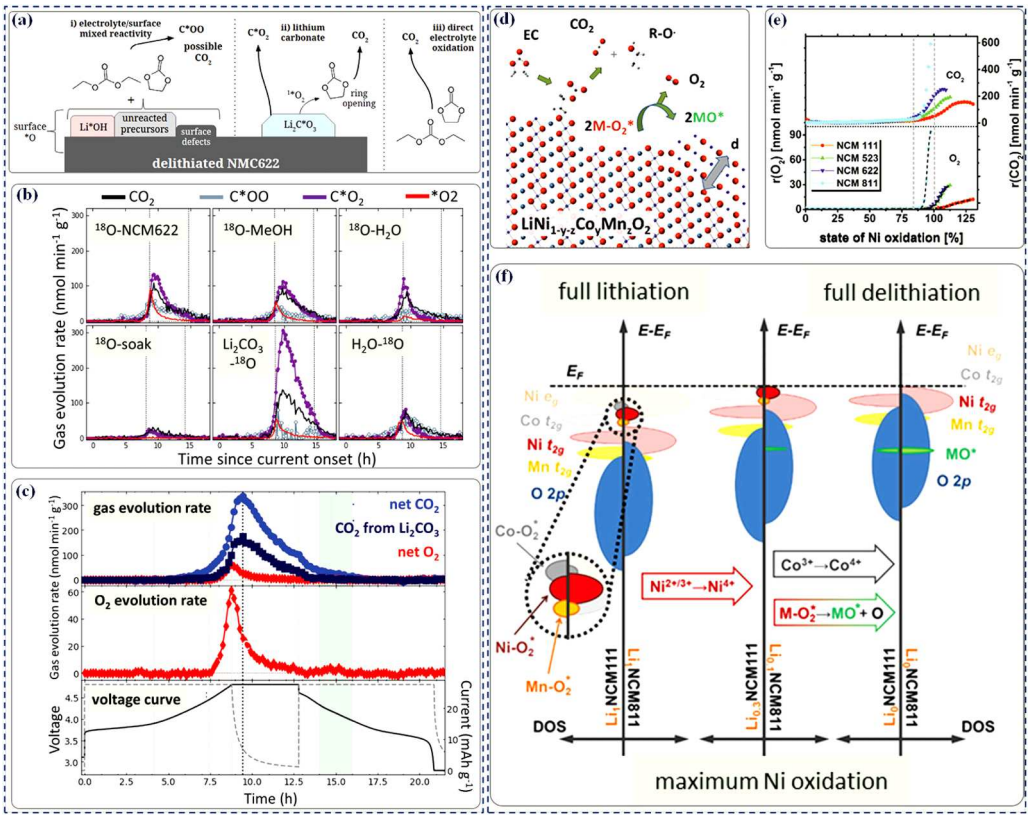

Fig. 5. **(a)** Gas formation at the surface, **(b)** CO_2 and O_2 breakdown for NMC622s under. Reproduced with permission [102]. Copyright 2019, ACS. **(c)** Gas evolution and corresponding voltage profiles for NMC622. Reproduced with permission [101]. Copyright 2019, ACS. **(d)** Schematic illustration of selected reactions resulting in gas formation. **(e)** The dependence of gas evolution on the state of Ni oxidation. **(f)** Qualitative density of states diagrams for NCM111 and NCM811 at full lithiation. Reproduced with permission [103]. Copyright 2017, ACS.

layer is irreversible and can stay at the electrode surface. It is well understood that gaseous breakdown products originate from the intricate interplay between surface reconstruction and interface reactivity. CO_2 production might also result through a phase transition at the electrode surface, in addition to the breakdown of surface impurity products. Berg and coworkers discovered these processes at the electrode surface, as shown in Fig. 5**d** [104]. On one hand, CO_2 is produced when partially oxidized surface oxygen combines with organic carbonate electrolytes such as ethylene carbonate (EC), dimethyl carbonate (DMC), and diethyl carbonate (DEC). However, the lattice oxygen loss caused by structural changes results in O_2 evolution. Furthermore, the CO_2, O_2, and R–O intermediates formed during electrolyte breakdown are known to be highly reactive with electrolyte solvents, leading to the creation of the surface inactive layer. The beginning points of gas production, according to electrochemical mass spectroscopy (EMS), falls within a restricted range of the Ni-oxidation state (85–100 %). The creation of gas is aided by a higher Ni concentration (Fig. 5**e**). As shown in Fig. 5**f**, the authors also reported electronic density of state (DOS) estimations for NMC111 and NMC811 at three distinct states. They came to the conclusion that the pace of electron depletion from the Ni–O_2* surface state determines the rate of gas production (CO_2 and O_2). Competitive Co t_{2g} bulk oxidation and Co–O_2* surface states impact it to a lesser extent.

2.2. Thermal degradation

In addition to gas evolution, a significant issue associated with Ni-rich cathode materials is the development of microcracks induced by the anisotropic lattice volume change of each primary particle. As the repulsive force between the oxygen slab and the TM intensifies, the c-axis expands during the charging process. Simultaneously, the increased electrostatic attraction between the oxygen slab and the TM leads to a reduction in the a-axis [105]. The significant safety concerns associated with the widespread adoption of multilayer NMC cathodes arise from their intrinsically low thermal stability and the exothermic side reactions induced by the ensuing oxygen release (Fig. 6**a**). Liu et al. [106] conducted an investigation into Co/Mn exchange in a Ni-rich $LiNi_{0.83}Co_{0.11}Mn_{0.06}O_2$ cathode, providing a comprehensive analysis of this matter. Their findings revealed that Co, rather than the commonly emphasized Mn, plays a substantial role in influencing the chemical and structural stability of deeply delithiated NMC cathodes (Fig. 6**b**). Using in situ mass spectrometry in conjunction with operando synchrotron X-ray analysis, it was shown that Co^{4+} decreases before Ni^{4+} does. This might extend the Ni migration by occupying the tetrahedral sites, delaying thermal failure and oxygen release. Mn is stable in and of itself, but it seldom stabilizes Ni^{4+} [106]. These results highlight how crucial it is to evaluate the inherent effects of compositional tweaking in Ni-rich/Co-free layered oxide cathode materials in order to guarantee the secure functioning of high-energy Li-ion batteries. Mn has traditionally been regarded as a stabilizing element for the NMC structure [19]. On the other hand, new research by Amine and colleagues casts doubt on this notion, indicating that Co may have the primary effect on the thermal stability of highly delithiated Ni- rich NMCs [107]. The findings from their study reveal that the initiation temperature of the phase transition and the presence of unstable Ni^{2+} in Mn-rich cathodes occur at lower temperatures than in Co-rich cathode materials. Additionally, as depicted in Fig. 6**c**, the onset temperatures of the two oxygen outgassing phases (first period: purple bar; second period: red bar) are similar for Mn-rich and Co-rich NMCs. In contrast to the Co-rich cathode, which releases 13 % of its total oxygen in the first period, the Mn-rich cathode releases 36 % of its total oxygen. This early release of oxygen, due to its strong reactivity with the electrolyte and lithiated anode, poses a higher risk of thermal runaway. Therefore, the Mn/Co

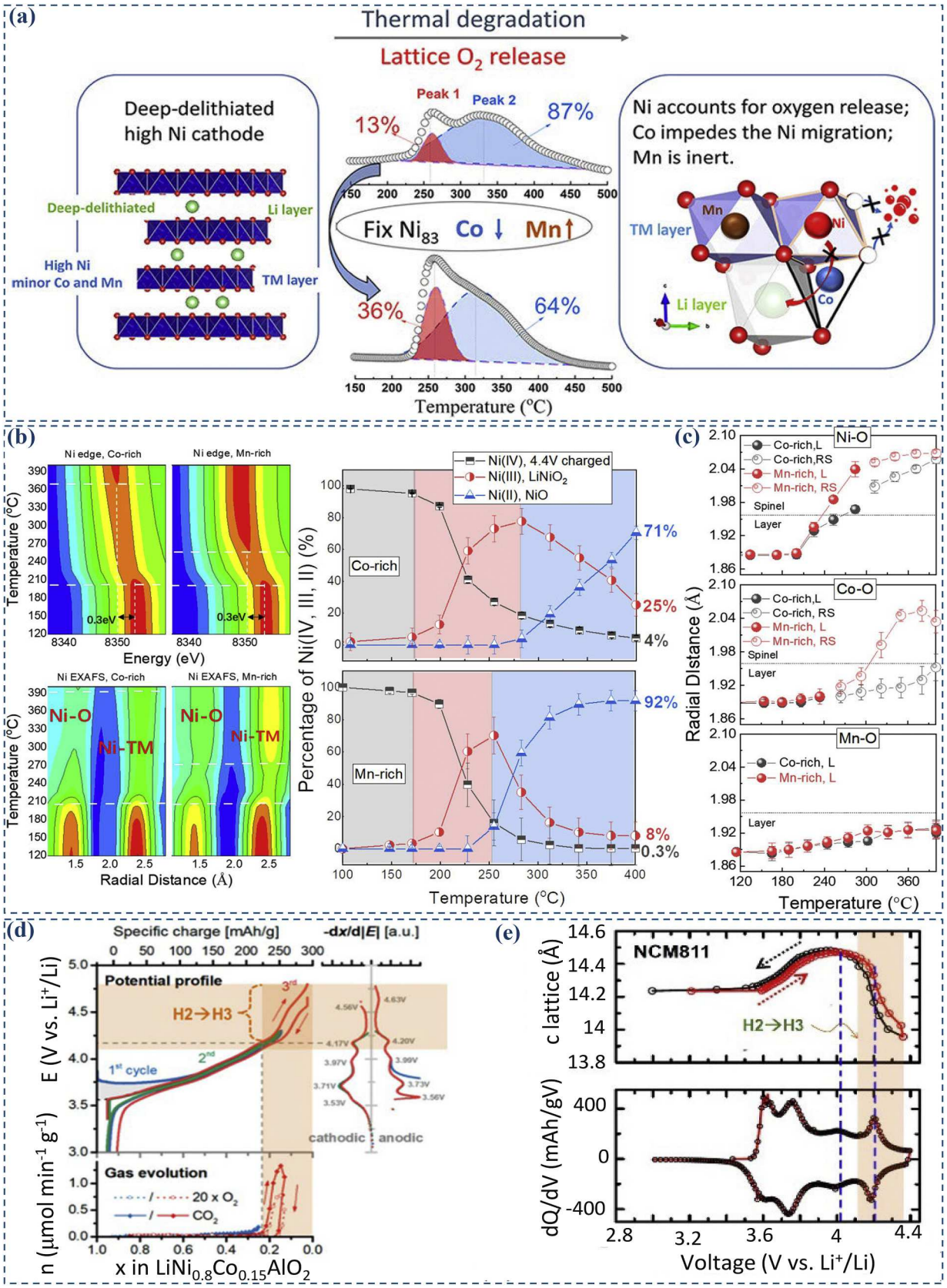

Fig. 6. **(a)** Thermal degradation leading to oxygen release in Ni-rich cathodes. **(b)** Operando XANES and EXAFS to reveal the chemical stability of the Co/Mn exchange in Ni-rich cathode. **(c)** Evolution of the TM-O bonding distance during heating, revealed by the EXAFS fitting. Reproduced with permission [106]. Copyright 2018, ACS. **(d)** Correlation of oxygen evolution with SOC, potential and differential capacity of Ni-rich cathode, where the shaded area corresponds to the H2→H3 transition region. Reproduced with permission [108]. Copyright 2018, ACS. **(e)** Correlation of c-lattice and potential of NCM811cathode. Reproduced with permission [109]. Copyright 2015, The Electrochemical Society.

ratio in Ni-rich cathodes significantly affects battery safety. Given these results, it is necessary to conduct a thorough investigation of Ni-rich batteries that have improved thermal stability. In Ni-rich cathodes, surface reconstruction is associated with a phase transition process primarily occurring at the material's surface. This phase transition leads to a transformation in the original crystal structure, transitioning from a layered structure to spinel and ultimately to rock-salt. Distinctive differential capacity patterns are observed in the highly delithiated state, as depicted in Fig. 6**d** and 6**e**, indicating that the H2-to-H3 transition is the driving force behind this process. The acceleration of this transition is notable at high Ni-content, high state of charge (SOC), and elevated temperatures, resulting from the combined influences of cation disorder and lattice oxygen loss.

2.3. Voltage fading mechanism

Voltage fading in Ni-rich cathode materials is a complex phenomenon, involving several mechanisms that contribute to the gradual decrease in the operating voltage of the cathode during charge-discharge cycles. Researchers have consistently observed the formation of the cathode SEI layer, even though conventional Ni-rich cathode materials are typically operated in the voltage range of 2.8 to 4.4 V, where there is no thermodynamic driving force for electrolyte electrodecompositions. This phenomenon endures even following electrochemical examinations or interaction with the electrolyte, underscoring the impact of the electro-oxidation process on the electrolyte [110,111]. Beyond the formation of the SEI layer, modifications to the local electrical structure can lead to structural alterations in the cathode (Fig. 7**a**).

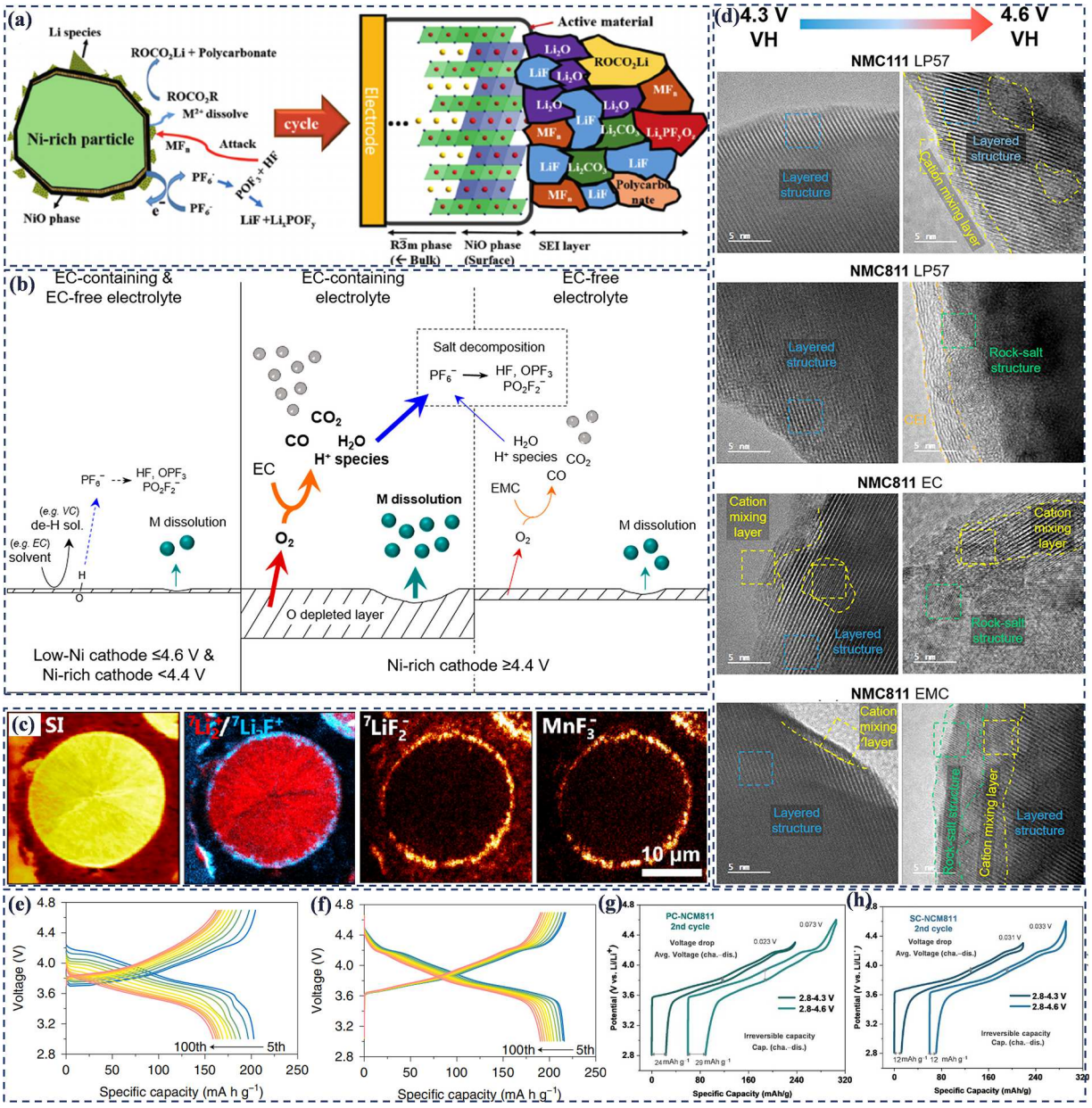

Fig. 7. **(a)** The microstructure and composition of the SEI at the surface of Ni-rich cathode materials. Reproduced with permission [74]. Copyright 2015, Wiley-VCH. **(b)** Degradation mechanism for Ni-rich cathode with EC-containing and EC-free electrolytes. Reproduced with permission [118]. Copyright 2022, ACS. **(c)** TOF-SIMS chemical mapping on Ni-rich secondary particle after cycling. Reproduced with permission [116]. Copyright 2017, ACS. **(d)** HR-TEM images of NMC after voltage hold at 4.3 and 4.6 V with different electrolyte additives. Reproduced with permission [118]. Copyright 2022, ACS. Corresponding voltage profiles of the cells using **(e)** $LiPF_6$/EC-EMC + VC and **(f)** LiFSI/DMTMSA electrolytes. Reproduced with permission [119]. Copyright 2021, Nature. Charge/discharge curves for **(g)** PCNMC811 and **(h)** SCNMC811. Reproduced with permission [33]. Copyright 2022, Wiley-VCH.

Lin et al. observed a phase transition in the $LiNi_{0.4}Mn_{0.4}Co_{0.18}Ti_{0.02}O_2$ cathode when it was exposed to the electrolyte [112]. Divalent Ni ions, owing to their ionic radii comparable to those of Li^+, exhibited a preference for forming the cation mixing layer over cobalt and manganese ions [74]. This observation suggests that the surface reconstruction layer is formed due to the spontaneous reductions of nickel ions among transition metal ions. This phenomenon significantly increases the charge transfer resistance. The evolution of the valence band structure was linked to the generation of a surface layer composed of organic species during the charging process, establishing a tight correlation between the valence band structure and surface composition [113]. The presence of acidic species, such as HF, formed during the breakdown of $LiPF_6$ salt and PVDF binder, could potentially dissolve TM ions in the cathode structure [78]. At present, it is understood that the structural instability of Mn ions is the underlying cause for the preferential dissolution of trivalent Mn ions from the cathode among the TM ions [114]. The disproportionation reactions ($2Mn^{3+} \rightarrow Mn^{2+} + Mn^{4+}$) were induced by the Jahn-Teller distortions of the trivalent manganese ions, leading to the removal of divalent Mn ions from the cathode [115]. In a study by Li et al. [116], it was clearly observed that various chemicals were generated at the surface of the $LiNi_{0.61}Co_{0.12}Mn_{0.27}O_2$ cathode after long-term cycling. Specifically, Li fluoride and Mn fluoride were produced at the cathode surface, where acidic species significantly dissolved the TM ions and Li ions after 3000 cycles at ambient temperature. Moreover, as depicted in Fig. 7**b**, the concentration of these fluoride compounds increased with the growing cycle number. Undesirable fluoride-containing substances may contribute to a decline in battery performance by obstructing processes involved in charge transfer at the cathode surface [117].

Furthermore, the conducting material in the electrode, such as carbon black, may experience weakening due to the presence of dissolved TM ions, leading to a reduction in the electrode's electrical conductivity [120]. The reciprocal exchange of surface species between the cathode and the conducting agent, such as TM fluoride, resulted in the passivation of the conducting agent. More concerning is the observation that this behavior occurred specifically when the electrode was in contact with the electrolyte during the electrochemical test. Li and colleagues demonstrated the dynamic behavior of the cathode-electrolyte interface using region-of-interest sensitive time of flight secondary ion mass spectrometry (TOF-SIMS). As depicted, the intensity of the fluoride containing species increased after the electrode was immersed in the electrolyte for 30 days compared to a pristine electrode. The surface species responsible for C_2F and COF_3 can originate from two distinct sources: (1) an acidic species attacking the carbonated electrolyte, or (2) a direct HF assault on the conducting agent. Interestingly, compounds containing fluorine, like C_2F and COF_3, were found at the cathode surface, indicating migration from the conducting agent. The presence of organic compounds decreased with reduced conducting agent, suggesting acidic species directly attacked the conducting agent, the primary source of fluorine-containing organic compounds. Dissolution products, including LiF and MnF_2, moved from the cathode towards the carbon-binder interface areas, appearing as metal fluoride compounds. The electrode with 10 wt% conducting agent showed higher metal fluoride compound intensity compared to the 1 wt% counterpart, suggesting that a conducting agent with a larger surface area is a more effective HF scavenger than Ni-rich cathode materials (Fig. 7**c**). Therefore, to achieve outstanding electrochemical performance, attention must be paid to the microstructure of the cathode surface, coupled with appropriate electrode design. The anode integrity may degrade not only due to the deteriorating cathode and conducting agent but also because of dissolved TM ions from the cathode. It is well-established that the full-cell setup with Ni-rich cathodes may experience substantial capacity fading due to the migration of TMs from the cathode to the anode side. The migration of dissolved TM ions from the cathode side to the anode side occurred during battery cycling, settling on the anode. These deposited TM ions, during the electrochemical test, contributed to the breakdown of the electrolyte solvent. Enhanced decompositions of the electrolyte solvent at the anode side could result in the formation of an unstable, thick, and unevenly layered anode SEI layer, potentially impeding Li^+ transport [121].

Increasing the upper cut-off voltage (UCV) of the cell led to poor electrochemical performance. Dissolved TM concentrations on the cycled graphite anode revealed that, below a UCV of 4.3 V, Mn ions were the most unstable, exhibiting the highest concentrations. Notably, at a UCV of 4.4 V, dissolved TM ions on the anode showed stoichiometric characteristics similar to the cathode material (Ni:Co:Mn=50:20:30). This suggested that newly exposed primary particles formed by microcrack evolution reacted with acidic species. The heightened TM dissolutions at high UCV contributed to severe capacity fading in the full-cell, likely due to irreversible Li consumption at the anode. Fuller et al. investigated the morphological change of the anode SEI layer triggered by dissolved TM ions by artificially adding TM salts as electrolyte additives in a full cell with $LiNi_{1/3}Co_{1/3}Mn_{1/3}O_2$ cathode and graphite anode [122]. The HR-TEM images in Fig. 7**d** compare the interfacial structure of NMC particles in the discharged state after volage holds at 4.3 and 4.6 V. This indicated that TM ions contributed to additional solvent breakdown, causing an unstable cathode surface and resulting in significant overpotential and capacity fading during the electrochemical test [123].

More importantly, the cycled graphite anode was shown to contain metallic Li, or dead Li, during the extended cycling. Because of the irreversible Li consumption on the graphite anode during the electrochemical cycling, the metallic Li deposition on the anode severely reduces the full-cell's capacity and power [124]. Furthermore, the battery's internal short circuit may result from the development of a metallic Li microstructure [125]. It was shown that the dissolved Mn-ion were the source of the metallic Li development on the anode. They found that the anode SEI layer is disrupted and forms new layers as a result of the dissolved manganese ions, and that the higher interfacial resistance of the unstable anode SEI layer causes metallic Li deposition. The distribution of Li elements in various compounds, including metallic Li at the cycled anode and the SEI layer component (LiF), is depicted in. On the graphite-electrolyte interface, the organic SEI layer components were localized; in contrast, on a heavily cycled anode, metallic Li developed beneath the anode SEI layer. It is noteworthy in particular that no electrochemical strain, such as quick charge or overcharge, occurred during the formation of the metallic Li under standard electrochemical test circumstances. Because of this, maintaining the cathode-electrolyte interface (CEI) stability is essential for high-energy and secure LIBs. In a study, Xue et al. [119] stabilized the cycle performance at ultrahigh voltage (4.7 V) by using sulfonamide-based electrolyte (Fig. 7**e** and **f**). Additionally, Sun et al. [33] have also discovered that preparing single-crystal (SC) Ni-rich cathode can also improve the cycle stability at high voltage (Fig. 7**g** and 7**h**).

TMs, including Ni, Co, and Mn, exhibit increased dissolution during chemomechanical breakdown. Among these metals, Mn ions dissolve more readily, and two possible reasons can account for this phenomenon [126,127]. The Mn^{3+} disproportionation reaction, as per the $2Mn^{3+}/Mn^{2+}/Mn^{4+}$ pathway, is the initial mechanism. The cathode is attacked by HF as the second mechanism. $LiPF_6$, a typical liquid electrolyte component, breaks down readily into $LiPF_6/LiF+PF_5$. PF_5 can further break down into $PF_5+H_2O/2HF+POF_3$ in the presence of water [75]. The dissolution of transition metals, such as Mn, can occur due to an HF reaction with the cathode. This process generates H_2O as a byproduct, leading to an auto-catalytic loop that accelerates PF_5 breakdown and produces more HF. The dissolved Mn ions have adverse effects, contributing to the formation of a resistive layer on the cathode surface and hindering SEI layer formation on the anode [128]. This interference on the anode surface results in the formation of an inactive layer and fractures in the SEI layer, leading to the breakdown of SEI components like $(CH_2{-}OCO_2Li)_2$, forming Li_2CO_3. Li_2CO_3 can react with $LiPF_6$, producing LiF and CO_2. The breakdown of TMs disrupts SEI layer

formation and promotes the generation of additional SEI, ultimately impacting electrochemical performance [122]. As a result, the dissolution of TMs intersects the SEI growth and induces more SEI formation, which leads to decreased electrochemical performance [96]. While Co ion dissolution is not predominant, it is frequently observed in cathode materials containing Co [129]. Additionally, the transition from a layered structure to spinel and/or rock-salt structure often accompanies Ni ion dissolution, which can be accelerated by factors such as high Ni concentration, high cut-off voltage, and elevated temperature [130]. For instance, $LiNi_{0.9}Mn_{0.05}Co_{0.05}O_2$ exhibits a significantly higher degree of Ni dissolution than NMC622, even though its Co and Mn concentration is only one-fourth that of NMC622. The increased dissolution of Co and Mn ions in $LiNi_{0.9}Mn_{0.05}Co_{0.05}O_2$ may be attributed to more fractures in the material, providing additional routes for cathode-electrolyte reactions and electrolyte infiltration [131].

2.4. Capacity fading mechanism

The observed capacity fading of NMC cathodes is generally explained by oxygen release destabilizing the crystal structure and parasitic surface reactions causing the accumulation of a NiO-like phase on the cathode material's surface [132–134]. Recently, anisotropic lattice contraction during cycling, identified as the primary mechanism for $LiNiO_2$, may also contribute to the structural degradation of NMC cathodes [135,136]. Multiscale modeling based on first-principle calculations suggests that anisotropic volume shifts create mechanical stress, leading to microcracking and eventual intergranular fracture-induced disintegration of Ni-rich NMC particles. Using the

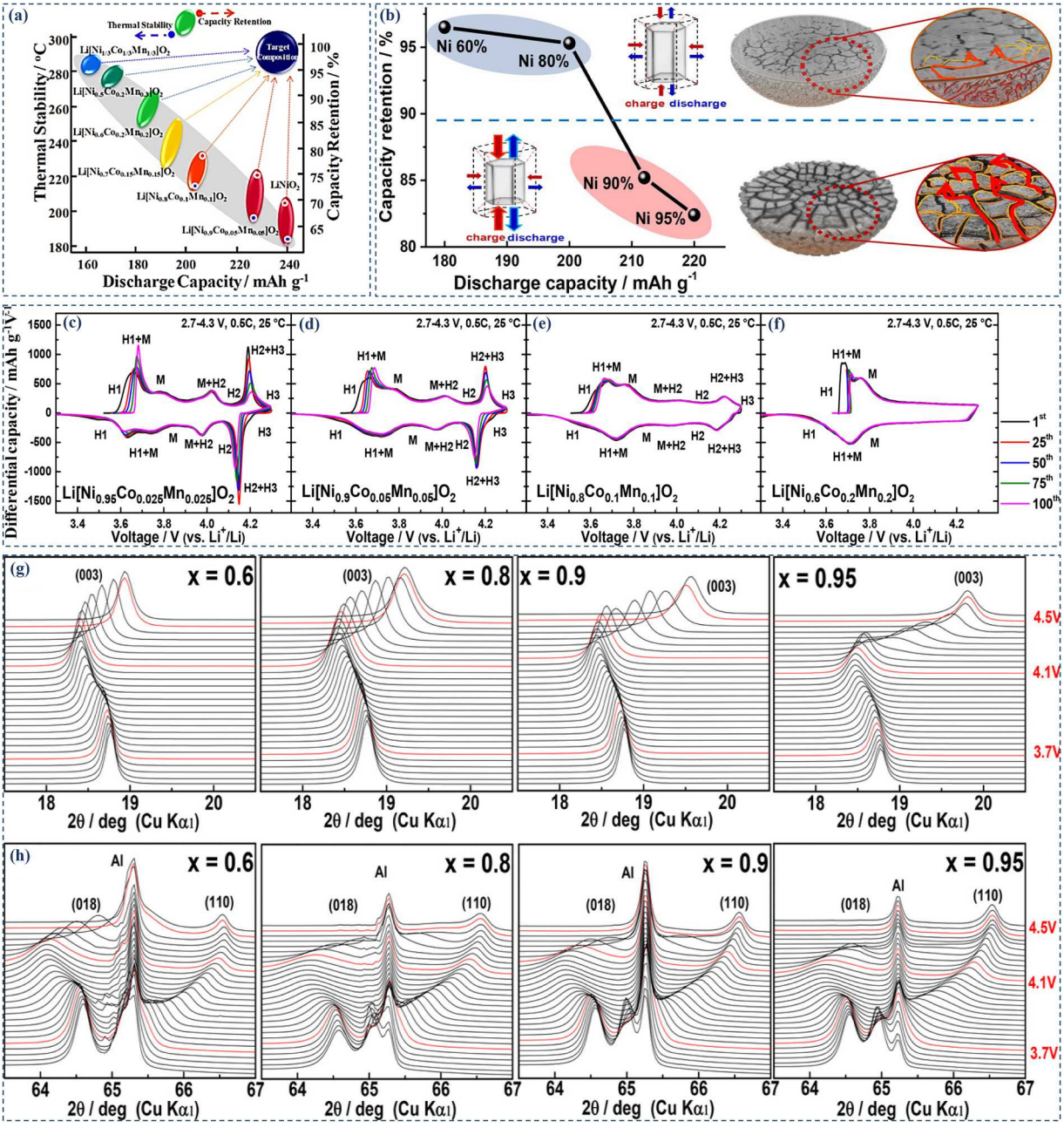

Fig. 8. **(a)** Electrochemical stability and capacity comparison of different NMC cathode materials. Reproduced with permission [139]. Copyright 2013, Elsevier. **(b)** Schematic illustration of capacity fading mechanism in Ni-rich cathodes. **(c-f)** dQ/dV profiles and **(g, h)** In situ XRD patterns of $Li[Ni_xCo_yMn_{1-x-y}]O_2$ ($x = 0.6$, 0.8, 0.9, and 0.95) during the first charge cycle charged from 2.7 to 4.5 V at 0.2C for (003) reflection and (110) reflection. Reproduced with permission [24]. Copyright 2018, ACS.

density functional theory (DFT) approach, Major and coworkers investigated NMC materials with varying Ni concentrations and enlarged the critical influence of Ni content [137]. The quantities of high-valence Ni ions (Ni^{4+}) in NMCs are illustrated. As the Ni content increases from low-Ni NMCs to Ni-rich NMCs, the amount of Ni^{4+} also increases. Notably, when the SOC increases, the concentration of Ni^{4+} decreases rapidly. The presence of Ni^{4+} is associated with rapid deterioration during charging due to its low-lying lowest unoccupied molecular orbital (LUMO), allowing it to readily react with oxygen or electrolyte species.

According to recent studies, NMCs with higher Ni percentages showed reduced capacity retention during cycling. Fig. 8**a** summarizes the key electrochemical characteristics of Ni-rich NMC-based electrodes. Experiments of NMCs with different Ni concentrations, as reported by Sun et al. [24] reveals that Ni-rich cathodes quickly lose their capacity when the composition gets closer to $LiNiO_2$, showing the drop of the capacity retention to 75 % after 100 cycles and making it unsuitable for real-world applications (Fig. 8**b**). Greater Li consumption (greater SOC), in addition to the Ni content in the compounds, is a significant contributor to mechanical fracture acceleration. In a similar way, Manthiram et al. [138] found the abrupt lattice collapse of NMCs with different concentrations of Ni. In many NMCs, structural damage is noted when Li consumption reaches 80 % at a high cut-off voltage. The charge-discharge voltage curves (Fig. 8**c-f**) show that Ni-rich NMCs ($x >$ 90 %) have a higher specific capacity despite the decreased stability. The investigations conducted by the authors indicate that there is a linear relationship between the discharge capacity of Ni rich NMCs and the Ni content in the compounds. In addition, NMC appears to have a lot of potential to grow based on its theoretical capacity of 275 mAh/g. Therefore, additional Ni content is needed for further development, which become one of the most crucial study fields. Moreover, higher Ni content results in higher rate capacity when compared with the rate capabilities of NMC622 and $LiNi_{0.90}Co_{0.05}Mn_{0.05}O_2$ [131].

A detailed understanding of NMC phase changes throughout the charge and discharge operations is crucial for mechanistic study. Before the study of Dahn and coworkers in 1993, the structural evolution of layered $LiNiO_2$ as a function of voltage has only been explored in two-phase domains. Using in situ XRD data, they showed four-phase regions for the first time for the operation of $LiNiO_2$ electrodes. Subsequent NMC studies have widely acknowledged this phase diagram since then. The areas that comprise the four phases are described below. $Li_{1-x}NiO_2$ undergoes many phase changes throughout the delithiation process: hexagonal-1 (H1), hexagonal-2 (H2), and hexagonal-3 (H3). Three hexagonal phases are defined by the evolution of lattice parameters in $Li_{1-x}NiO_2$. They can be followed using the differential capacity (dQ/dV) curves [140]. These graphs may be used to electrochemically determine the phase transitions of related layered Ni-rich materials. The phase changes in $LiNi_{0.95}Co_{0.025}Mn_{0.025}O_2$, $LiNi_{0.9}Co_{0.05}Mn_{0.05}O_2$, and $LiNi_{0.8}Co_{0.1}Mn_{0.1}O_2$) with respect to NMCs with a Ni ratio higher than 80 % are the same as those in $LiNiO_2$, with the initial H1 phase changing into M, H2, and H3 phases. Three phase-coexistence zones are found at 3.7 V (H1+*M*), 4.0 V (*M* + H2), and 4.2 V (H2+H3). The abrupt shrinkage on the c-axis in the unit cell, causing detrimental anisotropic lattice volume changes, is primarily responsible for the shift from H2 to H3 under a high voltage regime. The absence of the apex of the H2-to-H3 transition in the phase diagram of NMC622 suggests that the H2–H3 transition becomes more apparent as Ni concentration increases, emphasizing its importance for structural stability. Therefore, examining lattice collapse in Ni-rich NMCs at high SOC is crucial [141]. Beyond 4.11 V, the electrode undergoes the H2–H3 transition, followed by lattice oxygen reduction. This transition leads to lattice collapse, detrimentally affecting reversible storage capacity. The c-axis lattice shrinkage during the H2-to-H3 phase transition is linked to the lattice collapse of Ni-rich NMCs, as indicated by theoretical and experimental research. The distance between Li layers in the electrode material is associated with the c-axis parameter, showing a consistent evolutionary pattern with unit cell volume across various compositions and Ni-contents. It has been found that NMC811 experiences a bulk O3 to O1 phase change at high voltages and temperatures [142]. This phase transition is kinetically sluggish, as evidenced by the fact that the phase fraction of the O1 phase depends on temperature, duration, and hold voltage in addition to the material's lithium content. The O3 to O1 phase transition suppressed in fully charged NiO_2 when Ni ions move from their initial octahedral locations in NiO_2 slabs to face-sharing tetrahedral sites in Li layers. Fig. 8**g** and **h** illustrate the in situ XRD measurements tracking the development of the c-axis lattice parameter with voltage and Li concentration during delithiation [143]. At 4.1 V, as the cathode reaches a higher SOC, there is a sudden decrease in the length of the c-axis lattice. Numerous studies have consistently demonstrated similar findings, reinforcing the understanding that the highly unstable H2-to-H3 phase transition in Ni-rich layered materials is correlated with changes in anisotropic lattice characteristics during deep delithiation. In a novel approach, Yoon and collaborators [144] investigated the evolution of lattice parameters in $LiNi_{0.5+x}Co_{0.2}Mn_{0.3-x}O_2$ (x = 0, 0.1, 0.2) materials during discharging. By keeping Co content constant in various Ni-rich NMCs, they provided a comprehensive analysis of Ni's impact, independently of Mn, on the charge composition process [145]. The study revealed that the c-axis parameter's significant decrease at high SOC is primarily attributed to the shrinking thickness of the TMO_6 slab, shedding light on the intricacies of Ni-rich cathode lattice changes during the electrochemical process. This enhanced understanding is crucial for addressing degradation issues and exploring mitigation strategies as Ni-rich cathodes aim for higher Ni content. Even if it is indirect, there is some correlation between the mechanical deterioration of the cathode material and the capacity fading. Anisotropic volume variations during (de)lithiation create stress in the material, which causes interparticle contact loss due to particle fracture and unfavorable side reactions such as the creation of a cathode SEI layer [146].

3. Innovative modification strategies

Researchers have devoted considerable efforts to enhancing the electrochemical performance of Ni-rich cathode materials, addressing challenges through multifaceted approaches. Substantial progress has been achieved in areas such as enhancing cycle stability, preserving capacity over cycles, improving ionic conductivity, and mitigating voltage decay. A key solution to challenges like low cycle life and capacity retention in Ni-rich cathodes involves designing materials with minimal particle cracking and sustained cycling performance. Various strategies, including doping with inactive ions, intergranular modification, concentration gradient design, production of SC materials, and dual modification, have been proposed and applied to achieve these goals, paving the way for the practical utilization of Ni-rich cathodes in LIBs.

3.1. Multifunctional doping strategy

Numerous components, including metal and non-metallic ones, have been partially or completely integrated into the structure of the Ni-rich layer oxides with the aim of overcoming capacity fading. Others may prevent the migration of the Ni^{2+} ions to the Li layer, which lowers the degree of cation mixing, and some of the element's doping can provide a surface protective layer to prevent penetration and corrosion of the electrolyte. Additionally, these doped elements may function as pillar ions to control anisotropic strain and reinforce the bulk structure, which is crucial for preserving the crystal structure. To enhance mechanical and electrochemical performance, the most optimum dopant should be traded off and applied to any of the Ni-rich layer oxides, according of the needs. To address thermal and structural instability in Ni-rich cathodes, one widely explored method is the doping of inactive ions into the layered structure [147,148]. This involves substituting atoms in the crystal lattice with stable dopants to mitigate various issues associated

with Ni-rich cathodes. For example, substitution at Mn sites can impede cation mixing and gas evolution, while substitution at Co sites reinforces phase stability and charge transfer. The selection of doping elements profoundly influences the structural stability of Ni-rich cathode materials. Researchers have investigated the effects of different dopants (Al, Fe, Cu, Mg, Si, Ti, V, Zr, and Ga) on Ni-rich NMC, revealing that no single dopant can comprehensively resolve all issues [43,149,150]. Instead, each dopant tends to improve specific aspects while potentially exacerbating others. In many cases, substituting at the Co site enhances charge transfer and phase stability, while substitution at the Mn site helps prevent oxygen evolution and cation mixing. A promising strategy for doping modification involves substituting Ti or Zr in the Co site and Al in the Mn site. The selection of different doping elements for Ni-rich cathodes can significantly influence their structural stability and electrochemical performance. Both compositionally complex (high-entropy) doping and cation/anion co-doping strategies offer promising avenues for enhancing the structural stability and electrochemical performance of Ni-rich cathodes. However, careful optimization of doping parameters and thorough characterization are essential to harness their full potential and address associated challenges effectively. In this context, the primary focus is on doping agents that can generate particles without cracks, thereby improving electrochemical performance and reducing crack formation in Ni-rich layered cathodes.

In a recent study, Park et al. [151] provided a detailed study to push the Ni-composition upto 94 % with Ta-doping in core-shell (Ta-CSN94) cathode with a retention rate of 92.6 % after 1000 cycles. A cation disordered structure can be observed in selected area electron diffraction (SAED) patterns for CSN94 resulting in capacity fading as compared to Ta-CSN94, which showed a stable capacity even for long-term cycling (Fig. 9**a-k**). The presence of superlattice along [001] zone corresponds to the absence of TMs. The anion dopants, particularly fluorine (F), are considered effective candidates for this purpose [152]. DFT calculations were employed to assess the impact of F doping on the electrochemical characteristics of the $LiNiO_2$ (LNO) cathode. The results indicated that F doping had a positive impact on redox potential, ionic conductivity, lattice distortion, and Ni migration during delithiation, exhibited a negative influence on Li/Ni exchange. Kim et al. [152] discovered that F doping in compositionally graded $Li[Ni_{0.80}Co_{0.05}Mn_{0.15}]O_2$ (GC80) resulted in extended battery life, with retention rate of 78 % after 8000 cycles, attributed to cation ordering induced by F doping. HAADF-TEM images of the virgin and cycled F-doped GC80 cathodes are presented in Fig. 9**l**. The observed additional superlattice peaks suggest the presence of TM-ions between two TM layers. The most plausible explanation is that Ni ions migrate into the Li layer in a precisely ordered pattern, causing Li ions to occupy alternate TM-sites and resulting in the generation of a super unit cell. This ordered structure not only facilitates paths for Li-ion migration to the TM layer, enhancing Li migration, but also stabilizes the delithiated structure by acting as pillars to prevent the collapse of the layered structure at high SOC. Electrochemical testing demonstrates the impressive cycling stability of the F-doped GC80 cathode (Fig. 9**m**) after 2000 cycles.

Recent studies suggest that the presence of a spinel or rock-salt phase significantly enhances the structural stability of Ni-rich cathodes [154–156]. Doping with elements like boron (B) [157–160], tungsten (W) [155,161], and tantalum (Ta) [83], allows for the creation of microstructure-modified cathodes. Unlike other dopants, these elements can reduce the size of parent particles, forming secondary particles with unique microstructures. B, for instance, is effective in preventing the

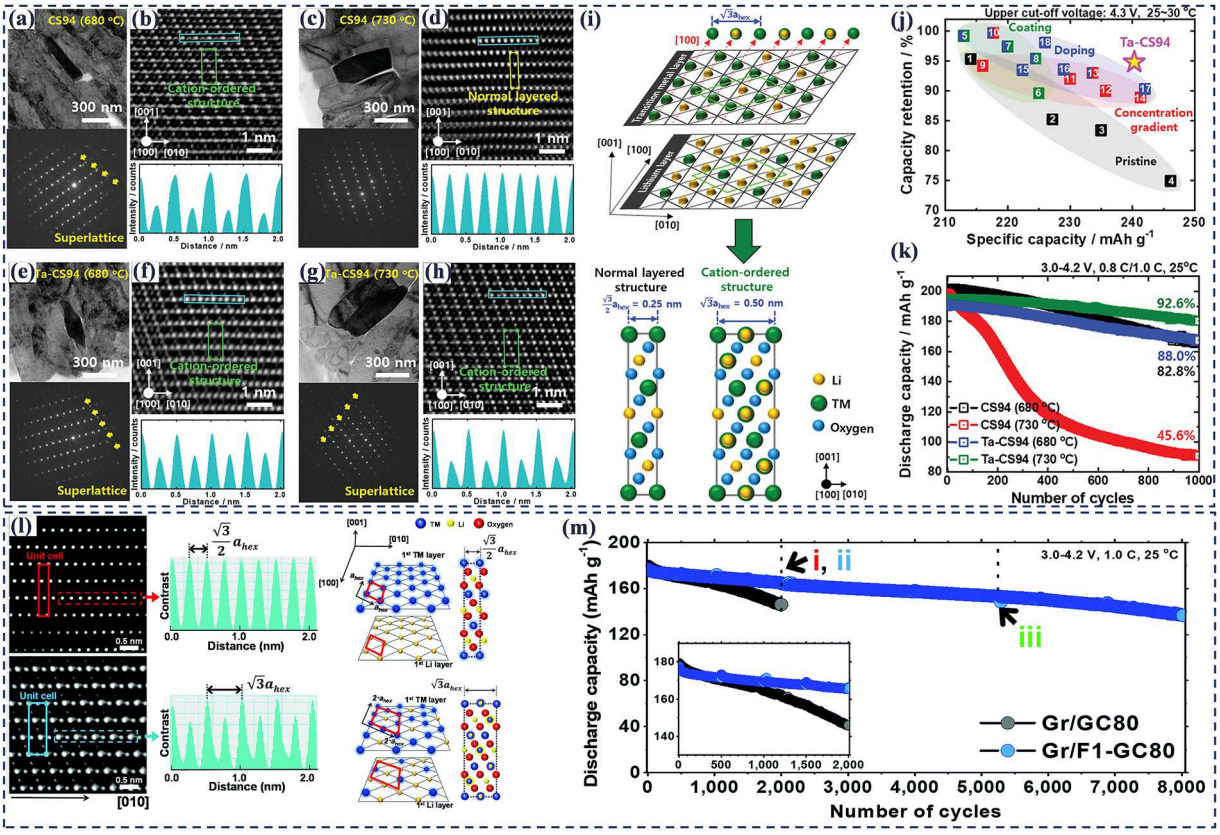

Fig. 9. (a-h) TEM images with SAED patterns and magnified Fourier-filtered [100] zone HAADF-TEM images of CS94 and Ta-CS94 cathodes, respectively. **(i)** Schematic depiction of atomic arrangements of layered structure and cation-ordered structure. **(j)** Comparison of half-cell performances of pristine cathodes, Ta-CS94 cathode, and other cathodes. **(k)** Long-term cycling performances of cathodes using full cells under. Reproduced with permission [151]. Copyright 2023, Wiley-VCH. **(l)** Atomic arrangement between F-doped GC80 (up; before cycling) and F-doped GC80 (down; after 2000 cycles). **(m)** Cycle performance of GC80 and F-doped GC80. Reproduced with permission [153]. Copyright 2021, RSC.

formation of microcracks (Fig. 10**a-c**) [157]. Introducing Li $[Ni_{0.9}Co_{0.09}W_{0.01}]O_2$ (NCW90) as a novel layered oxide cathode has demonstrated exceptional cycle performance, retaining 92 % of the original capacity after 1000 cycles and exhibiting a larger initial discharge capacity than $Li[Ni_{0.885}Co_{0.10}Al_{0.015}]O_2$ (NCA89) (231.2 mAh/g at 0.1C) [161]. Substituting W for Al refines particle size, leading to the development of inter-particulate microfractures in secondary particles (Fig. 10**d-g**). Additionally, W serves as a potent dopant to inhibit the initiation and propagation of microcracks. $Li[Ni_{0.90}Co_{0.05}Mn_{0.05}]O_2$ cathodes with 1.0 mol% W-doping (W1-NCM90) show significantly enhanced chemical stability with minimal initial capacity loss, achieving 89 % capacity retention after 500 cycles in a full-cell cycled at 4.3 V [155]. The suppression of microcrack development and reduced internal strain contribute to the chemical stability (Fig. 10**h**). Kim et al. [83] introduced a unique microstructure by creating $Li[Ni_{0.90}Co_{0.09}Ta_{0.01}]O_2$, where secondary particles were aggregated by radially aligned parent grains with crystallographic texture. This innovative approach achieved long-term cycle stability at full depth of discharge. The tailored microstructure dissipated internal anisotropic strain under high delithiation conditions, inhibiting microcrack development and propagation and resulting in an unparalleled capacity retention of 90 % even after 2000 cycles.

Moreover, a quaternary layered $LiNi_{0.93}Al_{0.05}Ti_{0.01}Mg_{0.01}O_2$ (NATM) cathode demonstrated excellent performance compared to NC and NMC with Ni>90 % (Fig. 10**i-j**) [165]. It retained 82 % capacity after 800 cycles at C/2 for pouch cell. In another study, Ni-rich NMA showed an improved electrochemical performance than NMC and NCA cathodes in pouch cells paired with graphite, and only slightly trails than Al-Mg doped NMC and a commercial cathode after 1000 deep cycles (Fig. 10**k**). Substituting Al into the NMC cathode reduced the unit cell volume change caused by the H2-H3 phase transition, as revealed by in situ XRD examination. The single-particle compression test demonstrated increased intrinsic mechanical strength, leading to enhanced structural stability and improved thermal stability of the cathode by suppressing microcrack creation and propagation. Similarly, Zhang et al. rationally designed a structurally and electrochemically stable single crystal $LiNi_{0.6}Co_{0.1}Mn_{0.3}O_2$ cathode with zirconium and titanium co-doping (Z/T@SC—NCM) for high-energy density batteries (Fig. 10**l**). In summary, inactive ion doping techniques, aiming to stabilize Ni ion oxidation states, strengthen M-O bonds, reduce lattice distortion, or create unique structures like heterostructures and microstructures, prove effective in minimizing microcrack formation, enhancing the structural stability of the host material, and improving electrochemical cycling performance. However, reducing lattice distortion through doping becomes challenging when the cutoff voltage exceeds 4.3 V, as more Li ions are removed during charging.

Future doping studies should focus on enhancing the structural stability of Ni-rich cathodes at high voltages. Furthermore, by combining theoretical calculations (such as formation energies, band structures, electronegativity, ionic radius, and charge densities to assess the feasibility and effectiveness of doping with different elements) with molecular dynamics simulations and finite element analysis, researchers can effectively screen doping elements, simulate ion behavior, and predict the mechanical response of single crystal materials, facilitating the design and optimization of advanced functional materials for various applications. Ab initio molecular dynamics simulations generate trajectories of atomic motion over time to study diffusion mechanisms, ion migration pathways, and the effects of doping on ion transport properties. Analyze the resulting data to quantify ion concentration profiles, diffusion coefficients, and migration barriers in the doped material. Finite element method analysis can also be used to model the stress distribution and mechanical response of the doped SC material under external loads or during electrochemical cycling [166].

3.2. Surface coating and modification

Although defects in Ni-rich cathode materials can be reduced by structural modification techniques, surface side reactions that cause deterioration, including HF corrosion and CEI production, are still an open challenge. Protective layer coatings emerge as a practical solution to address these issues, effectively blocking both electrolyte breakdown and the dissolution of TM ions from Ni-rich cathodes [167]. It has been suggested that the surface protective layer and doping, in addition to the surface coating layer, might ensure the interfacial stability in the Ni-rich cathode materials (Fig. 11**a**) [78,168,169,170]. For instance, the $LiNi_{0.8}Co_{0.15}Al_{0.05}O_2$ (NCA) cathodes underwent the vanadium-based surface treatment [171]. Surprisingly, throughout the annealing process, the multivalent vanadium ions interacted with the remaining Li-compounds, moderating the interactions with the HF and guaranteeing the interfacial stability. Another good example of surface treatment is subjecting NMC622 powder to a H_3PO_4 solution treatment followed by a heating treatment during which H_3PO_4 reacts with residual LiOH, Li_2O and Li_2CO_3 on the surface of NMC622 to form Li_3PO_4 coating, leading to substantial improvement in cycle stability [172].

Surface coatings for Ni-rich cathodes employ a diverse range of materials, including solid-state electrolytes (Li_3PO_4, Li_2ZrO_3, $LiNbO_3$, etc.), phosphates ($AlPO_4$, $MnPO_4$, $Si_3(PO_4)_4$, etc.), metal oxides (Al_2O_3, MgO, TiO_2, etc.), and conductive organic compounds (polyimide, polyaniline, etc.) [177–183]. Ionic conductive materials, such as solid-state electrolytes and conductive organic compounds with strong Li-ion conductivity, are combined with nonconductive substances like metal oxides, fluorides, and phosphates, known for high stability, to form protective coatings on Ni-rich cathode surfaces. A wide range of methods have been devised to deposit surface coatings, including atomic layer deposition (ALD), chemical vapor deposition (CVD), solid-state coating method, coprecipitation, hydrothermal, solvothermal, and sol-gel techniques [184]. In a study by Kim et al. [173] confirmed more stable interfaces in Li_2CO_3/$LiNbO_3$-coated NCM622 cathode in all solid-state battery cells using β-Li_3PS_4 as the solid electrolyte (Fig. 11**b**). In this case, the carbonate content of Li_2CO_3-coated and Li_2CO_3/-$LiNbO_3$-coated NCM622 was identical, the former material exhibits noticeably greater CO_2 evolution due to the relevant carbonate species' breakdown during cycling and the resulting generation of SO_2. Lee et al. [174] have proposed a facile surface coating technique to enhance the stability and reversibility by using piezoelectric $LiTaO_2$ on Ni-rich cathode (Fig. 11**c**). In a study by Yim et al. [175] a dry coating method was employed to create a protective layer combining CaO and Li_3PO_4 on the NMC811 cathode surface, ensuring long-term cycling performance by mitigating electrolyte breakdown (Fig. 11**d**). A highly effective approach has also been applied by nano-coating of TiO_2 on Ni-rich cathode providing a complete protection to the outer surface (Fig. 11**e**). Another innovative approach involves incorporating materials with negative thermal expansion (NTE) into electrodes to stabilize Ni-rich cathodes due to their exceptionally low expansion properties. For instance, Bai's team modified the surface of NCM622 using a common NTE material, ZrV_2O_7 [185]. Additionally, research has explored various organic compounds to prevent electrolyte breakdown at the cathode electrode surface [186]. Park et al. [178] created an OTS-coated $LiNi_{0.82}Mn_{0.09}Co_{0.09}O_2$ (NMC82) cathode with improved storage cyclability. The introduction of a new interface will unavoidably raise surface resistance and disrupt ionic transport, which is a significant disadvantage of the protective layer coating technique. Consequently, it is imperative to regulate the layer thickness in a way that does not impede ionic transport over the surface. It should be noted that surface coatings not only improve the cycle stability but also increase the specific capacity and the rate capability of cells as well. Sahni et al. [187] show that Li_3PO_4 coating simultaneously increases the specific capacity, improves the cycle stability, and enhances the rate capability of NMC532 and NMC333 cells. The reason for such simultaneous improvements is likely due to the replacement of the surface reduced layer typically

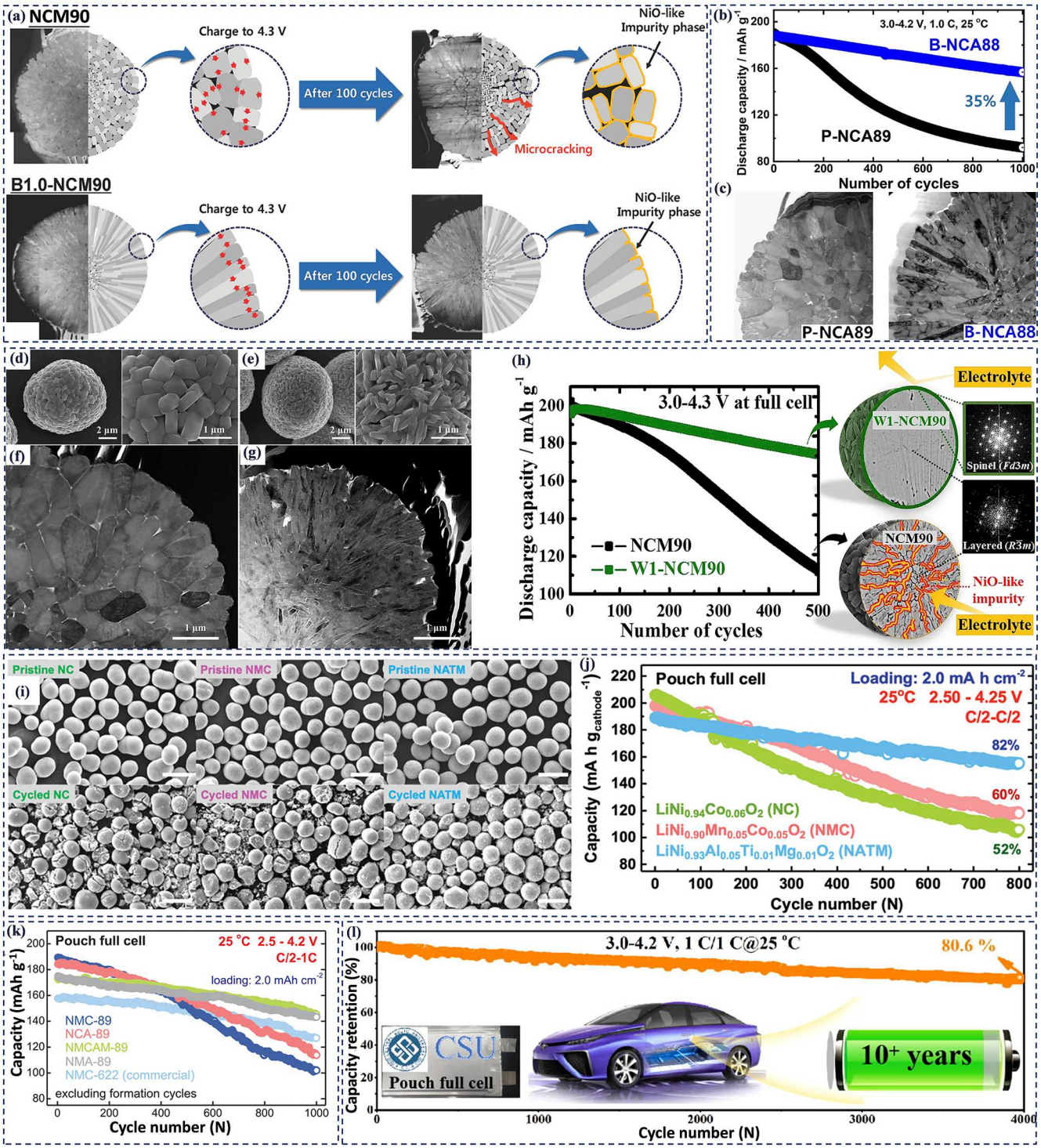

Fig. 10. **(a)** Comparison of the mechanical stability of B-doped NCM90 and NCM90 cathodes during cycling. Reproduced with permission [158]. Copyright 2018, Wiley-VCH. **(b, c)** The cycling stability and cross-section SEM images of pristine-$LiNi_{0.885}Co_{0.1}Al_{0.015}O_2$ (P-NCA89) and $LiNi_{0.878}Co_{0.097}Al_{0.015}B_{0.01}O_2$ (B-NCA88) cathodes. Reproduced with permission [159]. Copyright 2020, Elsevier. **(d-g)** STEM images of the particle and cross-section for NCA89 (left) and NCW90 (right). Reproduced with permission [161]. Copyright 2019, Wiley-VCH. **(h)** The cycle stability and capacity fading in W1-NCM90 and NCM90 cathodes. Reproduced with permission [155]. Copyright 2019, Elsevier. **(i, j)** SEM images and cycle stability comparison of NC, NMC, NATM cathodes. Reproduced with permission [162]. Copyright 2021, Wiley-VCH. **(k)** Cycle stability comparison of NMC-89, NCA-89-NMCAM-89, NMA-89 and commercial (NMC-622) cathodes. Reproduced with permission [163]. Copyright 2020, Wiley-VCH. **(l)** Cycle stability of Z/T@SC—NCM/graphite pouch cell for 4000 deep cycles. Reproduced with permission [164]. Copyright 2022, Elsevier.

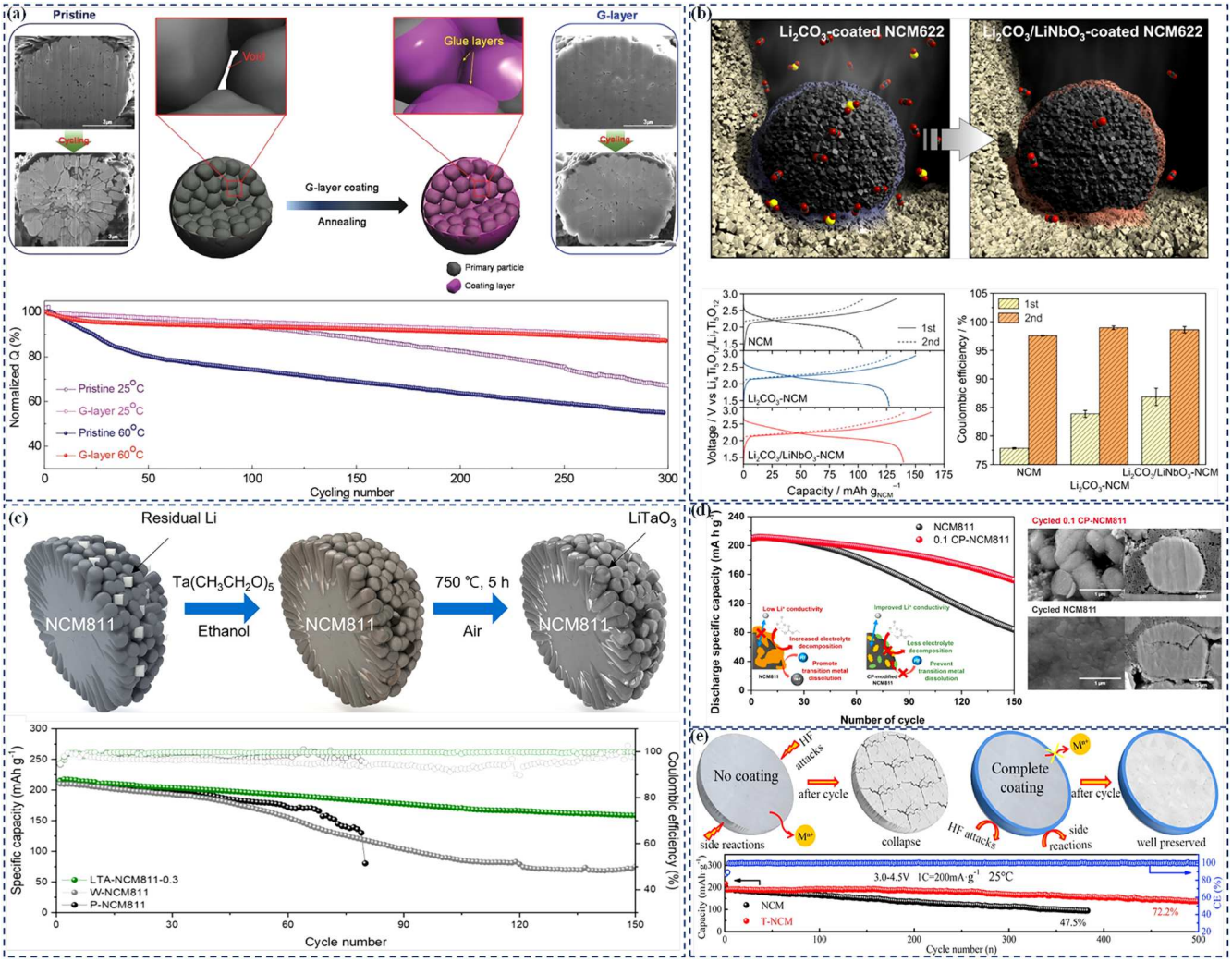

Fig. 11. **(a)** Schematic illustration of the glue layers on the NCA cathode during coating process showing the stabilized cycle performance. Reproduced with permission [168]. Copyright 2016, Wiley-VCH. **(b)** Li_2CO_3 and Li_2CO_3/$LiNbO_3$ coated NCM622 cathode particles with cycle voltage profiles and corresponding Coulombic efficiencies. Reproduced with permission [173]. Copyright 2019, ACS. **(c)** Schematic illustration of the $LiTaO_3$ surface coating onto NCM811 particles with improved cycle stability. Reproduced with permission [174]. Copyright 2022, ACS. **(d)** Surface modified NMC811 cathode by using functional $Ca_3(PO_4)_2$ precursor. Reproduced with permission [175]. Copyright 2021, Elsevier. **(e)** A protection mechanism of TiO_2 nano-coating on Ni-rich cathode with stable capacity. Reproduced with permission [176]. Copyright 2020, Elsevier.

formed during cell soaking by the Li-ion conductive Li_3PO_4 coating and the reduced amount of insulating residual Li compounds on the NMC surface. Simultaneous improvements in the specific capacity and cycle stability have also been reported for $LiAlO_2$/Al_2O_3-coated nano-$LiCoO_2$ because of minimization of the surface reduced layer and the protection of Li-ion conducting $LiAlO_2$ and stable Al_2O_3 coatings [188].

3.3. Grain boundary modification

Although the typical surface coating, which reduces the parasitic side reactions with the external electrolyte to protect the cathode surface, is a commonly used modification approach, it can rarely prevent grain boundary cracking. Grain boundary modification, specifically coating primary particles, has emerged as an effective coating strategy to mitigate the formation of intergranular microcracks. This approach involves covering the main particles in polycrystalline materials through a combination of surface coating and high-temperature treatment. Kim et al. proposed a novel surface treatment for the main particles of the NMC622 cathode [189]. The surfaces of primary particles exhibit enhanced cobalt content and a cation-mixing phase with a nanoscale thickness when the cathode material is combined with lithium and cobalt acetate in an ethanol solution, followed by calcination at 800 °C (Fig. 12**a**). This process significantly contributes to the structural stability of the cathode material by suppressing the development of intergranular microcracks in the secondary particles during charging and discharging, as shown in Fig. 12**b**. Additionally, the high oxidation state of Mn^{4+} on the surfaces of primary particles strengthens the Mn-O bonding, leading to reduced oxygen evolution during phase transitions. The structural and interfacial stability of $LiNi_{0.76}Mn_{0.14}Co_{0.10}O_2$ (NMC76) cathode material is reported to be greatly increased by injecting Li_3PO_4 into the grain boundaries by Yan et al. [190] To facilitate the penetration of Li_3PO_4 into the grain boundaries of secondary particles, NMC76 secondary particles are coated with Li_3PO_4 using atomic layer deposition (ALD), followed by annealing at 600 °C. After 200 cycles, the Li_3PO_4 infused electrode exhibits capacity retention of 91.6 % at ambient temperature and 73.2 % at 60 °C, which is 12.6 % and 14.9 % higher than the pristine cathode, respectively. After 200 cycles, pristine primary particles undergo significant structural evolution as the layered-to-spinel phase transformation initiates at the particle surface, as indicated by electron diffraction and high-resolution structural imaging. However, in the Li_3PO_4 infused cathode, the electrolyte cannot permeate into the grain boundaries within the secondary particles

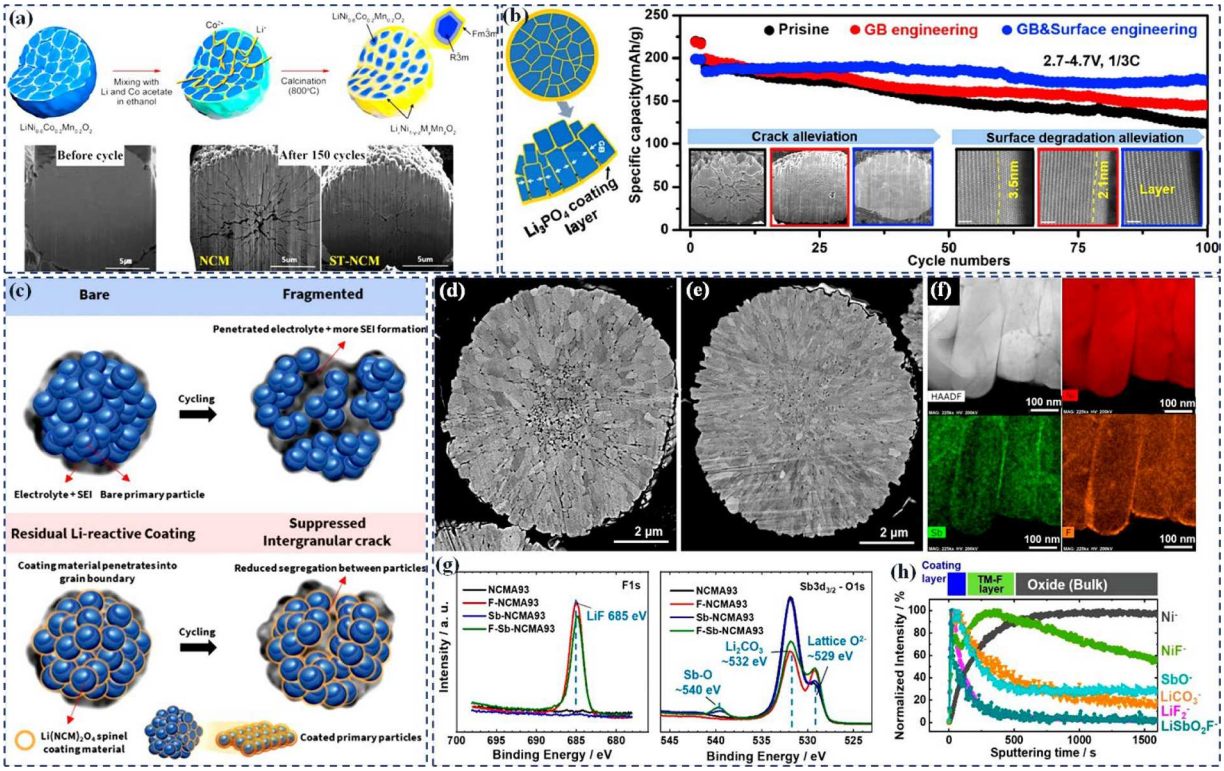

Fig. 12. **(a)** Surface modification on the primary particles with cross-sectional SEM images of the NCM622 before and after 150 cycles at 60 °C. Reproduced with permission [189]. Copyright 2015, ACS. **(b)** Li_3PO_4 coated NMC811 cathode with cycle performance and cross-section SEM and TEM images. Reproduced with permission [190]. Copyright 2019, Elsevier. **(c)** Schematic view of the effect of NMC surface coherent spinel coating to prevent intergranular crack. Reproduced with permission [191]. Copyright 2018, ACS. Cross-sectional images of **(d)** NMCA93 and **(e)** Sb-NMCA93, **(f)** EDS mapping of Ni, Sb, and F in F-Sb-NCMA93. **(g)** F 1 s, and Sb $3d_{3/2}$—O 1 s XPS spectra of NCMA93, F-NCMA93, Sb-NCMA93, and F-Sb-NCMA93. **(h)** Normalized depth profiles of representative species in as-synthesized F-Sb-NCMA93. Reproduced with permission [192]. Copyright 2023, ACS.

without intergranular cracks, preventing the phase change in the primary particles. This reduction in the cathode-electrolyte interfacial reaction and subsequent decrease in electrolyte degradation implies that the active materials inside the secondary particles are well-preserved after Li_3PO_4 infusion. Overall, the primary particle coating focuses on individual particle protection and tailored electrochemical properties, secondary particle coating emphasizes improving the structural integrity and conductivity of particle clusters. Each method has its unique advantages and limitations, and the choice between them depends on the specific requirements of the battery application and the desired balance between performance enhancement and manufacturing complexity.

The engineering of the grain boundary is also achieved through the wet-coating approach. Mo et al. found that modifying the main particle surface with lithium boron oxide (Li_2O-$2B_2O_3$, LBO) can prevent the formation of microcracks and promote stable cycling of NCM811 [193]. It has been observed that wet-chemical coating, as opposed to dry coating, enables a thinner and more uniform layer of LBO to be applied to the main particle. Similarly, $Li(NiCoMn)_2O_4$ coated $LiNi_{0.91}Co_{0.06}Mn_{0.03}O_2$ cathode using the wet coating technique resulted in reduced crack formation, as depicted in Fig. 12**c** [194]. The coating material permeates secondary particles along the grain boundaries, enhancing structural stability before coating the primary particles. An in-situ XRD examination revealed that the redesigned cathode practically maintained its volume throughout cycling. The improved mechanical characteristics of the spinel coating layer were confirmed to play a substantial role in preserving the mechanical integrity of the layered structure during lithiation/delithiation through first-principles calculations. With an outstanding capacity retention of 93.44 % at 1C after 50 cycles, the coated cathode provides a specific capacity of 220.35 mAh g^{-1}. Fig. 12**d** and **e** shows the microstructural changes in $LiNi_{0.931}Co_{0.031}Mn_{0.029}$ $Al_{0.009}O_2$ (NMCA93) with Sb doping showing a very fine particle than the pristine NMCA93. The EDS mapping (Fig. 12**f**) shows that the F encapsulates the primary particle and covers the grain boundaries. the primary particles. The F 1 s, Sb $3d_{3/2}$, and O 1 s XPS spectra of as-synthesized NCMA93 and Sb-NCMA93, both with and without F coatings, are shown in Fig. 12**g**. The consumption of residual Li compounds on the surfaces of the F-coated cathode materials is responsible for the comparable peaks in the O 1 s XPS spectra of the uncoated cathode materials. The F-coated cathode materials exhibit stronger Sb–O peaks in their Sb $3d_{3/2}$ XPS spectra than the comparable peaks in the Sb $3d_{3/2}$ XPS spectra of the uncoated cathode materials. This phenomenon is probably caused by the decreased amount of residual Li compounds on their surfaces. The depth profiles in Fig. 12**h** demonstrate that the intensity of Ni^- species sputters for around 500 s before leveling off. The intensity of other inorganic species, like SbO^-, $LiCO_3^-$, LiF_2^-, and $LiSbO_2F^-$, decreases with increasing sputtering time, indicating that these species are concentrated within ~10 nm of the surfaces of secondary particles. In contrast, the intensity of NiF^- species reaches a maximum after approximately 300 s of sputtering. Grain boundary engineering can significantly enhance the performance of the modified cathode material by altering the surface of primary particles in a way that typical coating modifications cannot achieve. However, effective treatment of primary particle surfaces, whether through high-temperature treatment or pure wet treatment following surface coating at secondary particles, faces challenges such as accurate parameter control and poor repeatability. Although the alteration may be effectively accomplished in the lab, applying it in the industry poses challenges due to technical complexities and the need for expensive equipment. Future research should focus on progressing this technology toward industrialization.

3.4. Concentration gradient structure

After the core-shell structure had been thoroughly investigated to enhance the electrochemical performance of Ni-rich cathodes in comparison to conventional cathodes (CC), it was later discovered that this structure had drawbacks, including the ability for rapid structural and electrochemical performance degradation due to shell fracture and debonding between the core and shell upon cycling [195]. However, a unique structure called a concentration gradient was developed to solve the problems with core-shell cathode materials by preventing unfavorable volume fluctuations, preventing the development of microcracks, and further enhancing structural integrity. Typically, concentration-gradient structures fall into one of two categories: full concentration-gradient structures (FCGS) [196,197] or shell concentration-gradient structures (SCGS) [198,199]. The Ni-rich core and the outside shell with the TM concentration gradient make up SCGS cathodes [200]. The cathodes' discharge capacity is maximized by the Ni-enriched core, while improved stability is attained by the Mn/Co-enriched surface area. Since inactive Mn^{4+} is present close to the surface and protects the Ni-rich core by limiting side reactions between the electrolyte and $Ni^{3+/4+}$, SCGS cathodes often have the ability to withstand deterioration of the inner active materials. However, a SCGS $Li[Ni_{0.865}Co_{0.120}Al_{0.015}]O_2$ cathode with a Co-rich surface has been shown to have better thermal stability and cycling than a standard cathode. After charging to 4.3 V, the SCGS $Li[Ni_{0.865}Co_{0.120}Al_{0.015}]O_2$ cathode is devoid of microcracks whereas the traditional NCA cathode has several cracks. The cycling stability of SCGS cathodes is significantly increased by the gradual change in the TM concentration in the shell area, which leads to a reduction and weakening of radial stress at the core-shell interface [199]. In the outer region of the SCGS cathode, the primary particles exhibit radial elongation and are arranged perpendicular to the surface. These crystals are closely spaced and have parallel (003) plane arrangements, as shown in Fig. 13**a** [6]. To mitigate the stress induced by the H2-H3 phase transformation, the elongated columnar grains are enveloped by Ni-rich grains. This configuration in the SCGS cathode aims to provide a high specific discharge capacity during extended cycling, suppressing impedance increase and discharge capacity decay linked to the degradation of the interparticle boundary surface due to direct contact with the electrolyte. Sun's group [197] introduced the FCGS cathode, wherein the concentration gradient

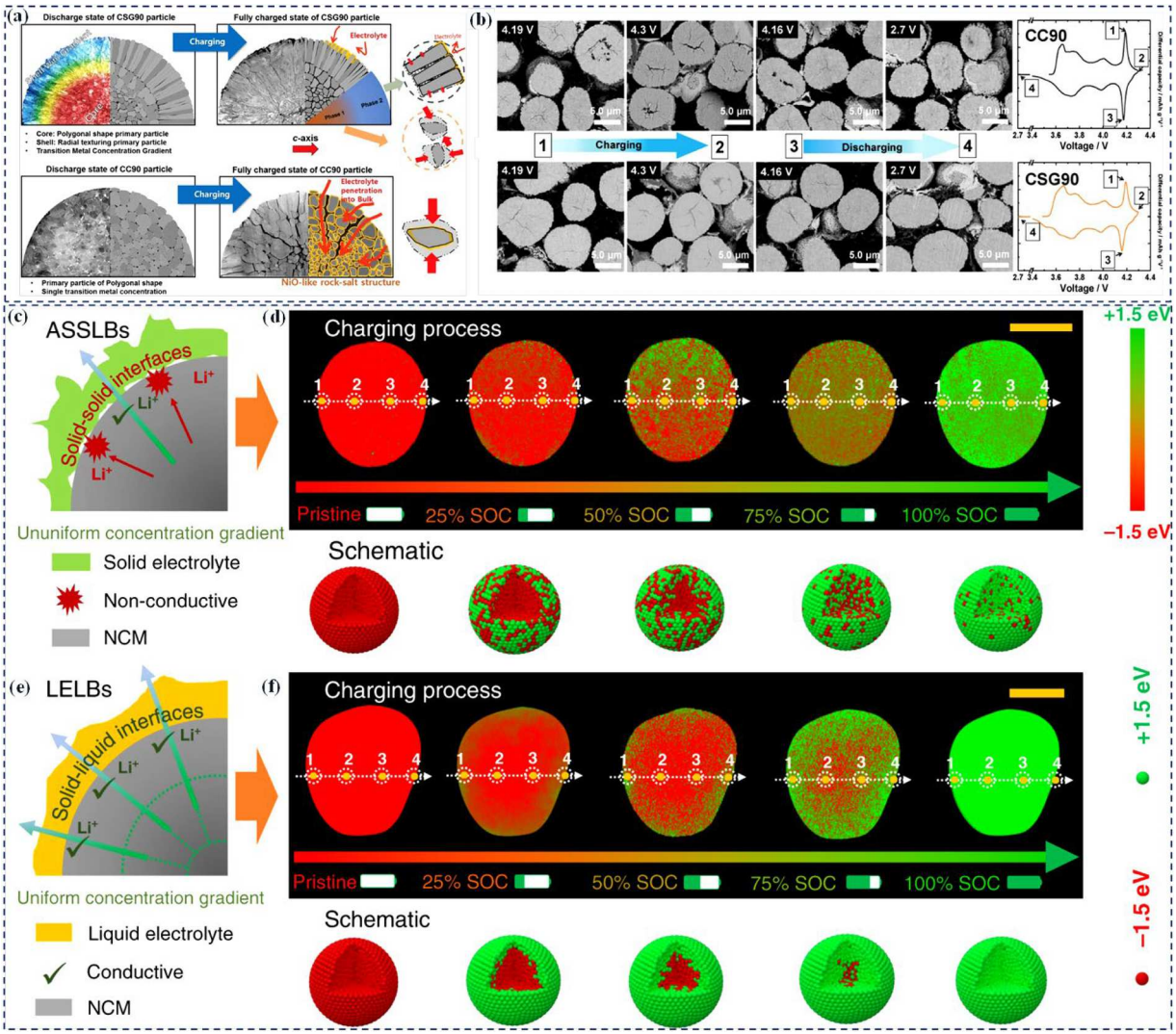

Fig. 13. **(a)** Internal morphology and mechanical integrity of CSG90 and CC90 cathodes at discharge and charge state, and **(b)** Cross-sectional SEM images of the charge state and discharge state for CC90 (up) and CSG90 (down). Reproduced with permission [203]. Copyright 2019, Wiley-VCH. **(c)** Solid-solid interface models and kinetics. **(d)** TXM-XANES mapping of single cathode particle as a function of charging time in ASSLBs, and the corresponding schematic diagram to expound the unique solid-state electrochemistry. **(e)** Schematic of solid-liquid interface models and kinetics. **(f)** TXM-XANES mapping of single cathode particle as a function of charging time in LELBs, and the corresponding schematic diagram expound the conventional solid-liquid electrochemistry (Scale bar, 10 μm). Reproduced with permission [202]. Copyright 2020, Nature.

extends uniformly throughout the entire particle. This modification addresses concerns about the structural stability of Ni-rich cathodes, especially under higher voltage cycling conditions and elevated temperatures (Fig. 13**b**). The FCGS cathode exhibits a gradual increase in Mn concentration from the center region towards the surface, accompanied by a nearly linear decline in Ni concentration. Operating in the 2.7–4.5 V voltage range, the FCGS cathode delivers an initial capacity of 215.4 mAh/g and maintains 88 % after 100 cycles. With a Co concentration gradient extending from the center region toward the surface area, Lee et al. [196] synthesized an FCGS cathode. After 2500 cycles of electrochemical cycling, only voids were observed in the secondary particles (Fig. 12f). However, microcracks emerged after 2500 cycles in the larger voltage window of 2.7–4.4 V at the elevated temperature of 55 °C. Two-sloped FCGS cathodes were developed through coprecipitation, featuring a slow, then steep, variation in Ni/Mn concentration approaching the particle surface to leverage the benefits of the unique FCGS structure and enhance stability further. Park et al. [201] presented a Ni-rich $Li[Ni_{0.8}Co_{0.06}Mn_{0.14}]$ O_2 cathode with a dual concentration gradient. After 100 cycles in a half-cell at increased voltages of 4.3 V at C/2, it maintained structural integrity, demonstrating cycling stability in preventing particle cracking. In another study, Lou et al. [202] expanded on the distinct electrochemistry of solid-state lithium batteries by drawing on ideas from the study of solid-solid interfaces and local ion diffusion in polycrystalline particles of NMC622 (Fig. 13**c-f**). This indicates discontinuous physical contact causes a slight difference in the initial electrochemical behavior of polycrystalline particles compared to that in conventional liquid-electrolyte LIBs. It also shows comparable electrochemical reversibility in a solid-state battery to that of a liquid-electrolyte battery. This result challenges the conventional wisdom that solid-state batteries perform less well electrochemically as a result of partial physical contact loss. Furthermore, the micrometer to single particle diameters of the local Li^+ transport channel was shown. The study reveals an unexpected homogeneity in the local Li concentration in a particle after first charging, which advances our knowledge of nonequilibrium electrochemical processes in solid-state electrochemistry.

3.5. Single-crystalline structure

The traditional shape of Ni-rich cathodes is characterized by spherical secondary particles aggregated with polycrystalline (PC) primary particles. The random aggregation of primary particles leads to strong grain boundary tension due to the anisotropy of Li-ion intercalation and deintercalation. As a result, the increased boundary stress accelerates electrolyte attack and contributes to the loss of electrical contact between primary particles. In recent years, there has been a growing focus on SC Ni-rich cathodes due to their potential for use in commercial applications [204–206]. Unlike PC cathodes, which consist of

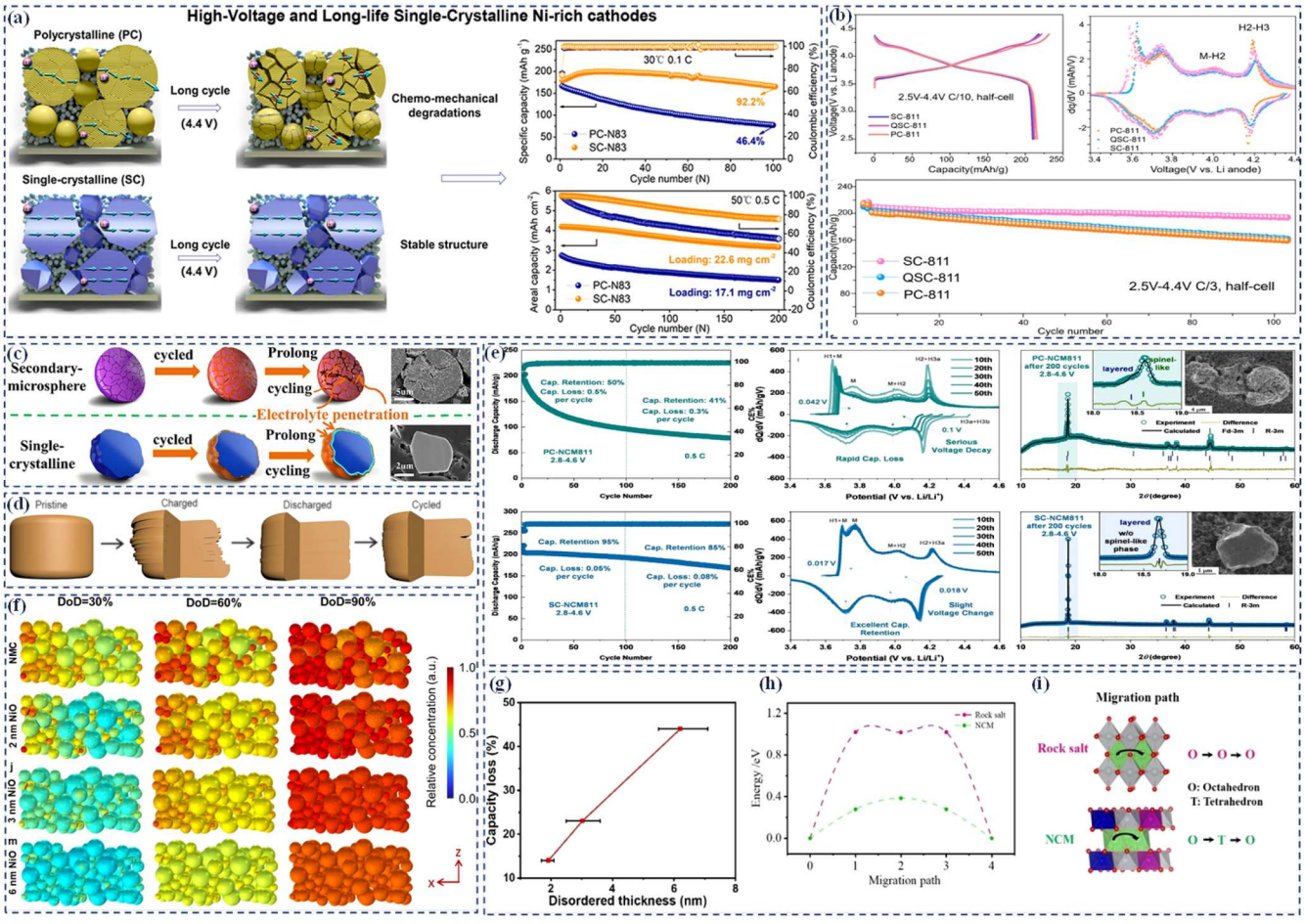

Fig. 14. **(a)** Comparison of the structural evolution and cycle performance of PC and SC cathode materials at 30 and 50 °C. Reproduced with permission [209]. Copyright 2021, Elsevier. **(b)** Electrochemical performance of the SC-811, QSC-811, and PC-811 cathode materials. Reproduced with permission [208]. Copyright 2022, Nature. **(c)** Degradation mechanism of PC and SC cathode. Reproduced with permission [206]. Copyright 2020, Elsevier. **(d)** Schematic illustration of the reversible planar gliding in SC Ni-rich cathode during cycling. Reproduced with permission [210]. Copyright 2020, Science. **(e)** Cycle performance, XRD patterns and SEM images of PC- and SC—NCM811 cathodes. Reproduced with permission [33]. Copyright 2022, Wiley-VCH. **(f)** Rock-salt layer thickness and the depth of discharge (DoD). **(g)** Capacity loss and rock-salt layer on the SC—NMC particles. **(h)** Static energy distribution along the migration path from DFT. **(i)** Li-ion diffusion pathways in ordered NCM and disordered NiO [211]. Copyright 2022, 2023 Wiley-VCH.

aggregated primary particles forming secondary particles, SC cathodes are characterized by smaller phase boundaries, a larger surface area, and more integrated crystal structures. PC cathodes are prone to secondary particle breakage during battery electrode flake production, leading to microcrack formation and propagation on the surface of secondary particles at high SOC. This exacerbates issues related to cathode-liquid interaction, resulting in rapid cell degradation and capacity loss. SC cathodes were proposed as a solution to address these challenges, offering increased stability during charging or discharging at higher cut-off voltages. According to Fig. 14**a**, the diffusion of Li ions during the charge-discharge process is slowed down by several grain boundaries inside PC secondary particles. Since, SC particles do not have grain boundaries, rapid ion transport can occur within them. SC cathodes have intact ion transport channels and a well-preserved structure during extended cycles at high voltages [207]. In contrast, substantial intergranular fractures and particle pulverization occur in PC cathodes, obstructing the diffusion paths for Li ions. In a previous study, Zhang et al. [208] provided a deep analysis of SC—NMC811, PC—NMC811 and quasi-SC—NMC811 (QSC-811) cathodes. Following two formation cycles, the charge/discharge profiles of various NMC811 types are displayed. According to the results in Fig. 14**b**, the discharge capacities of SC-811 and QSC-811 are 209.5 and 212.7 mA h/g, respectively, and they are similar to PC—NMC811′s value of 216.6 mA h/g. The first charge/discharge cycle's differential capacity (dQ/dV) curves demonstrate that SC-811 and QSC-811′s H2–H3 redox peak intensities are lower than PC-811′s. This finding suggests that, in comparison to PC-811, the harmful H2–H3 phase transition is somewhat inhibited in SC-811 and QSC-811. After 100 cycles, the capacity retentions of SC-811, QSC-811, and PC-811 are 92.6 %, 79.5 %, and 79.2 %, respectively. In comparison to QSC—NMC811 and PC-811, SC-811 has superior cycle retention, which is consistent with other studies on SC—NMC cathodes. Fig. 14**c** schematically shows that the SC structure can effectively reduce irreversible phase change, prevent intergranular fractures, and effectively attenuate undesirable electrode/electrolyte interactions.

Bi et al. [210] reported on studies on reversible slippage and cracking along the (003) plane in Ni-rich SC cathodes. When the material is charged, it is discovered that the (003) plane slip can be seen; however, when the material is discharged, the opposite happens. The sliding will ultimately develop into microcracks near the crystal surface, even if the internal lattice remains symmetrical after sliding (Fig. 14**d**), exposing additional surface to the liquid electrolyte. The local stress brought on by the concentration gradient of Li^+ in the lattice is connected to the reversible creation of microstructure defects. After the gradient in Li concentration has been formed in the lattice, the stress production of Li^+ radial diffusion along the particle is calculated using the analytical cylinder isotropic diffusion induced stress model. Peak tensile stress in the tangential and axial directions near the surface occurs at the start of lithium removal by charging, which causes microcracks to spread in the (003) plane. On the other hand, the center of the particle exhibits the maximal tensile stress in all directions. At a current density of 0.5 C, the cycle stabilities of PC- and SC—NCM811 were measured in the range of 2.8 to 4.6 V (vs. Li/Li^+) by Sun et al. [33] (Fig. 14**e**). The PC—NCM811 demonstrated a significant reduction in capacity after 100 and 200 cycles, respectively, resulting in a low retention rate of just 50 % and 41 %, respectively. By comparison, the SC cathode demonstrated exceptional cycle performance, with an average loss of just 0.05 % of capacity per cycle over the first 100cycles (10 % of the PC cathode) and an impressive 85 % (more than 170mAh g^{-1}) after 200cycles. In a previous work, Zhao et al. [211] deeply studied the relationship between cycle performance degradation mechanism in SC—NMC cathode through DFT and COMSOL Multiphysics modeling analysis. Fig. 14**f** displays the distribution of Li-ion concentrations on the surface of the SC—NMC particles. Once more, the concentration rose unmistakably as the discharge depths increased, just like in the single particle scenario. However, significantly decline for rock-salt surface layer thicknesses greater than 2 nm, suggesting that slow charge transfer has a negative impact on the dynamics of intercalation and eventually causes capacity degradation. The layered NMC phase has a higher effective energy barrier for Li-transport than the disordered rock-salt NiO layer (Fig. 14**g-i**). The detrimental impact of the rock-salt surface development on the kinetics of Li-transport was further verified using COMSOL Multiphysics simulation.

SC cathode materials hold great promise for practical use in commercially available LIBs due to their superior physical and electrochemical properties compared to PC cathode materials. However, SC cathodes face challenges related to the precise control of particle size and shape, limiting their commercialization and development. Factors in particle preparation, such as roasting temperature, holding period, and Li concentration, influence the characteristics of the final product. Recent research has focused on investigating the morphology and electrochemical capabilities of produced SC Ni-rich cathodes under various experimental conditions. These studies aim to enhance production procedures and approaches for SC materials. Ou et al. [212] have further improved the stability of SC $LiNi_{0.88}Co_{0.09}Mn_{0.03}O_2$ (SNCM) cathode by incorporating Al/Zr (Fig. 15**a** and **b**). The synergistic impact of Al/Zr co-doping in SNCM lattice improves Li-ion mobility, relieves internal strain, and suppresses Li/Ni cation mixing at a high cut-off voltage. During extended cell cycling, these characteristics enhance the cathode rate capability and structural stability. Specifically, the Zr-rich surface facilitates the establishment of a stable cathode electrolyte interphase, which inhibits Ni dissolution and keeps SNCM from reacting unintentionally with the non-aqueous fluorinated liquid electrolyte solution. In a recent study, Li et al. [213] introduced Ce/Gd dopants into SC Ni-rich $LiNi_{0.83}Co_{0.07}Mn_{0.10}O_2$ (SC—NCM@CG2) cathode materials, resulting in improved electrochemical performance and structural stability during high-voltage cycling (Fig. 15**c**). The incorporation of Ce and Gd induced distinct deposition behaviors, forming a high-entropy zone near the surface of SC—NCM@CG2. This zone, including a LCGO shell and a Ce/Gd dopant-concentrated layer, enhanced lattice oxygen stability, inhibited oxygen evolution, and prevented the formation of oxygen vacancies. Moreover, Ce/Gd incorporation facilitated reversible H2-H3 phase transformations and alleviated stress/strain during lithium-ion (de)intercalation processes (Fig. 15**d-e**). These synergistic effects reduced oxygen vacancy concentration, mitigated stress/strain, and inhibited in-plane migration of transition metal ions and lattice planar gliding, thereby preventing intragranular nanocrack formation.

In addition, high ionic conductivity surface coatings are thought to be a useful tactic for stabilizing the electrode/electrolyte contact for SC cathode [215]. The multifunctional layers of $LiBO_2/LiAlO_2$ (BA) on the surface of SC—NMC were depicted in Fig. 15**f** [90]. The middle layer of $LiAlO_2$ is intended to establish close contact with NMC in order to avoid direct contact between the cathode and electrolyte, therefore fortifying the cathode surface structure. BA coated NMC exhibits significantly better rate and cycle characteristics than B coated NMC and bare NMC at both 25 and 55 °C (Fig. 15**g**). Furthermore, Fan et al. [214] provided a method to build an in situ $Li_{1.4}Y_{0.4}Ti_{1.6}(PO_4)_3$ (LYTP) ion/electron conductive network that links SC—NMC particles (Fig. 15**h**). The LYTP network reduces mechanical instability, inhibits harmful crystalline phase change, and enables Li-ion transfer between SC—NMC particles. The LYTP-containing SC—NMC cathode combined with a Li metal anode for a coin cell delivered a capacity of 130 mAh g^{-1} after 500 cycles at 5 C rate in the 2.75–4.4 V range at 25 °C (Fig. 15**i**). Surface coating/modification for SC cathode offer superior performance in high-temperature, high-stress environments but come with challenges such as cost, brittleness, and complex manufacturing requirements. These factors must be carefully considered when selecting materials for specific engineering applications. However, a deep coating layer that is entirely homogeneous is difficult to obtain for SC cathode. Furthermore, the coating layer will break and lose some of its functionality due to the fluctuation in particle volume during repeated cycle procedures.

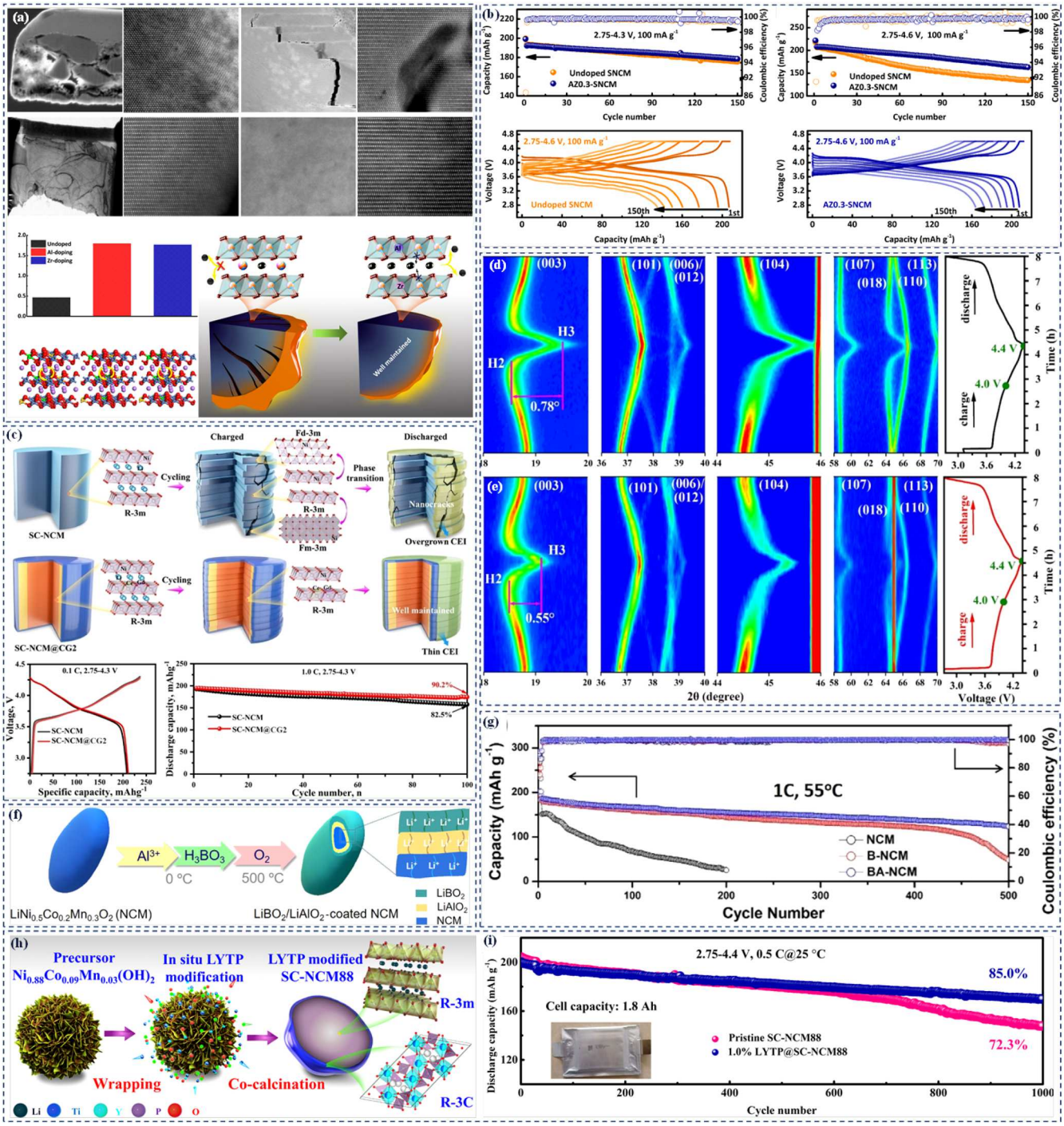

Fig. 15. **(a)** Morphology and crystal structure of undoped SNCM and AZ0.3-SNCM after 150 cycles. **(b)** Electrochemical characterizations of coin-type half-cell at 25 °C. Reproduced with permission [212]. Copyright 2022, Nature. **(c)** Schematic illustration of the structure evolutions for SC—NMC and SCNMC@CG2 during cycling and in situ XRD characterization for SC—NMC **(d)** and SC—NMC@CG2 **(e)** cathodes during 2nd cycle. Reproduced with permission [213]. Copyright 2024, Wiley-VCH. **(f)** BA coated SC—NMC dual modification process and **(g)** cyclability and coulombic efficiency. Reproduced with permission [90]. Copyright 2020, ACS. **(h)** LYTP@SC—NMC synthesis process and **(i)** electrochemical evaluation for pouch-type full cells. Reproduced with permission [214]. Copyright 2021, Nature.

Consequently, the coating modification can slow down the attenuation of materials to some level, but it is not a perfect solution. Consequently, it is recommended that in order to enhance the overall qualities of the applied SC materials, further modification procedures such doping be used in addition to reaching the highest level of coating uniformity.

3.6. Dual modification

It is important to keep in mind that sometimes implementing one modification strategy will not be able to solve all the issues; instead, it may focus on one issue while exacerbating others. For instance, many surface coating techniques stabilize the structure, but a significant amount of discharge capacity is lost due to the inactive coating layer. In addition, surface coatings cannot solve the cation mixing problem that

occurs inside the Ni-rich crystalline particles. Thus, numerous related explorations have been conducted, and several successes have been made, in an effort to use the synergetic effect among various strategies to improve the structure stability. The research conducted by Yang et al. introduced a one-step dual modification method to create an NMC811 cathode with a La_4NiLiO_8 coating and Ti doping (Fig. 16**a**) [216]. This approach aimed to leverage the synergistic effect of Ti doping and La_4NiLiO_8 coating for improved electrochemical performance. Ti doping was effective in inhibiting harmful phase changes, while the La_4NiLiO_8 coating layer enhanced the diffusion kinetics of Li ions. The combined impact of these modifications inhibited structural degradation and intergranular cracking, thereby stabilizing the host material's structure and enhancing overall cell performance (Fig. 16**b**). In another research by Yoon et al. [217] Co_xB was utilized to coat the NMC811 secondary particle's surface and introduce grain boundaries between the NMC811 primary particles. This coating and infusion approach, along with the optimized structure, demonstrated improved stability in the NMC811 cathode, with minimal microcrack formation after 200 cycles. This suggests that the electrolyte did not significantly damage the interior of secondary particles, showcasing the enhanced structural stability achieved through these modifications (Fig. 16**c**) [217]. Tang et al. [218] explored the use of elemental doping coupled with surface coating (Fig. 16**d**). Additionally, Lim et al. [219] created a two-step full concentration gradient (TSFCG-Al) Al-doped $Li[Ni_{0.84}Co_{0.06}Mn_{0.09}Al_{0.01}]O_2$ (NCMA) cathode material, as seen in Fig. 16**e**. The particles have a distinctive morphology with rod-shaped and radially arranged primary particles as a result of the concentration gradient. Even at a high cutoff voltage of 4.5 V, TSFCG-Al demonstrated a greater discharge capacity and improved structural stability when compared to commercial NCA85. After 100 cycles, the structural examination of raw NCA cathodes and TSFCG-Al cathodes revealed that TSFCG-Al retains structural integrity, while NCA particles experience significant breaking as a result of the buildup of stress and strain at the grain boundary. According to reports, quaternary NCMA cathodes with a hybrid structure may effectively stop fractures from spreading toward the surface of secondary particles, extending the lifespan of batteries [220]. The combination of doping with concentration gradient structures has shown the potential to further enhance performance. In the case of Al-doped full concentration gradient $Li[Ni_{0.61}Co_{0.12}Mn_{0.27}]O_2$ (Al-FCG61), it was reported that even after 3000 cycles at 100 % DOD and 1.0C cycling, the cathode material retained 84 % of its original capacity. In comparison, the full concentration gradient (FCG61) without Al-doping did not reach 80 % of its original capacity until after 500 cycles. Mechanical strength data indicated that Al-doping strengthened the grain boundaries of secondary particles, contributing to delaying the initiation of microcracks [221]. Park et al. [222] created the shell concentration-gradient $Li[Ni_{0.90}Co_{0.045}Mn_{0.045}Al_{0.01}]O_2$ cathode (CSG-NCMA90). The primary particles of CSG-NCM90 exhibited finer and longer characteristics in the radial direction compared to those of NMC90, NCMA90, and CSG-NCM90 (Fig. 16**f**). TEM analysis revealed that these primary particles had

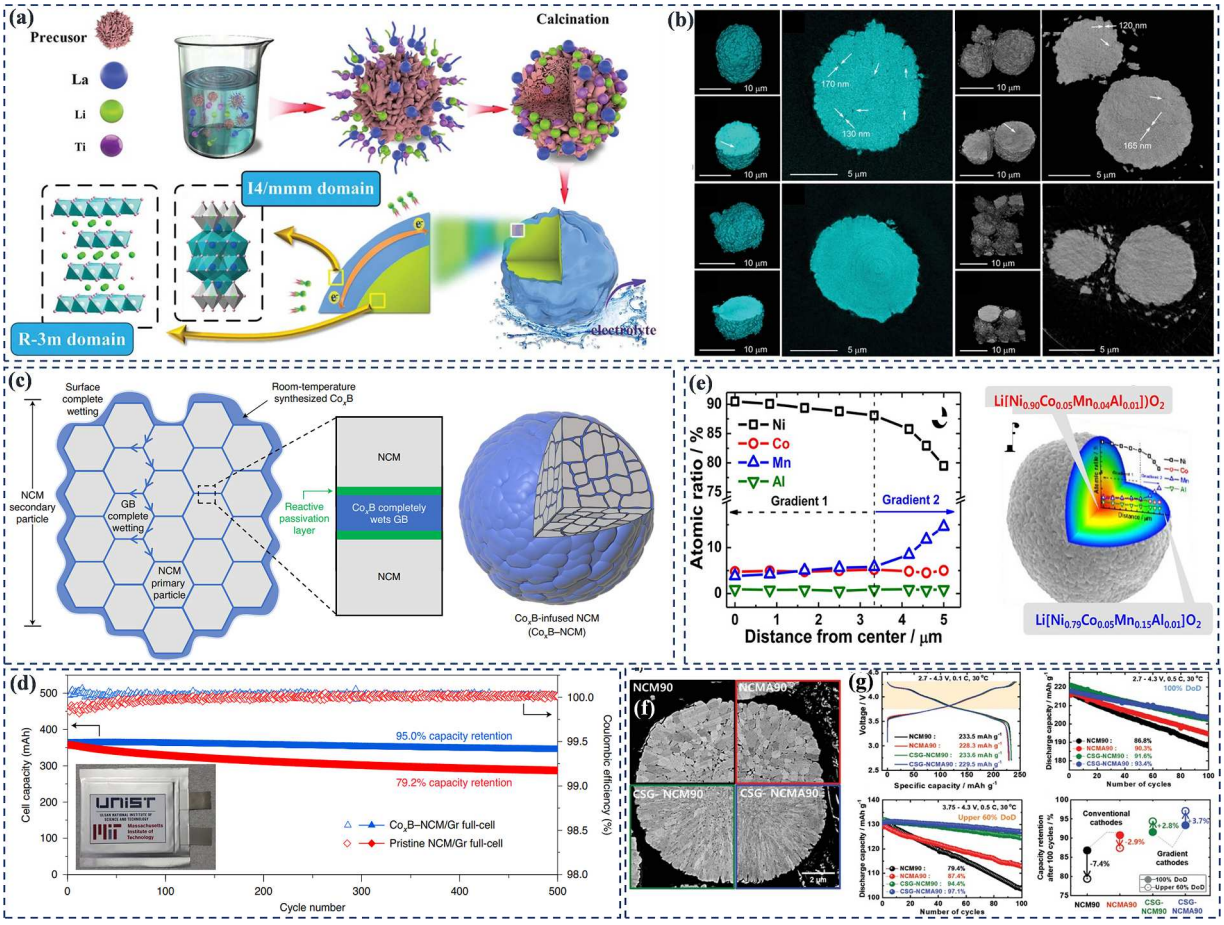

Fig. 16. **(a)** Schematic representation of synthesize process of Ti-doped and La_4NiLiO_8-coated NCM811 cathode material. **(b)** 3D reconstruction of single NCM particle (slice view and enlarged view of showing multiple cracks), and 3D morphology of NCM, and 3D morphology of LT1 particle after cycling. Reproduced with permission [216]. Copyright 2019, Wiley-VCH. **(c, d)** Schematic illustration of Co_xB coating-plus-infusion microstructure and cycle performance of NCM811 cathode particle. Reproduced with permission [217]. Copyright 2021, Nature. **(e)** EPMA scan of the atomic ratio of TM of the lithiated TSFCG-Al powder, and schematic diagram of the secondary particle of NCMA cathode. Reproduced with permission [219]. Copyright 2016, ACS. **(f, g)** Cross-sectional SEM images and electrochemical performance of the NCM90, NCMA90, CSG-NCM90, and CSG-NCMA90 cathode particles. Reproduced with permission [222]. Copyright 2021, Wiley-VCH.

(001) facets on their lateral sides, providing resistance to electrolyte attack and surface failure. This unique structure was effective in preventing the formation and spreading of microcracks during continuous cycling in highly delithiated states (Fig. 16**g**).

An oxalate-assisted deposition and subsequent thermally driven diffusion approach were used to develop and manufacture a $LiNi_{0.9}Co_{0.1}O_2$ (NC91) cathode that is synchronous gradient Al-doped and $LiAlO_2$-coated [34]. Al-oxalate chelates are created when the oxalate anions first chelate with Al^{3+} in solution, as seen in Fig. 17**a**. The resulting chelates attach themselves to the exposed surfaces of the hydroxide precursor by hydrogen bond interaction, penetrating along intergranular gaps. The Al^{3+} in the Al-oxalate chelate will be stimulated to nucleate and develop in a regulated manner to produce an $Al(OH)_3$ coating layer on the surface (NC91-$Al(OH)_3$) upon OH^- injection. Early on in the charging process, the predicted lattice parameters and unit cell volumes from the in situ XRD refinements were identical (Fig. 17**b**). Fig. 17**c** and 17**d** show a plot of the charging state function. Fig. 17**e** displays the distributions of internal stresses and volume deformation inside the secondary particles at 4.3 V. Finite-element modeling, in situ X-ray diffraction data, and theoretical calculations all confirm that Al^{3+} arrives at the tetrahedral interstices before Ni^{2+}, which removes the internal structural stress and Li/Ni disorder. Side reactions are decreased and electrolyte penetration of the boundaries is prevented by the Li^+-conductive $LiAlO_2$ skin. After charging to 4.3 V, the original rhombohedral structures (space group of R-3 m) were preserved, as seen in Fig. 17**f**. The coalescence of peaks $(108)_R$ and $(110)_R$ into a single spinel $(440)_S$ peak indicates that the NCAl-LAO underwent a transformation to a disordered spinel structure (space group of Fd-3 m) at around 200 °C as a result of temperature rise.

The NC91 exhibited a distinct exothermic peak at 192.4 °C, as indicated by the DSC measurements (Fig. 17**g**), with a total heat emitted of 632 J g^{-1}. By contrast, the NCAl-LAO demonstrated enhanced thermal stability with a lower total released heat of 413 J g^{-1} and a greater exothermic peak temperature of 222.7 °C. In contrast to the single modification technique discussed above, dual modification often necessitates a laborious preparation process and increased energy consumption, making it difficult for the strategy to find industrial use at the moment. However, given its significant improvement in cathode cycle stability and electrochemical performance, it may be used to make battery materials in the future. Therefore, it is crucial for future studies

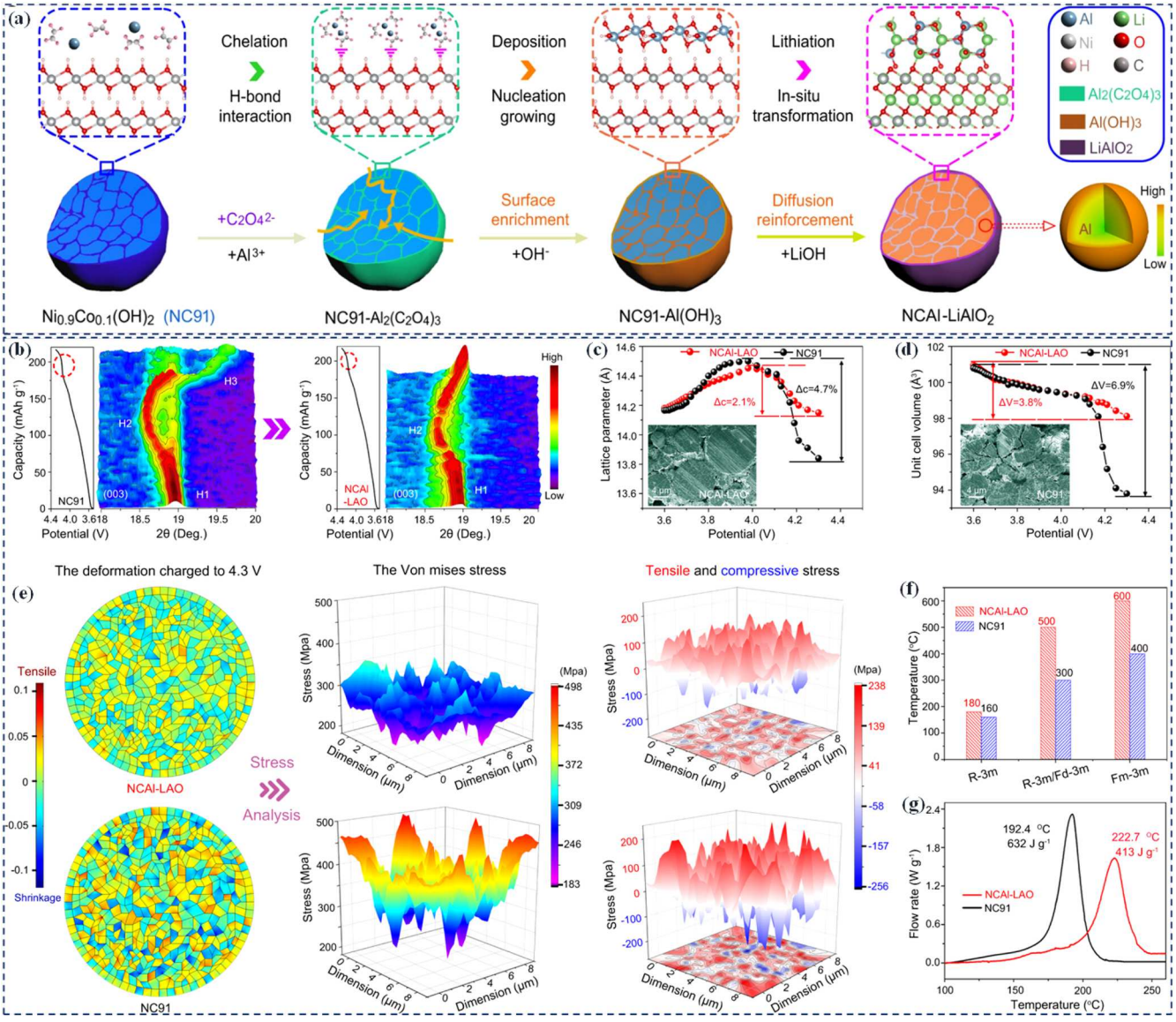

Fig. 17. **(a)** Schematic illustration of synchronous gradient Al-doped and $LiAlO_2$-coated NC91 cathode. **(b-g)** Crystal structure, internal stress, and thermal stability of Ni-rich cathode. Reproduced with permission [34]. Copyright 2021, Nature.

to optimize the preparation route.

3.7. CEI engineering and electrolyte additives

CEI engineering involves strategies to stabilize the interface, thereby enhancing the battery's overall performance. Applying thin layers of protective materials (e.g., oxides, phosphates, or polymers) on the cathode particles can prevent direct contact between the electrolyte and the Ni-rich cathode material. This barrier can inhibit harmful side reactions, reduce the dissolution of transition metals, and stabilize the CEI, improving cycle life and thermal stability. The incorporating functional additives (EC, DMC, DEC, FEC, VC, EMC, etc.) into the electrolyte can also lead to the formation of a stable and uniform CEI layer. These additives react with the cathode surface to form a film that protects the cathode material from direct interaction with the electrolyte, minimizing capacity fade and improving resistance to thermal runaway. The sustained electrochemical performance of Ni-rich cathodes in $LiPF_6$-based electrolytes has been thought to be maintained by the application of additives to create a consistent CEI and to scavenge there active HF and PF_5 species (Fig. 18**a**) [223]. Such electrolytes generate dangerous interfacial damage to Ni-rich cathodes in LIBs as well as TM dissolution from the cathode due to the HF and PF_5 species they create (Fig. 18**b**). A homogenous CEI is formed when film-forming additives oxidize on the surface of Ni-rich cathodes before electrolyte solvents such EC, DMC, and Li salt break down. Uniform CEI can prevent interfacial deterioration caused by microcracks inside NMC secondary particles and reversible phase change of Ni-rich cathodes, as well as side reactions of the electrolyte at the cathode. In a previous report by Sahni et al. [187], Li_3PO_4 coating is shown to be successful for NMC cathode in improving the specific capacity of the initial discharge as well as the rate capability and capacity retention in the following charge/discharge cycles. According to their findings, there are two ways to increase the first discharge capacity, one is to stop the surface reduced layer from forming during soaking, and another is to stop the NMC surface region's phase change from layered structure to disordered spinel structure during the first charge process. Besides, by improving Li-ion transport, which permits more Li-ion intercalation and de-intercalation at the electrode/electrolyte interface during charge and discharge, respectively, there

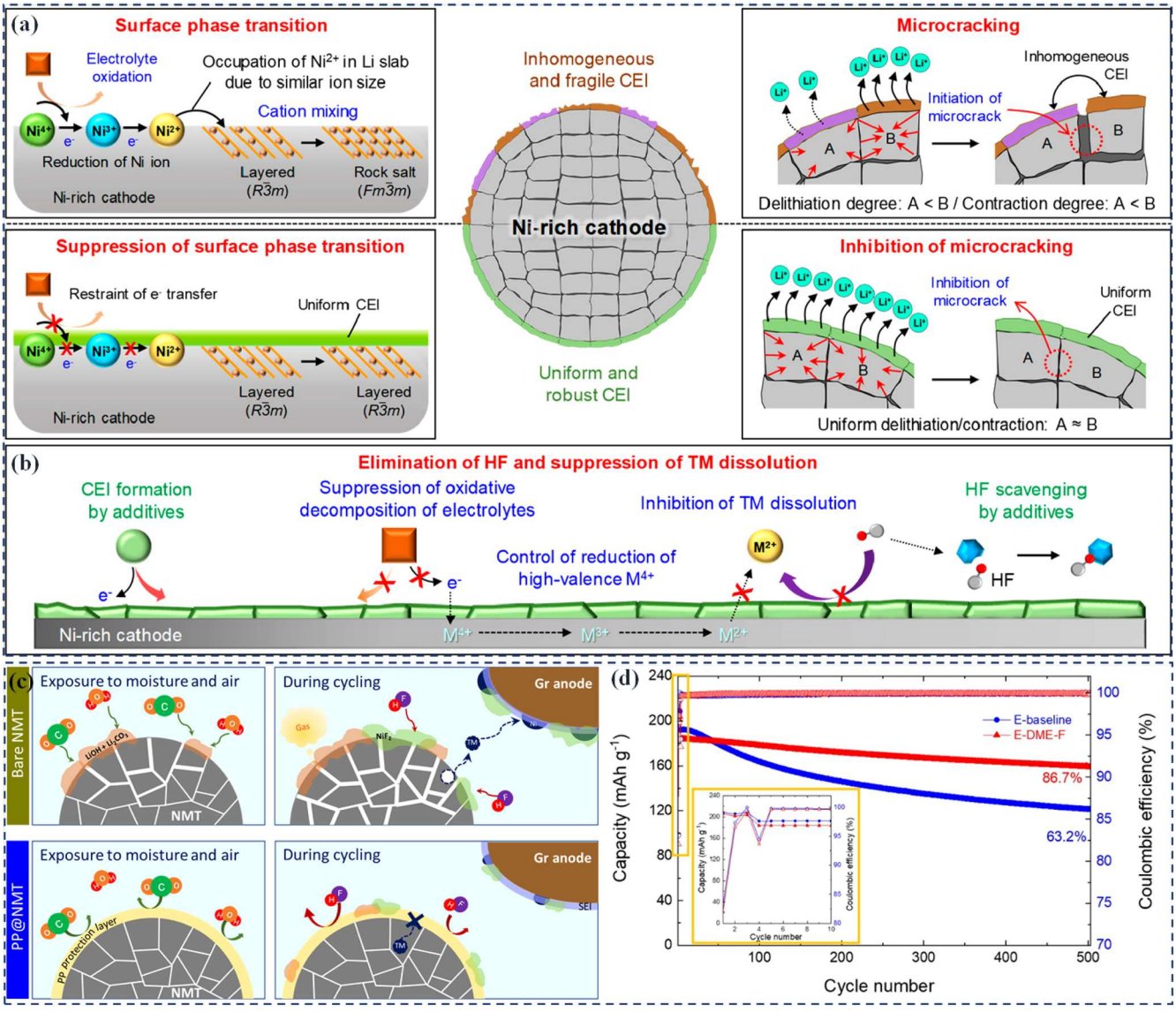

Fig. 18. **(a)** Surface phase transition, microcracking and suppression of surface phase transition along with inhibition of microcracking simultaneously. **(b)** Elimination of HF and suppression of TM dissolution. Reproduced with permission [223]. Copyright 2020, ACS. **(c)** Schematic illustration of the advantages of the dual-protection PP-coating layer on NMT, **(d)** cycling performances of PP@NMT using E-baseline and E-DME-F. Reproduced with permission [224]. Copyright 2022, ACS.

is a second way to increase the initial discharge capacity [188]. Although, Co-free Ni-rich cathode materials are thought to be among the most promising cathode because of their high specific capacity, their highly reactive surface still makes practical use difficult. It is shown (Fig. 18**c**) that the $LiNi_{0.96}Mg_{0.02}Ti_{0.02}O_2$ (NMT) cathode material is protected against surface contamination from wet air and from undesirable interfacial side reactions during cycling by a coating layer of polyimide/polyvinyl pyrrolidone (PI/PP) [224]. Furthermore, with an innovative localized high-concentration electrolyte, the exposed PP@NMT achieves a high-capacity retention of 86.7 % after 500 cycles (Fig. 18**d**). This work shows that even after being exposed to damp air, Co-free/Ni-rich multilayer cathodes may be effectively protected. In another study, a multifunctional, self-reconstructive CEI layer with altered mechanical and electrochemical stability was created on a Co-free Ni-rich cathode surface [225]. Concurrently, the protective layer against fluoride caused by additives was created in order to work together to control the flow of electrons and lithium ions during the CEI restoration process. Through the processes of O_2 elimination, anion regulation, water capture, and gas adsorption, the additive-induced self-reconstructive CEI layer reduced hazardous oxygen species, controlled electrolyte dynamics, relieved lithium salt hydrolysis, and prevented electrolyte decomposition [226,227].

4. Conclusion and future perspectives

In this review, we have explored the intricate world of Ni-rich cathode materials, shedding light on their electrochemical dynamics and the innovative modification strategies aimed at mitigating structural and interfacial degradation. Through a detailed analysis of voltage fade, capacity decay, and structural instability, it becomes evident that while Ni-rich cathodes offer high energy density, their practical implementation faces formidable challenges. The understanding of these challenges has led to the development of ingenious modification strategies, such as surface coatings, doping techniques, and nanostructuring approaches with controlled environment handling and advanced manufacturing techniques, which have shown promise in enhancing the stability and durability of these cathode materials (Fig. 19). As we move forward, several avenues for future research and development emerge:

Multi-Pronged Strategies: Given the problems faced by Ni-rich cathodes come from multiple sources, it is imperative to address them simultaneously via a combination of synergistic approaches in order to achieve long-term cycle stability. In particular, synergies among cation/anion co-doping, Li site/transition metal site co-doping, single crystals and coatings have great potentials to yield significant improvement in the cycle stability of Ni-rich cathodes because they improve the cycle stability via different mechanisms. The synergistic effects are possible because the capacity decay over cycles will accelerate when a group of Ni-rich particles in the cathode cease to contribute to redox reactions by any mechanism(s), the next group of Ni-rich particles will be overcharged, leading to vicious cycles. In contrast, by suppressing every source of capacity decay mechanisms, a long-lasting cycle life becomes possible.

Co-Free Ni-Rich Cathodes: Co element is expensive because its global reserves are low in comparison to other elements in Ni-rich cathodes. As such, research on Co-free cathodes is critical for widespread adoption of electric vehicles. Co is known to play a critical role in offering high rate capability and suppressing cation (Li/Ni) mixing. Thus, to achieve Co-free Ni-rich cathodes with good cycle stability, focus should be co-doping and tri-doping as well as simultaneous Li site/

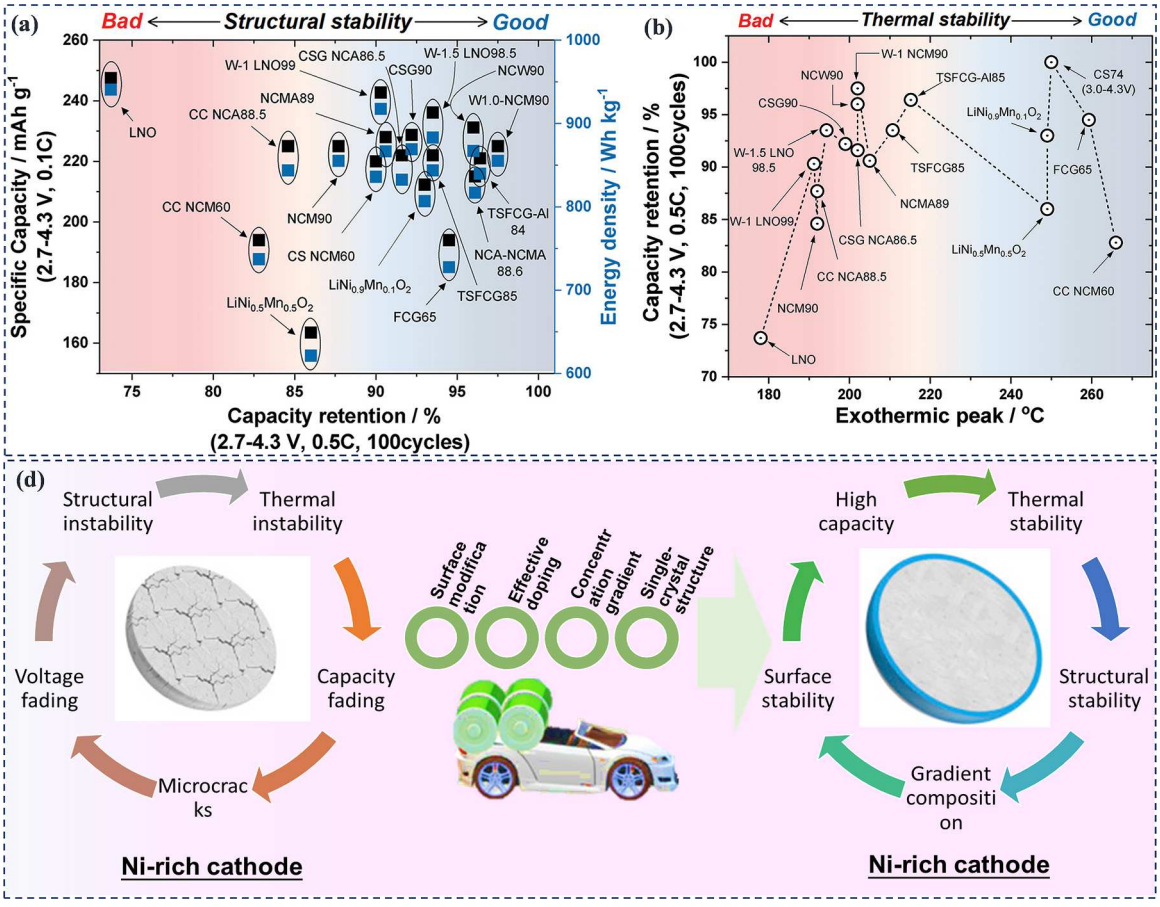

Fig. 19. (a, b) Comparison of the structural and thermal stability for various Ni-rich cathode materials. Reproduced with permission [5]. Copyright 2020, Wiley-VCH. **(c)** Schematic illustration of the next-generation techniques to mitigate the existing problems.

transition metal site doping to suppress cation mixing and postpone phase transformation to higher cutoff voltages during charge. Computational screening of the functions of various dopant elements can accelerate the progress in identifying suitable dopants for Co-free Ni-rich cathode materials.

CEI engineering: CEI engineering in Ni-rich cathodes is a multifaceted approach that addresses the inherent challenges of these materials. Through innovative surface treatments, electrolyte formulations, material doping, and composition modifications, researchers have the opportunity to unlock the full potential of Ni-rich cathodes for high-performance LIBs.

Advanced Characterization Techniques: Continued advancement of in situ and operando characterization techniques is paramount. These techniques offer real-time insights into electrochemical processes occurring at atomic and molecular levels, providing a deeper understanding of degradation mechanisms. By closely monitoring changes as they happen during battery operation, researchers can identify key factors contributing to performance decline and degradation. Such understanding enables the development of more targeted modification strategies aimed at mitigating degradation pathways, enhancing stability, and extending battery lifespan. Consequently, the evolution of these characterization techniques plays a pivotal role in accelerating the advancement of Ni-rich cathodes and facilitating the development of next-generation high-performance LIBs.

Modeling and Simulation: First-principles simulations and multi-scale modeling can aid in the rapid screening of material candidates and enhance the understanding of complex degradation mechanisms at the cell level. These modeling and simulations can predict the behavior of new materials under various conditions, guiding experimental efforts toward the most promising options.

AI-Accelerated Materials Discovery: Recent advancements in artificial intelligence (such as deep learning, active learning, reinforcement learning, and ensemble learning) have made acceleration of new material discovery possible. Developing and utilizing AI algorithms to explore novel materials, including alternative Li-ion conductors and solid-state electrolytes, can accelerate material discovery and revolutionize the design of Ni-rich cathode materials. Investigating new chemistries and composite structures might unveil materials with enhanced stability and performance.

Multi-Disciplinary Collaboration: Collaborations between materials scientists, electrochemists, physicists, engineers and computer scientists are essential. Interdisciplinary efforts can provide holistic solutions by combining insights from various fields, leading to innovative approaches in both material design and battery engineering.

Sustainability and Recycling: As the demand for LIBs grows, ensuring the sustainability of materials and developing efficient recycling methods becomes imperative. Research into eco-friendly materials and closed-loop recycling systems will be pivotal in reducing the environmental impact of battery technology.

In summary, by combining fundamental insights into electrochemical dynamics with innovative modification strategies, there is immense potential to revolutionize the landscape of Ni-rich cathode materials. By effectively addressing the challenges associated with these materials, we can pave the way for the development of more reliable, efficient, and sustainable LIBs. This integration of advanced understanding and strategic enhancement holds the promise of ushering in a new era in energy storage technology, where LIBs play a central role in enabling a cleaner and more sustainable energy future.

CRediT authorship contribution statement

Adil Saleem: Writing – review & editing, Writing – original draft, Investigation, Formal analysis, Data curation, Conceptualization. **Leon L. Shaw:** . **Rashid Iqbal:** Writing – original draft, Methodology, Formal analysis, Data curation, Conceptualization. **Arshad Hussain:** Methodology, Investigation, Data curation, Conceptualization. **Abdul Rehman Akbar:** Methodology, Formal analysis, Data curation. **Bushra Jabar:** Formal analysis, Data curation. **Sajid Rauf:** Methodology, Formal analysis, Data curation. **Muhammad Kashif Majeed:** Writing – original draft, Data curation, Conceptualization.

Declaration of competing interest

The authors declare the following financial interests/personal relationships which may be considered as potential competing interests: Leon Shaw reports financial support was provided by National Science Foundation. Leon Shaw reports a relationship with National Science Foundation that includes: funding grants. Leon Shaw has patent pending to None. None. If there are other authors, they declare that they have no known competing financial interests or personal relationships that could have appeared to influence the work reported in this paper.

Acknowledgements

This work was financially supported by the U.S. National Science Foundation (NSF) with the award numbers OISE-2230770. Leon Shaw is also grateful to the Rowe Family Endowment Fund.

References

[1] J.W. Choi, D. Aurbach, Nat. Rev. Mater. 1 (2016) 16013.
[2] E.C. Evarts, Nature 526 (2015) S93–S95.
[3] D. Hou, Z. Xu, Z. Yang, C. Kuai, Z. Du, C.-J. Sun, Y. Ren, J. Liu, X. Xiao, F. Lin, Nat. Commun. 13 (2022) 3437.
[4] G.E. Blomgren, J. Electrochem. Soc. 164 (2016) A5019.
[5] J.U. Choi, N. Voronina, Y.-K. Sun, S.-T. Myung, Adv. Energy Mater. 10 (2020) 2002027.
[6] H.H. Sun, H.-H. Ryu, U.-H. Kim, J.A. Weeks, A. Heller, Y.-K. Sun, C.B. Mullins, ACS. Energy Lett. 5 (2020) 1136–1146.
[7] G.W. Nam, N.-Y. Park, K.-J. Park, J. Yang, J. Liu, C.S. Yoon, Y.-K. Sun, ACS. Energy Lett. 4 (2019) 2995–3001.
[8] J.M. Tarascon, M. Armand, Nature 414 (2001) 359–367.
[9] J. Kim, H. Lee, H. Cha, M. Yoon, M. Park, J. Cho, Adv. Energy Mater. 8 (2018) 1870023.
[10] S. Myung, F. Maglia, K. Park, C. Yoon, P. Lamp, S. Kim, Y. Sun, A.E. Lett, Energy Mater. 6 (2016) 1501010.
[11] W. Li, E.M. Erickson, A. Manthiram, Nat. Energy 5 (2020) 26–34.
[12] M. Jiang, D.L. Danilov, R.-A. Eichel, P.H.L. Notten, Adv. Energy Mater. 11 (2021) 2103005.
[13] L. de Biasi, B. Schwarz, T. Brezesinski, P. Hartmann, J. Janek, H. Ehrenberg, Adv. Mater. 31 (2019) 1900985.
[14] A. Manthiram, B. Song, W. Li, Energy Storage Mater. 6 (2017) 125–139.
[15] A.-H. Marincaş, F. Goga, S.-A. Dorneanu, P. Ilea, J. Solid State Electrochem. 24 (2020) 473–497.
[16] Y. Xue, L.-L. Zheng, Z.-B. Wang, Y. Han, F.-D. Yu, Y.-X. Zhou, J. Nanoparticle Research 20 (2018) 257.
[17] J.-H. Park, J.-S. Kim, E.-G. Shim, K.-W. Park, Y.T. Hong, Y.-S. Lee, S.-Y. Lee, Electrochem. commun. 12 (2010) 1099–1102.
[18] C. Xu, K. Märker, J. Lee, A. Mahadevegowda, P.J. Reeves, S.J. Day, M.F. Groh, S. P. Emge, C. Ducati, B.Layla Mehdi, Nat. Mater. 20 (2021) 84–92.
[19] J.U. Choi, N. Voronina, Y.K. Sun, S.T. Myung, Adv. Energy Mater. 10 (2020) 2002027.
[20] Y. Lee, J. Lee, K.Y. Lee, J. Mun, J.K. Lee, W. Choi, J. Pow. Sour. 315 (2016) 284–293.
[21] J.-L. Shi, J.-N. Zhang, M. He, X.-D. Zhang, Y.-X. Yin, H. Li, Y.-G. Guo, L. Gu, L.-J. Wan, ACS. Appl. Mater. Interfaces 8 (2016) 20138–20146.
[22] F. Schipper, E.M. Erickson, C. Erk, J.-Y. Shin, F.F. Chesneau, D. Aurbach, J. Electrochem. Soc. 164 (2016) A6220.
[23] S. Cui, Y. Wei, T. Liu, W. Deng, Z. Hu, Y. Su, H. Li, M. Li, H. Guo, Y. Duan, Adv. Energy Mater. 6 (2016) 1501309.
[24] H.-H. Ryu, K.-J. Park, C.S. Yoon, Y.-K. Sun, Chem. Mater. 30 (2018) 1155–1163.
[25] H. Liu, M. Wolfman, K. Karki, Y.-S. Yu, E.A. Stach, J. Cabana, K.W. Chapman, P. J. Chupas, Nano Lett. 17 (2017) 3452–3457.
[26] Q. Huang, X. Zhang, F. Wu, R. Chen, L. Li, Energy Storage Mater. 63 (2023) 103050.
[27] C. Liao, F. Li, J. Liu, Nanomaterials 12 (2022) 1888.
[28] L. Liang, W. Zhang, F. Zhao, D.K. Denis, F. Zaman, L. Hou, C. Yuan, Adv. Mater. Interfaces 7 (2020) 1901749.
[29] R. Jung, R. Morasch, P. Karayaylali, K. Phillips, F. Maglia, C. Stinner, Y. Shao-Horn, H.A. Gasteige, J. Electrochem. Soc. 165 (2018) A132–A141.
[30] Y. Su, G. Chen, L. Chen, Q. Li, Y. Lu, L. Bao, N. Li, S. Chen, F. Wu, Chin. J. Chem. 38 (2020) 1817–1831.
[31] A. Butt, G. Ali, K. Tul Kubra, R. Sharif, A. Salman, M. Bashir, S. Jamil, Energy Technol. 10 (2022) 2100775.

[32] J. Shen, B. Zhang, W. Huang, X. Li, Z. Xiao, J. Wang, T. Zhou, J. Wen, T. Liu, K. Amine, X. Ou, Adv. Funct. Mater. 33 (2023) 2300081.
[33] J. Sun, X. Cao, H. Yang, P. He, M.A. Dato, J. Cabana, H. Zhou, Angewandte Chemie Int. Ed. 61 (2022) e202207225.
[34] H. Yu, Y. Cao, L. Chen, Y. Hu, X. Duan, S. Dai, C. Li, H. Jiang, Nat. Commun. 12 (2021) 4564.
[35] D. Andre, S.-J. Kim, P. Lamp, S.F. Lux, F. Maglia, O. Paschos, B. Stiaszny, J. Mater. Chem. A 3 (2015) 6709–6732.
[36] S.-T. Myung, F. Maglia, K.-J. Park, C.S. Yoon, P. Lamp, S.-J. Kim, Y.-K. Sun, ACS. Energy Lett. 2 (2017) 196–223.
[37] V. Etacheri, R. Marom, R. Elazari, G. Salitra, D. Aurbach, Energy Environ. Sci. 4 (2011) 3243–3262.
[38] C. Ding, Y. Bai, X. Feng, C. Chen, Solid. State Ion. 189 (2011) 69–73.
[39] D. Aurbach, O. Srur-Lavi, C. Ghanty, M. Dixit, O. Haik, M. Talianker, Y. Grinblat, N. Leifer, R. Lavi, D.T. Major, J. Electrochem. Soc. 162 (2015) A1014.
[40] S. Tan, L. Wang, L. Bian, J. Xu, W. Ren, P. Hu, A. Chang, J. Pow. Sour. 277 (2015) 139–146.
[41] Y. Chen, Y. Zhang, B. Chen, Z. Wang, C. Lu, J. Pow. Sour. 256 (2014) 20–27.
[42] M. Bettge, Y. Li, B. Sankaran, N.D. Rago, T. Spila, R.T. Haasch, I. Petrov, D. P. Abraham, J. Pow. Sour. 233 (2013) 346–357.
[43] C. Liang, F. Kong, R.C. Longo, C. Zhang, Y. Nie, Y. Zheng, K. Cho, J. Mater. Chem. A 5 (2017) 25303–25313.
[44] H. Sun, H. Ryu, U. Kim, J. Weeks, A. Heller, Y. Sun, C. Mullins, in, 2020.
[45] X. Ding, Y.-X. Li, X.-D. He, J.-Y. Liao, Q. Hu, F. Chen, X.-Q. Zhang, Y. Zhao, C.-H. Chen, ACS. Appl. Mater. Interfaces 11 (2019) 31477–31483.
[46] E. Boivin, N. Guerrini, R.A. House, J.G. Lozano, L. Jin, G.J. Rees, J.W. Somerville, C. Kuss, M.R. Roberts, P.G. Bruce, Adv. Funct. Mater. 31 (2021) 2003660.
[47] M. Jo, M. Noh, P. Oh, Y. Kim, J. Cho, Adv. Energy Mater. 4 (2014) 1301583.
[48] J. Choi, S.Y. Lee, S. Yoon, K.H. Kim, M. Kim, S.H. Hong, ChemSusChem. 12 (2019) 2439–2446.
[49] Y.-K. Lin, C.-H. Lu, J. Pow. Sour. 189 (2009) 353–358.
[50] M. Zhang, H. Zhao, M. Tan, J. Liu, Y. Hu, S. Liu, X. Shu, H. Li, Q. Ran, J. Cai, J. Alloys. Compd. 774 (2019) 82–92.
[51] Z. Gong, Y. Yang, Energy Environ. Sci. 4 (2011) 3223–3242.
[52] Y. Ding, D. Mu, B. Wu, Z. Zhao, R. Wang, Ceram. Int. 46 (2020) 9436–9445.
[53] H.-H. Sun, W. Choi, J.K. Lee, I.-H. Oh, H.-G. Jung, J. Pow. Sour. 275 (2015) 877–883.
[54] P. Pang, X. Tan, Z. Wang, Z. Cai, J. Nan, Z. Xing, H. Li, Electrochim. Acta 365 (2021) 137380.
[55] Y. Lee, H. Kim, T. Yim, K.-Y. Lee, W. Choi, J. Power. Sources. 400 (2018) 87–95.
[56] S.-J. Yoon, K.-J. Park, B.-B. Lim, C.S. Yoon, Y.-K. Sun, J. Electrochem. Soc. 162 (2014) A3059.
[57] H.-J. Noh, S.-T. Myung, Y.J. Lee, Y.-K. Sun, Chem. Mater. 26 (2014) 5973–5979.
[58] D. Wang, R. Kou, Y. Ren, C.J. Sun, H. Zhao, M.J. Zhang, Y. Li, A. Huq, J.P. Ko, F. Pan, Adv. Mater. 29 (2017) 1606715.
[59] W. Xiang, W.-Y. Liu, J. Zhang, S. Wang, T.-T. Zhang, K. Yin, X. Peng, Y.-C. Jiang, K.-H. Liu, X.-D. Guo, J. Alloys. Compd. 775 (2019) 72–80.
[60] J. Zheng, W.H. Kan, A. Manthiram, ACS. Appl. Mater. Interfaces 7 (2015) 6926–6934.
[61] J. Zheng, P. Yan, L. Estevez, C. Wang, J.-G. Zhang, Nano Energy 49 (2018) 538–548.
[62] K. He, Z. Ruan, X. Teng, Y. Zhu, Mater. Res. Bull. 90 (2017) 131–137.
[63] C. Fu, G. Li, D. Luo, Q. Li, J. Fan, L. Li, ACS. Appl. Mater. Interfaces 6 (2014) 15822–15831.
[64] J. Zhang, X. Tan, L. Guo, Y. Jiang, S. Liu, H. Wang, X. Kang, W. Chu, Energy Technol. 7 (2019) 1800752.
[65] Y. Shi, M. Zhang, C. Fang, Y.S. Meng, J. Pow. Sour. 394 (2018) 114–121.
[66] Y. Zhang, K. Du, Y. Cao, Y. Lu, Z. Peng, J. Fan, L. Li, Z. Xue, H. Su, G. Hu, J. Pow. Sour. 477 (2020) 228701.
[67] B. Huang, D. Liu, L. Zhang, K. Qian, K. Zhou, X. Cai, F. Kang, B. Li, ACS. Appl. Energy Mater. 2 (2019) 7403–7411.
[68] M. Zhang, J. Shen, J. Li, D. Zhang, Y. Yan, Y. Huang, Z. Li, Ceram. Int. 46 (2020) 4643–4651.
[69] K.J. Kim, Y.N. Jo, W.J. Lee, T. Subburaj, K. Prasanna, C.W. Lee, J. Pow. Sour. 268 (2014) 349–355.
[70] J. Zhu, J. Zheng, G. Cao, Y. Li, Y. Zhou, S. Deng, C. Hai, J. Pow. Sour. 464 (2020) 228207.
[71] S. Zhang, J. Ma, Z. Hu, G. Cui, L. Chen, Chem. Mater. 31 (2019) 6033–6065.
[72] H.Maleki Kheimeh Sari, X. Li, Adv. Energy Mater. 9 (2019) 1901597.
[73] A. Manthiram, A.V. Murugan, A. Sarkar, T. Muraliganth, Energy Environ. Sci. 1 (2008) 621–638.
[74] W. Liu, P. Oh, X. Liu, M.J. Lee, W. Cho, S. Chae, Y. Kim, J. Cho, Angewandte Chemie Int. Ed. 54 (2015) 4440–4457.
[75] J. Vetter, P. Novák, M.R. Wagner, C. Veit, K.C. Möller, J.O. Besenhard, M. Winter, M. Wohlfahrt-Mehrens, C. Vogler, A. Hammouche, J. Pow. Sour. 147 (2005) 269–281.
[76] B.B. Berkes, A. Schiele, H. Sommer, T. Brezesinski, J. Janek, J. Solid State Electrochem. 20 (2016) 2961–2967.
[77] M. Shikano, H. Kobayashi, S. Koike, H. Sakaebe, E. Ikenaga, K. Kobayashi, K. Tatsumi, J. Pow. Sour. 174 (2007) 795–799.
[78] J. Kim, J. Lee, H. Ma, H.Y. Jeong, H. Cha, H. Lee, Y. Yoo, M. Park, J. Cho, Adv. Mater. 30 (2018) 1704309.
[79] C.S. Yoon, M.H. Choi, B.-B. Lim, E.-J. Lee, Y.-K. Sun, J. Electrochem. Soc. 162 (2015) A2483.
[80] J. Zheng, Y. Ye, T. Liu, Y. Xiao, C. Wang, F. Wang, F. Pan, Acc. Chem. Res. 52 (2019) 2201–2209.
[81] S.K. Jung, H. Gwon, J. Hong, K.Y. Park, D.H. Seo, H. Kim, J. Hyun, W. Yang, K. Kang, Adv. Energy Mater. 4 (2014) 1300787.
[82] R.D. Shannon, Revised effective ionic radii and systematic studies of interatomic distances in halides and chalcogenides, Acta crystallographica section A: crystal physics, diffraction, theoretical and general crystallography 32 (5) (1976) 751–767.
[83] U.-H. Kim, G.-T. Park, B.-K. Son, G.W. Nam, J. Liu, L.-Y. Kuo, P. Kaghazchi, C. S. Yoon, Y.-K. Sun, Nat. Energy 5 (2020) 860–869.
[84] Y. Wang, Q. Yang, Y. Zhao, S. Du, C. Zhi, Adv. Mater. Technol. 4 (2019) 1900083.
[85] D. Goonetilleke, N. Sharma, W.K. Pang, V.K. Peterson, R. Petibon, J. Li, J. Dahn, Chem. Mater. 31 (2018) 376–386.
[86] F. Kong, C. Liang, L. Wang, Y. Zheng, S. Perananthan, R.C. Longo, J.P. Ferraris, M. Kim, K. Cho, Adv. Energy Mater. 9 (2019) 1802586.
[87] S.-H. Lee, S. Lee, B.-S. Jin, H.-S. Kim, Int. J. Hydrogen. Energy 44 (2019) 13684–13689.
[88] Y. You, H. Celio, J. Li, A. Dolocan, A. Manthiram, Angewandte Chemie Int. Ed. 57 (2018) 6480–6485.
[89] J.H. Jo, C.-H. Jo, H. Yashiro, S.-J. Kim, S.-T. Myung, J. Pow. Sour. 313 (2016) 1–8.
[90] X. Zeng, T. Jian, Y. Lu, L. Yang, W. Ma, Y. Yang, J. Zhu, C. Huang, S. Dai, X. Xi, ACS. Sustain. Chem. Eng. 8 (2020) 6293–6304.
[91] J. Kim, H. Lee, H. Cha, M. Yoon, M. Park, J. Cho, Adv. Energy Mater. 8 (2018) 1702028.
[92] S.W. Doo, S. Lee, H. Kim, J.H. Choi, K.T. Lee, ACS. Appl. Energy Mater. 2 (2019) 6246–6253.
[93] S. Kang, H.-s. Kim, J.Y. Jung, K.-H. Park, K. Kim, J.H. Song, J.-S. Yu, Y.-J. Kim, W. Cho, ACS. Appl. Mater. Interfaces 15 (2023) 10744–10751.
[94] A. Grenier, H. Liu, K.M. Wiaderek, Z.W. Lebens-Higgins, O.J. Borkiewicz, L.F. J. Piper, P.J. Chupas, K.W. Chapman, Chem. Mater. 29 (2017) 7345–7352.
[95] K. Qian, B. Huang, Y. Liu, M. Wagemaker, M. Liu, H. Duan, D. Liu, Y.-B. He, B. Li, F. Kang, J. Mater. Chem. A 7 (2019) 12723–12731.
[96] Y. Bi, T. Wang, M. Liu, R. Du, W. Yang, Z. Liu, Z. Peng, Y. Liu, D. Wang, X. Sun, RSC. Adv. 6 (2016) 19233–19237.
[97] S.E. Renfrew, B.D. McCloskey, J. Am. Chem. Soc. 139 (2017) 17853–17860.
[98] T. Hatsukade, A. Schiele, P. Hartmann, T. Brezesinski, J.r. Janek, ACS. Appl. Mater. Interfaces 10 (2018) 38892–38899.
[99] Q. Gan, N. Qin, Y. Zhu, Z. Huang, F. Zhang, S. Gu, J. Xie, K. Zhang, L. Lu, Z. Lu, ACS. Appl. Mater. Interfaces 11 (2019) 12594–12604.
[100] X. Tian, Y. Yi, B. Fang, P. Yang, T. Wang, P. Liu, L. Qu, M. Li, S. Zhang, Chem. Mater. 32 (2020) 9821–9848.
[101] S.E. Renfrew, B.D. McCloskey, ACS. Appl. Energy Mater. 2 (2019) 3762–3772.
[102] S.E. Renfrew, L.A. Kaufman, B.D. McCloskey, ACS. Appl. Mater. Interfaces 11 (2019) 34913–34921.
[103] D. S treich, C. Erk, A. Guéguen, P. Müller, F.-F. Chesneau, E.J. Berg, J. Phys. Chem. C 121 (2017) 13481–13486.
[104] D. Streich, C. Erk, A. Guéguen, P. Müller, F.-F. Chesneau, E.J. Berg, J. Phys. Chem. C 121 (2017) 13481–13486.
[105] J. Duan, X. Tang, H. Dai, Y. Yang, W. Wu, X. Wei, Y. Huang, Electrochem. Energ. Rev. 3 (2020) 1–42.
[106] X. Liu, G.-L. Xu, L. Yin, I. Hwang, Y. Li, L. Lu, W. Xu, X. Zhang, Y. Chen, Y. Ren, C.-J. Sun, Z. Chen, M. Ouyang, K. Amine, J. Am. Chem. Soc. 142 (2020) 19745–19753.
[107] X. Liu, G.-L. Xu, L. Yin, I. Hwang, Y. Li, L. Lu, W. Xu, X. Zhang, Y. Chen, Y. Ren, J. Am. Chem. Soc. 142 (2020) 19745–19753.
[108] E. Flores, N. Vonrüti, P. Novák, U. Aschauer, E.J. Berg, Chem. Mater. 30 (2018) 4694–4703.
[109] J. Li, L.E. Downie, L. Ma, W. Qiu, J.R. Dahn, J. Electrochem. Soc. 162 (2015) A1401.
[110] G. Cherkashinin, K. Nikolowski, H. Ehrenberg, S. Jacke, L. Dimesso, W. Jaegermann, Phys. Chem. Chem. Phys. 14 (2012) 12321–12331.
[111] M.K. Rahman, Y. Saito, J. Pow. Sour. 174 (2007) 889–894.
[112] F. Lin, I.M. Markus, D. Nordlund, T.-C. Weng, M.D. Asta, H.L. Xin, M.M. Doeff, Nat. Commun. 5 (2014) 3529.
[113] G. Cherkashinin, M. Motzko, N. Schulz, T. Späth, W. Jaegermann, Chem. Mater. 27 (2015) 2875–2887.
[114] W. Yang, Z. Liu. Synchrotron Radiation in Materials Science: Light Sources, Techniques, and Applications, Wiley-VCH , 2, 2018, pp. 511–562.
[115] J.-S. Kim, K. Kim, W. Cho, W.H. Shin, R. Kanno, J.W. Choi, Nano Lett. 12 (2012) 6358–6365.
[116] W. Li, U.-H. Kim, A. Dolocan, Y.-K. Sun, A. Manthiram, ACS. Nano 11 (2017) 5853–5863.
[117] S.-T. Myung, K. Amine, Y.-K. Sun, J. Mater. Chem. 20 (2010) 7074–7095.
[118] W.M. Dose, W. Li, I. Temprano, C.A. O'Keefe, B.L. Mehdi, M.F.L. De Volder, C. P. Grey, ACS. Energy Lett. 7 (2022) 3524–3530.
[119] W. Xue, M. Huang, Y. Li, Y.G. Zhu, R. Gao, X. Xiao, W. Zhang, S. Li, G. Xu, Y. Yu, P. Li, J. Lopez, D. Yu, Y. Dong, W. Fan, Z. Shi, R. Xiong, C.-J. Sun, I. Hwang, W.-K. Lee, Y. Shao-Horn, J.A. Johnson, J. Li, Nat. Energy 6 (2021) 495–505.
[120] A. Manthiram, J.C. Knight, S.T. Myung, S.M. Oh, Y.K. Sun, Adv. Energy Mater. 6 (2016) 1501010.
[121] J.A. Gilbert, I.A. Shkrob, D.P. Abraham, J. Electrochem. Soc. 164 (2017) A389.
[122] T. Joshi, K. Eom, G. Yushin, T.F. Fuller, J. Electrochem. Soc. 161 (2014) A1915.
[123] R. Bhattacharyya, B. Key, H. Chen, A.S. Best, A.F. Hollenkamp, C.P. Grey, Nat. Mater. 9 (2010) 504–510.
[124] Q. Liu, C. Du, B. Shen, P. Zuo, X. Cheng, Y. Ma, G. Yin, Y. Gao, RSC. Adv. 6 (2016) 88683–88700.

[125] D. Aurbach, E. Zinigrad, Y. Cohen, H. Teller, Solid. State Ion. 148 (2002) 405–416.
[126] H. Zheng, Q. Sun, G. Liu, X. Song, V.S. Battaglia, J. Pow. Sour. 207 (2012) 134–140.
[127] D.R. Gallus, R. Schmitz, R. Wagner, B. Hoffmann, S. Nowak, I. Cekic-Laskovic, R. W. Schmitz, M. Winter, Electrochim. Acta 134 (2014) 393–398.
[128] O.B. Chae, B.L. Lucht, Adv. Energy Mater. 13 (2023) 2203791.
[129] Q. Liu, X. Su, D. Lei, Y. Qin, J. Wen, F. Guo, Y.A. Wu, Y. Rong, R. Kou, X. Xiao, F. Aguesse, J. Bareño, Y. Ren, W. Lu, Y. Li, Nat. Energy 3 (2018) 936–943.
[130] Y.-M. Song, J.-G. Han, S. Park, K.T. Lee, N.-S. Choi, J. Mater. Chem. A 2 (2014) 9506–9513.
[131] H.-H. Sun, A. Manthiram, Chem. Mater. 29 (2017) 8486–8493.
[132] S. Watanabe, M. Kinoshita, T. Hosokawa, K. Morigaki, K. Nakura, J. Pow. Sour. 260 (2014) 50–56.
[133] D.-W. Jun, C.S. Yoon, U.-H. Kim, Y.-K. Sun, Chem. Mater. 29 (2017) 5048–5052.
[134] U.-H. Kim, S.-T. Myung, C.S. Yoon, Y.-K. Sun, ACS. Energy Lett. 2 (2017) 1848–1854.
[135] C.S. Yoon, D.-W. Jun, S.-T. Myung, Y.-K. Sun, ACS. Energy Lett. 2 (2017) 1150–1155.
[136] J.-M. Lim, T. Hwang, D. Kim, M.-S. Park, K. Cho, M. Cho, Sci. Rep. 7 (2017) 39669.
[137] M. Dixit, B. Markovsky, F. Schipper, D. Aurbach, D.T. Major, J. Phys. Chem. C 121 (2017) 22628–22636.
[138] W. Li, H.Y. Asl, Q. Xie, A. Manthiram, J. Am. Chem. Soc. 141 (2019) 5097–5101.
[139] H.-J. Noh, S. Youn, C.S. Yoon, Y.-K. Sun, J. Pow. Sour. 233 (2013) 121–130.
[140] C. Xu, P.J. Reeves, Q. Jacquet, C.P. Grey, Adv. Energy Mater. 11 (2021) 2003404.
[141] S.S. Zhang, J. Energy Chem. 41 (2020) 135–141.
[142] Z. Ruff, C.S. Coates, K. Märker, A. Mahadevegowda, C. Xu, M.E. Penrod, C. Ducati, C.P. Grey, Chem. Mater. 35 (2023) 4979–4987.
[143] H. Li, A. Liu, N. Zhang, Y. Wang, S. Yin, H. Wu, J.R. Dahn, Chem. Mater. 31 (2019) 7574–7583.
[144] M. Jeong, H. Kim, W. Lee, S.-J. Ahn, E. Lee, W.-S. Yoon, J. Pow. Sour. 474 (2020) 228592.
[145] Q. Tao, L. Wang, C. Shi, J. Li, G. Chen, Z. Xue, J. Wang, S. Wang, H. Jin, Mater. Chem. Front. 5 (2021) 2607–2622.
[146] S. Schweidler, L. de Biasi, G. Garcia, A. Mazilkin, P. Hartmann, T. Brezesinski, J. Janek, ACS. Appl. Energy Mater. 2 (2019) 7375–7384.
[147] S.-M. Bak, E. Hu, Y. Zhou, X. Yu, S.D. Senanayake, S.-J. Cho, K.-B. Kim, K. Y. Chung, X.-Q. Yang, K.-W. Nam, ACS. Appl. Mater. Interfaces 6 (2014) 22594–22601.
[148] T. Weigel, F. Schipper, E.M. Erickson, F.A. Susai, B. Markovsky, D. Aurbach, ACS. Energy Lett. 4 (2019) 508–516.
[149] R. Du, Y. Bi, W. Yang, Z. Peng, M. Liu, Y. Liu, B. Wu, B. Yang, F. Ding, D. Wang, Ceram. Int. 41 (2015) 7133–7139.
[150] A. Saleem, H. Zhu, M.K. Majeed, R. Iqbal, B. Jabar, A. Hussain, M.Z. Ashfaq, M. Ahmad, S. Rauf, J.P. Mwizerwa, J. Shen, Q. Liu, ACS. Appl. Mater. Interfaces 15 (2023) 20843–20853.
[151] N.-Y. Park, G. Cho, S.-B. Kim, Y.-K. Sun, Adv. Energy Mater. 13 (2023) 2204291.
[152] F. Kong, C. Liang, R.C. Longo, D.-H. Yeon, Y. Zheng, J.-H. Park, S.-G. Doo, K. Cho, Chem. Mater. 28 (2016) 6942–6952.
[153] U.-H. Kim, G.-T. Park, P. Conlin, N. Ashburn, K. Cho, Y.-S. Yu, D.A. Shapiro, F. Maglia, S.-J. Kim, P. Lamp, C.S. Yoon, Y.-K. Sun, Energy Environ. Sci. 14 (2021) 1573–1583.
[154] U.H. Kim, D.W. Jun, K.J. Park, Q. Zhang, P. Kaghazchi, D. Aurbach, D.T. Major, G. Goobes, M. Dixit, N. Leifer, C.M. Wang, P. Yan, D. Ahn, K.H. Kim, C.S. Yoon, Y. K. Sun, Energy Environ. Sci. 11 (2018) 1271–1279.
[155] G.-T. Park, H.-H. Ryu, N.-Y. Park, C.S. Yoon, Y.-K. Sun, J. Pow. Sour. 442 (2019) 227242.
[156] C. Xu, W. Xiang, Z. Wu, Y. Xu, Y. Li, Y. Wang, Y. Xiao, X. Guo, B. Zhong, ACS. Appl. Mater. Interfaces 11 (2019) 16629–16638.
[157] H.-H. Ryu, N.-Y. Park, T.-C. Noh, G.-C. Kang, F. Maglia, S.-J. Kim, C.S. Yoon, Y.-K. Sun, ACS. Energy Lett. 6 (2021) 216–223.
[158] K.-J. Park, H.-G. Jung, L.-Y. Kuo, P. Kaghazchi, C.S. Yoon, Y.-K. Sun, Adv. Energy Mater. 8 (2018) 1801202.
[159] H.-H. Ryu, N.-Y. Park, J.H. Seo, Y.-S. Yu, M. Sharma, R. Mücke, P. Kaghazchi, C. S. Yoon, Y.-K. Sun, Mater. Today 36 (2020) 73–82.
[160] S.-H. Han, J.H. Song, T. Yim, Y.-J. Kim, J.-S. Yu, S. Yoon, J. Electrochem. Soc. 163 (2016) A748.
[161] H.-H. Ryu, K.-J. Park, D.R. Yoon, A. Aishova, C.S. Yoon, Y.-K. Sun, Adv. Energy Mater. 9 (2019) 1902698.
[162] Z. Cui, Q. Xie, A. Manthiram, Adv. Energy Mater. 11 (2021) 2102421.
[163] W. Li, S. Lee, A. Manthiram, Adv. Mater. 32 (2020) 2002718.
[164] Z. Zhang, B. Hong, M. Yi, X. Fan, Z. Zhang, X. Huang, Y. Lai, Chem. Eng. J. 445 (2022) 136825.
[165] U.-H. Kim, L.-Y. Kuo, P. Kaghazchi, C.S. Yoon, Y.-K. Sun, ACS. Energy Lett. 4 (2019) 576–582.
[166] S. Ansah, H. Hyun, N. Shin, J.-S. Lee, J. Lim, H.-H. Cho, Data Brief. 37 (2021) 107246.
[167] S.H. Song, M. Cho, I. Park, J.G. Yoo, K.T. Ko, J. Hong, J. Kim, S.K. Jung, M. Avdeev, S. Ji, Adv. Energy Mater. 10 (2020) 2000521.
[168] H. Kim, S. Lee, H. Cho, J. Kim, J. Lee, S. Park, S.H. Joo, S.H. Kim, Y.-G. Cho, H.-K. Song, S.K. Kwak, J. Cho, Adv. Mater. 28 (2016) 4705–4712.
[169] J. Kim, H. Ma, H. Cha, H. Lee, J. Sung, M. Seo, P. Oh, M. Park, J. Cho, Energy Environ. Sci. 11 (2018) 1449–1459.
[170] A. Saleem, M.K. Majeed, R. Iqbal, A. Hussain, M.S. Naeem, S. Rauf, Y. Wang, M. S. Javed, J. Shen, Adv. Mater. Interfaces 9 (2022) 2200800.
[171] M.-J. Lee, M. Noh, M.-H. Park, M. Jo, H. Kim, H. Nam, J. Cho, J. Mater. Chem. A 3 (2015) 13453–13460.
[172] C.-H. Jo, D.-H. Cho, H.-J. Noh, H. Yashiro, Y.-K. Sun, S.T. Myung, Nano Res. 8 (2015) 1464–1479.
[173] A.Y. Kim, F. Strauss, T. Bartsch, J.H. Teo, T. Hatsukade, A. Mazilkin, J. Janek, P. Hartmann, T. Brezesinski, Chem. Mater. 31 (2019) 9664–9672.
[174] S. Jeong, J.H. Park, S.Y. Park, J. Kim, K.T. Lee, Y.D. Park, J. Mun, ACS. Appl. Mater. Interfaces 13 (2021) 22475–22484.
[175] H.J. Song, S.H. Oh, Y. Lee, J. Kim, T. Yim, J. Pow. Sour. 483 (2021) 229218.
[176] Q. Fan, K. Lin, S. Yang, S. Guan, J. Chen, S. Feng, J. Liu, L. Liu, J. Li, Z. Shi, J. Pow. Sour. 477 (2020) 228745.
[177] A.M. Wise, C. Ban, J.N. Weker, S. Misra, A.S. Cavanagh, Z. Wu, Z. Li, M. S. Whittingham, K. Xu, S.M. George, Chem. Mater. 27 (2015) 6146–6154.
[178] Y. Li, X. Liu, D. Ren, H. Hsu, G.-L. Xu, J. Hou, L. Wang, X. Feng, L. Lu, W. Xu, Nano Energy 71 (2020) 104643.
[179] D. Hu, Y. Su, L. Chen, N. Li, L. Bao, Y. Lu, Q. Zhang, J. Wang, S. Chen, F. Wu, J. Energy Chem. 58 (2021) 1–8.
[180] K. Liu, Q. Zhang, S. Dai, W. Li, X. Liu, F. Ding, J. Zhang, ACS. Appl. Mater. Interfaces 10 (2018) 34153–34162.
[181] H.-H. Sun, J.-Y. Hwang, C.S. Yoon, A. Heller, C.B. Mullins, ACS. Nano 12 (2018) 12912–12922.
[182] Y.-G. Zou, F. Meng, D. Xiao, H. Sheng, W.-P. Chen, X.-H. Meng, Y.-H. Du, L. Gu, J.-L. Shi, Y.-G. Guo, Nano Energy 87 (2021) 106172.
[183] N.-H. Yeh, F.-M. Wang, C. Khotimah, X.-C. Wang, Y.-W. Lin, S.-C. Chang, C.-C. Hsu, Y.-J. Chang, L. Tiong, C.-H. Liu, ACS. Appl. Mater. Interfaces 13 (2021) 7355–7369.
[184] S. Yang, Q. Fan, Z. Shi, L. Liu, J. Liu, X. Ke, J. Liu, C. Hong, Y. Yang, Z. Guo, ACS. Appl. Mater. Interfaces 11 (2019) 36742–36750.
[185] K. Du, A. Gao, L. Gao, S. Sun, X. Lu, C. Yu, S. Li, H. Zhao, Y. Bai, Nano Energy 83 (2021) 105775.
[186] J.-M. Kim, X. Zhang, J.-G. Zhang, A. Manthiram, Y.S. Meng, W. Xu, Mater. Today 46 (2021) 155–182.
[187] K. Sahni, M. Ashuri, Q. He, R. Sahore, I.D. Bloom, Y. Liu, J.A. Kaduk, L.L. Shaw, Electrochim. Acta 301 (2019) 8–22.
[188] C. Chen, W. Yao, Q. He, M. Ashuri, J. Kaduk, Y. Liu, L. Shaw, ACS. Appl. Energy Mater. 2 (2019) 3098–3113.
[189] H. Kim, M.G. Kim, H.Y. Jeong, H. Nam, J. Cho, Nano Lett. 15 (2015) 2111–2119.
[190] P. Yan, J. Zheng, J. Liu, B. Wang, X. Cheng, Y. Zhang, X. Sun, C. Wang, J.-G. Zhang, Nat. Energy 3 (2018) 600–605.
[191] X. Cheng, J. Zheng, J. Lu, Y. Li, P. Yan, Y. Zhang, Nano Energy 62 (2019) 30–37.
[192] H.-H. Ryu, H.-W. Lim, G.-C. Kang, N.-Y. Park, Y.-K. Sun, ACS. Energy Lett. 8 (2023) 1354–1361.
[193] W. Mo, Z. Wang, J. Wang, X. Li, H. Guo, W. Peng, G. Yan, Chem. Eng. J. 400 (2020) 125820.
[194] K. Min, C. Jung, D.-S. Ko, K. Kim, J. Jang, K. Park, E. Cho, ACS. Appl. Mater. Interfaces 10 (2018) 20599–20610.
[195] Y.-K. Sun, S.-T. Myung, M.-H. Kim, J. Prakash, K. Amine, J. Am. Chem. Soc. 127 (2005) 13411–13418.
[196] E.-J. Lee, Z. Chen, H.-J. Noh, S.C. Nam, S. Kang, D.H. Kim, K. Amine, Y.-K. Sun, Nano Lett. 14 (2014) 4873–4880.
[197] Y.-K. Sun, Z. Chen, H.-J. Noh, D.-J. Lee, H.-G. Jung, Y. Ren, S. Wang, C.S. Yoon, S.-T. Myung, K. Amine, Nat. Mater. 11 (2012) 942–947.
[198] H.-H. Sun, J.A. Weeks, A. Heller, C.B. Mullins, ACS. Appl. Energy Mater. 2 (2019) 6002–6011.
[199] K.-J. Park, M.-J. Choi, F. Maglia, S.-J. Kim, K.-H. Kim, C.S. Yoon, Y.-K. Sun, Adv. Energy Mater. 8 (2018) 1703612.
[200] Y.-K. Sun, S.-T. Myung, B.-C. Park, J. Prakash, I. Belharouak, K. Amine, Nat. Mater. 8 (2009) 320–324.
[201] K.-J. Park, B.-B. Lim, M.-H. Choi, H.-G. Jung, Y.-K. Sun, M. Haro, N. Vicente, J. Bisquert, G. Garcia-Belmonte, J. Mater. Chem. A 3 (2015) 22183–22190.
[202] S. Lou, Q. Liu, F. Zhang, Q. Liu, Z. Yu, T. Mu, Y. Zhao, J. Borovilas, Y. Chen, M. Ge, X. Xiao, W.-K. Lee, G. Yin, Y. Yang, X. Sun, J. Wang, Nat. Commun. 11 (2020) 5700.
[203] U.-H. Kim, H.-H. Ryu, J.-H. Kim, R. Mücke, P. Kaghazchi, C.S. Yoon, Y.-K. Sun, Adv. Energy Mater. 9 (2019) 1803902.
[204] J. Li, A.R. Cameron, H. Li, S. Glazier, D. Xiong, M. Chatzidakis, J. Allen, G. A. Botton, J.R. Dahn, J. Electrochem. Soc. 164 (2017) A1534.
[205] X. Xu, H. Huo, J. Jian, L. Wang, H. Zhu, S. Xu, X. He, G. Yin, C. Du, X. Sun, Adv. Energy Mater. 9 (2019) 1803963.
[206] X. Fan, G. Hu, B. Zhang, X. Ou, J. Zhang, W. Zhao, H. Jia, L. Zou, P. Li, Y. Yang, Nano Energy 70 (2020) 104450.
[207] A. Saleem, A. Hussain, M.Z. Ashfaq, M.S. Javed, S. Rauf, M.M. Hussain, A. Saad, J. Shen, M.K. Majeed, R. Iqbal, J. Alloys. Compd. 924 (2022) 166375.
[208] R. Zhang, C. Wang, M. Ge, H.L. Xin, Nano Lett. 22 (2022) 3818–3824.
[209] W. Jiang, X. Fan, X. Zhu, Z. Wu, Z. Li, R. Huang, S. Zhao, X. Zeng, G. Hu, B. Zhang, S. Zhang, L. Zhu, L. Yan, M. Ling, L. Wang, C. Liang, J. Pow. Sour. 508 (2021) 230335.
[210] Y. Bi, J. Tao, Y. Wu, L. Li, Y. Xu, E. Hu, B. Wu, J. Hu, C. Wang, J.-G. Zhang, Y. Qi, J. Xiao, Science (1979) 370 (2020) 1313–1317.
[211] W. Zhao, K. Wang, X. Fan, F. Ren, X. Xu, Y. Liu, S. Xiong, X. Liu, Z. Zhang, M. Si, R. Zhang, W. van den Bergh, P. Yan, C. Battaglia, T. Brezesinski, Y. Yang, Angewandte Chemie Int. Ed. 62 (2023) e202305281.
[212] X. Ou, T. Liu, W. Zhong, X. Fan, X. Guo, X. Huang, L. Cao, J. Hu, B. Zhang, Y. S. Chu, G. Hu, Z. Lin, M. Dahbi, J. Alami, K. Amine, C. Yang, J. Lu, Nat. Commun. 13 (2022) 2319.

[213] J. Li, H. Yang, Q. Deng, W. Li, Q. Zhang, Z. Zhang, Y. Chu, C. Yang, Angewandte Chemie Int. Ed. 63 (2024) e202318042.
[214] X. Fan, X. Ou, W. Zhao, Y. Liu, B. Zhang, J. Zhang, L. Zou, L. Seidl, Y. Li, G. Hu, C. Battaglia, Y. Yang, Nat. Commun. 12 (2021) 5320.
[215] Y. Liu, Q. Wang, L. Chen, Z. Xiao, X. Fan, S. Ma, L. Ming, A. Tayal, B. Zhang, F. Wu, X. Ou, Materials Today 61 (2022) 40–53.
[216] H. Yang, H.-H. Wu, M. Ge, L. Li, Y. Yuan, Q. Yao, J. Chen, L. Xia, J. Zheng, Z. Chen, J. Duan, K. Kisslinger, X.C. Zeng, W.-K. Lee, Q. Zhang, J. Lu, Adv. Funct. Mater. 29 (2019) 1808825.
[217] M. Yoon, Y. Dong, J. Hwang, J. Sung, H. Cha, K. Ahn, Y. Huang, S.J. Kang, J. Li, J. Cho, Nat. Energy 6 (2021) 362–371.
[218] L.-b. Tang, Y. Liu, H.-x. Wei, C. Yan, Z.-j. He, Y.-j. Li, J.-c. Zheng, J. Energy Chem. 55 (2021) 114–123.
[219] B.-B. Lim, S.-T. Myung, C.S. Yoon, Y.-K. Sun, ACS. Energy Lett. 1 (2016) 283–289.
[220] U.-H. Kim, J.-H. Kim, J.-Y. Hwang, H.-H. Ryu, C.S. Yoon, Y.-K. Sun, Mater. Today 23 (2019) 26–36.
[221] U.-H. Kim, E.-J. Lee, C.S. Yoon, S.-T. Myung, Y.-K. Sun, Adv. Energy Mater. 6 (2016) 1601417.
[222] N.-Y. Park, H.-H. Ryu, G.-T. Park, T.-C. Noh, Y.-K. Sun, Adv. Energy Mater. 11 (2021) 2003767.
[223] K. Kim, H. Ma, S. Park, N.-S. Choi, ACS. Energy Lett. 5 (2020) 1537–1553.
[224] J.-M. Kim, Y. Xu, M.H. Engelhard, J. Hu, H.-S. Lim, H. Jia, Z. Yang, B. E. Matthews, S. Tripathi, X. Zhang, L. Zhong, F. Lin, C. Wang, W. Xu, ACS. Appl. Mater. Interfaces 14 (2022) 17405–17414.
[225] J. Dong, F. Wu, J. Zhao, Q. Shi, Y. Lu, N. Li, D. Cao, W. Li, J. Hao, X. Yang, L. Chen, Y. Su, Energy Storage Mater. 60 (2023) 102798.
[226] F. Wu, J. Dong, L. Chen, L. Bao, N. Li, D. Cao, Y. Lu, R. Xue, N. Liu, L. Wei, Z. Wang, S. Chen, Y. Su, Energy Storage Mater. 41 (2021) 495–504.
[227] J. Zhao, Y. Liang, X. Zhang, Z. Zhang, E. Wang, S. He, B. Wang, Z. Han, J. Lu, K. Amine, H. Yu, Adv. Funct. Mater. 31 (2021) 2009192.